

University of Alberta

Charge Transport in Molecular Junctions and Microfluidic Devices

by

Steven Wayne Olson

A thesis submitted to the Faculty of Graduate Studies and Research
in partial fulfillment of the requirements for the degree of

Master of Science

Department of Physics

©Steven Wayne Olson
Fall 2010
Edmonton, Alberta

Permission is hereby granted to the University of Alberta Libraries to reproduce single copies of this thesis and to lend or sell such copies for private, scholarly or scientific research purposes only. Where the thesis is converted to, or otherwise made available in digital form, the University of Alberta will advise potential users of the thesis of these terms.

The author reserves all other publication and other rights in association with the copyright in the thesis and, except as herein before provided, neither the thesis nor any substantial portion thereof may be printed or otherwise reproduced in any material form whatsoever without the author's prior written permission.

Examining Committee

Mark Freeman, Physics

Frank Marsiglio, Physics

Richard McCreery, Chemistry

Richard Sydora, Physics

Abstract

Electro-transmittance of molecular junctions was characterized electrically and studied optically at 410nm and 532nm. Between 1kHz and 100kHz there was no qualitative difference between the control samples and the molecular junction samples, however there were difficulties with reproducibility of the quantitative behaviour, so no hard conclusions could be drawn. A microfluidic capacitor device was designed and fabricated to study the electrical double layer, using standard microfabrication techniques. A complimentary flux corrected transport simulation was written using the same experimental geometry and the results of this study found qualitative agreement between the simulation and experiment. The experiment produced results about the concentration dependence of the double layer formation time which allows an estimate of the required frequency of an AC electrical signal for which the electrical double layer doesn't have time to form, and its effects can be ignored.

Acknowledgments

I have received much help and support during this work, and I would like to acknowledge them here.

First I would like to thank my lab mates, who have both been great help with ideas, and also have been great friends during my time here, Robert Bryce, Jacob Burgess, Shawn Compton, John Davis, Alastair Fraser, Mohammad Hedayatipour and Joe Losby. Don Mullin and Greg Popowich have been great help in the thin films lab, and with any electronics help I have needed. Tony Walford has been very helpful in the machine shop. I would like to thank Lynn Chandler who has been very helpful and friendly while I have been here. I would like to thank the staff at the Nanofab, where most of the fabrication for this project has been done, specifically Stephanie, Keith, Scott, Les and Glen. I would also like to thank Dr. McCreery and Adam Bergren for the molecular junction samples. I also need to thank summer students George Coomber and Sonia Milbradt as well as Dave Fortin who wrote all of the labview programs used in this thesis. I would like to thank my fellow graduate students (past and present) in the department who have been good friends, and specifically Josh Mutus, Tyler Cocker, Tyler Luchko, James Day, Vince Sauer, and any others who I might have missed who have helped me unwind from research by playing sports. I also need to thank Devin Baillie who has been an amazing resource for anything computer related. And Dr. Rick Sydora who provided lots of guidance and suggestions for the simulation in this thesis.

Special thanks to my supervisor, Mark Freeman. I couldn't have had a better supervisor and I have learned from just about every discussion I have had with him. I would not have been able to complete this work without his guidance and am glad I got the opportunity to work with him both as an undergraduate intern, and as a graduate student. I wouldn't be where I am

today without Mark.

Lastly I would like to thank my parents for being very supportive of me when things weren't working, and excited for me when they were.

Contents

1	Introduction	1
1.1	Introduction	1
1.2	Electrical Double Layer	1
1.3	Molecular Junction	6
1.4	Charge Transport	8
2	Device	9
2.1	Microfluidic Capacitor Design	9
2.1.1	Introduction	9
2.1.2	Design	10
2.2	Device Fabrication	13
2.3	Molecular Junction Fabrication	23
3	Molecular Junction Experiments	25
3.1	Introduction	25
3.2	Samples	26
3.3	Optical Set Up	27
3.4	Laser Stability	27
3.5	Current Voltage Characteristics	29
3.5.1	Experimental Set Up	29
3.5.2	I-V Results	32

3.6	Raster Scan	33
3.7	Modulation	39
3.8	Experimental Conclusions	44
4	Electrical Double Layer Simulation	46
4.1	Introduction	46
4.2	Flux-Corrected Transport Method	47
4.2.1	Introduction	47
4.2.2	The Model	48
4.2.3	Lower Order Method	49
4.2.4	High Order Method	53
4.2.5	Electric Field and Potential	57
4.2.6	Flux Corrected Transport Algorithm	62
4.2.7	Realistic Voltage Pulse	66
4.2.8	Current	68
4.2.9	Parylene Model	70
4.3	Simulation Parameters	74
4.4	Results	74
4.5	Future Work	77
5	Electrical Double Layer Experiment	80
5.1	Introduction	80
5.2	Dielectric Model of Microfluidic Capacitor	84
5.3	Analysis	103
5.3.1	Initial Data Analysis	103
5.3.2	Data Driven Model	109
5.4	Results	110
5.5	Comparison with Simulation	120

5.6	Experimental conclusions	122
6	Conclusion	124
	Bibliography	127
A	FCT C++ Code	131

List of Tables

5.1	Model and Experiment τ for varying C_2	83
5.2	Varying C_1	84
5.3	Power law fit parameters	118

List of Figures

1.1	Cell Geometry	3
1.2	Gouy Chapman Solutions for Finite System	4
1.3	Molecular Junction Schematic	7
1.4	Molecular Junction Spectrum's	8
2.1	Microfluidic Capacitor Schematic	10
2.2	Optical Lithography Mask Designs	13
2.3	Parylene Deposition	17
2.4	Sample Holder	21
3.1	Optical Setup Schematic	28
3.2	Optical Power Stability	30
3.3	I-V experiment schematic	31
3.4	I-V and $\frac{dI}{dV}$ vs V curves	33
3.5	Rasterscan of DC transmittance	35
3.6	Rasterscan of AC amplitude	36
3.7	Rasterscan of AC phase	37
3.8	Rasterscan of damaged sample in AC amplitude	38
3.9	AC amplitude for multiple runs of NAB-1 sample	40
3.10	AC amplitude and phase of NAB-1 and control samples	41
3.11	Amplitude of NAB-1 and NAB-4 for 410nm beam	42

3.12	AC amplitude at different locations on the sample	43
3.13	AC amplitude and phase varying bias and frequency	44
4.1	Low Order Ion density distribution	51
4.2	Low Order ion flux	52
4.3	High order ion density	54
4.4	High order ion flux	56
4.5	Electric field and potential evolution	58
4.6	Comparing electric field and potential to the Gouy-Chapman solutions	60
4.7	Comparing FCT, low and high order solutions	65
4.8	Input pulse interpolation	67
4.9	Spatial Distribution of current in microchannel	70
4.10	Current through first grid point	71
4.11	Experimental and Simulated currents	72
4.12	Parylene Dielectric Model	72
4.13	Parylene Model	73
4.14	Simulated current for different ion concentrations	76
4.15	Time constant as a function of concentration	76
4.16	Time constant as a function of input potential magnitude	77
5.1	Experimental circuit schematics	82
5.2	Schematics of dielectric models	85
5.3	Initial 3 layer dielectric model	86
5.4	Intermediate 5 layer dielectric model	89
5.5	Electric field and Potential in equilibrium	89
5.6	Time Dependent Capacitance	93
5.7	Displacement Current with time dependent capacitance	94

5.8	Total current using realistic parameters	95
5.9	Comparing the model and experiment	97
5.10	Case 2 Double Layer Discharging	99
5.11	Improved Double Layer Discharge Fit	102
5.12	Device capacitance in air and theoretical capacitance	104
5.13	Microfluidic capacitor device equivalent circuit	104
5.14	Sample input pulse and voltage response	106
5.15	Potential drop as a function of parylene thickness	106
5.16	Capacitance of sample from varying load resistance	107
5.17	Offset subtraction procedure	111
5.18	Subtracted offsets	112
5.19	Non linear behavior for small load resistances	113
5.20	Subtracted linear behavior to isolate non linear behavior	114
5.21	Second time constant	114
5.22	Empirical model fits	115
5.23	Theoretical capacitance of device in equilibrium as a function of concentration	116
5.24	Experimental capacitance of device in equilibrium as a function of concentration for large load resistances	116
5.25	Experimental capacitance of device in equilibrium as a function of concentration for small load resistance	117
5.26	Experimental power law fits	118
5.27	Time constant calculated with power law fits as a function of frequency	119
5.28	Circuit Model Fit	120

Nomenclature

Δt	Time step for simulation
Δx	Distance between 2 gridpoints in simulation
ϵ	dielectric constant
λ	wavelength
λ_D	Debye length
μm	micrometer
μ	ion mobility
Ω	Ohm
ϕ_{j+1}^A	Antidiffusive flux
ϕ_{j+1}^C	Corrected flux
ϕ_{j+1}^H	Higher order flux
ϕ_{j+1}^L	Lower order flux
C_{j+1}	Flux correction multiplier
$c_{j+\frac{1}{2}}$	Courant number
$k\Omega$	kiloohm

k_B Boltzmann constant

$M\Omega$ megaohm

p_0 concentration

$s_{j+\frac{1}{2}}$ diffusion constant for simulation

SiO_2 Silicon dioxide

V_{dr} Driving voltage

V_{RC} Voltage drop across RC circuit elements

A Area

AC Alternating Current

AQ Anthraquinone

Au Gold

C Capacitance

Cr Chromium

D diffusion constant

d distance

DAQ Data acquisition

DC Direct current

E electric field

e magnitude of the electron charge

EOM Electro-optic modulator

FCT Flux corrected transport

g Gram

I Current

IPA Isopropanol

KCl Potassium Chloride

kHz kilohertz

MHz megahertz

mL millilitre

mV millivolt

mW milliwatt

n negative ion density

NAB Nitroazobenzene

NaCl Sodium Chloride

nm Nanometer

p positive ion density

PDMS Polydimethylsiloxane

Pt Platinum

R Resistance

T Temperature

V potential

W Ion velocity

Chapter 1

Introduction

1.1 Introduction

The movement of electric charge is responsible for many different effects in a broad range of systems. This can be through charge transfer from one material, or molecule to another or just the redistribution of charge in a system. This thesis looks at the effect of the movement of charge in two different systems. One system is that of the movement of ions in a liquid in the presence of an external electrical field, studying the so called Electrical Double Layer[1]. The other system is that of a molecular heterojunction with a molecular layer sandwiched between two electrodes[2]. These are two very different systems, but the role played by the position and movement of electrical charge is important in the behavior of both.

1.2 Electrical Double Layer

Microfluidics is a rapidly growing field of study. One of the areas of research is using micro electronics as sensors to detect biological entities in vitro.[3, 4, 5] Typically the buffer solution used for biological materials is a saline solution

which has a reasonably high concentration of salts (NaCl, KCl, etc...) which means it has a high concentration of positive and negative ions which have a known mobility. The combination of microelectronics and saline solutions naturally leads to the formation of electrical double layers which screen the electric field created by an applied bias between two electrodes. If the electrical double layer has time to form this can change the potential applied to a biological material between the electrodes significantly. In these types of experiments an AC bias is applied and a high frequency (MHz range) is chosen with the assumption that the potential is switching faster than the electrical double layer can form. However this has yet to be confirmed experimentally and one of the experiments in this thesis will be looking at this question.

The equations governing the behavior of the the electrical double layer in a 1-D system are[6]

$$\frac{\partial n}{\partial t} = \frac{\partial(\mu_n n E)}{\partial x} + \frac{\partial}{\partial x} \left(D_n \frac{\partial n}{\partial x} \right) \quad (1.1)$$

$$\frac{\partial p}{\partial t} = -\frac{\partial(\mu_p p E)}{\partial x} + \frac{\partial}{\partial x} \left(D_p \frac{\partial p}{\partial x} \right) \quad (1.2)$$

$$\frac{\partial^2 V}{\partial x^2} = \frac{e}{\epsilon_r \epsilon_0} (Z_p p - Z_n n) \quad (1.3)$$

where n is the negative ion density, p is the positive ion density, E is the electric field. D_n and D_p are the negative and positive ion diffusion coefficients, μ_n and μ_p are the negative and positive ion mobilities. The valence number of the negative and positive ions are represented by Z_n and Z_p , the magnitude of the electronic charge is e , and the dielectric constant of the fluid is ϵ_r

The first term on the right hand side of equations 1.1 and 1.2 is an advective term, which causes the charges to flow in one direction because of the electric

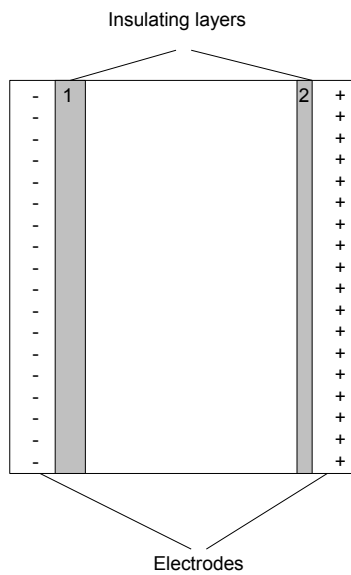
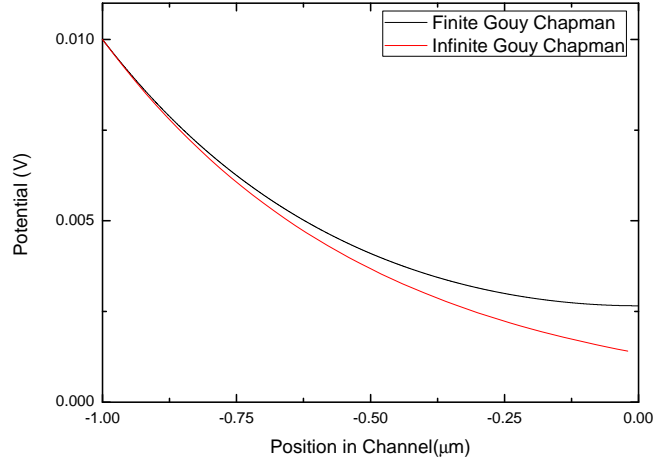
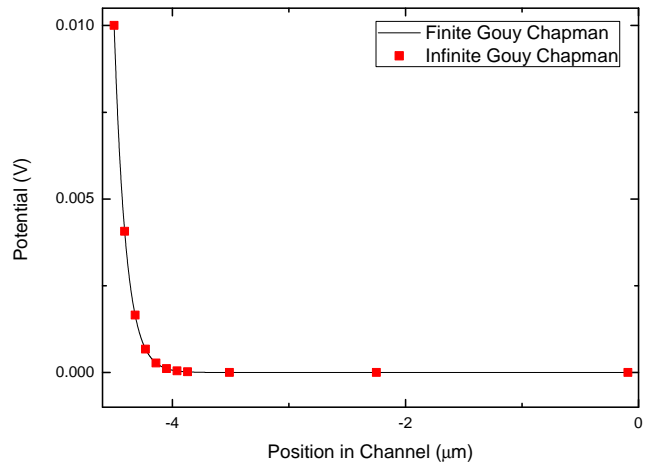


Figure 1.1: Geometry of a simple cell that could study the formation of the electrical double layer. Two electrodes are separated by two dielectric layers and a microchannel that can be filled with fluid. The positive and negative charges on the electrodes represent a voltage, ΔV applied across the electrodes.



(a)



(b)

Figure 1.2: (a) has the Debye length, $\lambda_D = 500nm$, the channel width, $d = 1\mu m$ and the potential across the channel, $V_0 = 10mV$ and shows the difference between the semi infinite and the parallel plate Gouy-Chapman solutions which is significant. (b) has the Debye length, $\lambda_D = 100nm$, which is larger than for the smallest concentrations that will be used in the experiment, channel width, $d = 4.5\mu m$, which is half of the channel length of the final device and the potential across the channel, $V_0 = 10mV$ and shows very good agreement between the parallel plate and semi-infinite Gouy-Chapman solutions.

field and the second term is a diffusion term. Equations 1.1, 1.2 and 1.3 need to be solved simultaneously with the proper boundary conditions to get a solution for the ion behavior.

The equilibrium behavior of the system can be found in the case of a small potential. In this approximation the solution is called the Gouy-Chapman solution for a semi-infinite system [7] where the potential, V is given by

$$V = \frac{2k_bT}{e} \ln\left(\frac{1 + \gamma e^{-\kappa x}}{1 - \gamma e^{-\kappa x}}\right) \quad (1.4)$$

where κ and γ are given by

$$\kappa = \sqrt{\frac{2e^2\rho_0}{\epsilon_r\epsilon_0 k_B T}} \quad (1.5)$$

$$\gamma = \tanh\left(\frac{eV_0}{4k_B T}\right). \quad (1.6)$$

The electric field, E is the negative derivative of the potential,

$$E = -\sqrt{\frac{8\rho_0 k_B T}{\epsilon_r\epsilon_0}} \sinh\left(\frac{e\phi_0}{2k_B T}\right). \quad (1.7)$$

However, the system being studied is not a semi-infinite system. The Gouy-Chapman solution, modified for a parallel plate system, has been found in the low potential ($<25\text{mV}$)[8] regime and is given as

$$V = V_0 \frac{\cosh\left(\frac{x}{\lambda_D}\right)}{\cosh\left(\frac{d}{\lambda_D}\right)} \quad (1.8)$$

where $\lambda_D = \frac{1}{\kappa}$ is the Debye Length and d is the distance from one electrode to the middle of the channel.

Since the Debye length is the characteristic length scale of the electrical double layer, (as well as a property of the bulk fluid), if $\lambda_D \approx d$, then there

will be an appreciable difference between the parallel plate and semi-infinite Gouy-Chapman solutions (figure 1.2a), however, if $\lambda_D \ll d$ the solutions are effectively the same as can be seen in figure 1.2b.

1.3 Molecular Junction

Molecular based electronic devices have become very popular to investigate. In this study molecular junctions which consist of a carbon based molecular layer and insulating oxide layer are sandwiched between two transparent metal electrodes. (Quartz/Cr/Au/C/Molecule/SiO₂/Au)[9]

A schematic of the sample can be seen in figure 1.3 which shows the 5nm transparent platinum electrode on the quartz substrate with a chromium adhesion layer. The carbon layer is used to adhere the molecular layer, either 9, 10 Anthraquinone (AQ) or Nitroazobenzene (NAB) through an electrochemical deposition. On top of that is a thin (10-15nm) insulating layer and lastly another transparent electrode. The resultant sample is optically transparent and able to be electrically excited. In previous work[9] on these molecular junctions in-situ optical absorbance spectroscopy was performed on the molecular junctions using a broad broadband light source.

The range of the wavelength of the broadband light source was $\lambda = 320 - 820nm$ and voltage pulses were applied to the molecular junction. Then changes in the absorbance were measured. Figure 1.4a shows the change in absorbance of the NAB molecular junction to a -4V and to a +4V pulse. Local maxima and minima can be seen at $\lambda \approx 420nm$ and $\lambda \approx 550nm$. Figure 1.4b shows the change in absorbance of the AQ molecular junction as well as the change in absorbance of a Fluorene molecular junction which was used as a control molecule in this work. The AQ shows local maxima and minima

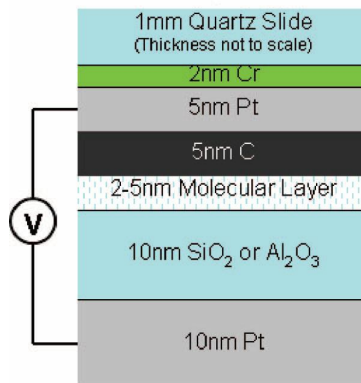


Figure 1.3: Schematic of molecular junction sample where the molecular layer is either 9, 10 Anthraquinone (AQ) or Nitroazobenzene (NAB). The Cr layer is used as an adhesion layer for the transparent Pt electrode. The C layer allows the molecule to bond to the junction. The insulating layer prevents current from flowing from the top transparent Pt electrode to the bottom electrode. Reprinted in part from [9]. Copyright 2008 American Chemical Society.

in the same range as the AQ molecule. The voltage pulses applied to the molecular junctions in this work ranged from 100's of milliseconds to several seconds, and corresponded to possible chemical reduction of the molecular layer with an applied voltage bias. This suggests the ability to dynamically change the energy levels in a molecular junction with an applied bias. A next step would be to change the time scale of the applied bias on the molecular junctions to see if changes in energy levels can be observed on faster time scales. This work will explore the behavior of the molecular junctions on time scales short enough to eliminate chemical reduction as a mechanism for any optical changes of the sample. Because of the stronger changes in absorbance of the two molecules near $\lambda = 420nm$ and $\lambda = 530nm$ continuous wave lasers in the blue ($\lambda = 410nm$) and in the green ($\lambda = 532nm$) will be used in transmission mode through the samples.

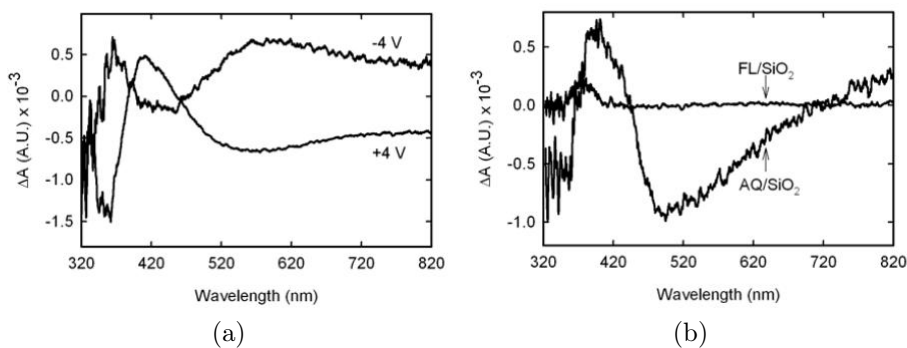


Figure 1.4: (a) shows the change in absorbance of the NAB molecular junction to a -4V and a 4V pulse that was applied for 100ms and caused reduction of the NAB molecular layer and the changes in the absorbance spectrum. (b) shows the change in absorbance of the AQ molecular junction to a -4V pulse applied for 100ms and compared to the control Fluorine molecular junction with the same -4V pulse. Reprinted in part from [9]. Copyright 2008 American Chemical Society.

1.4 Charge Transport

The transport of charge plays an important role in both the behavior of molecular junctions and the formation of the electrical double layer. Chapter 2 of this thesis will discuss the fabrication of the devices used in both of these sets of experiments. Chapter 3 will discuss the optical and electric experimental setups for the experiments involving the molecular junctions. In Chapter 4 the Flux Corrected Transport simulation of the formation of the electrical double layer formed between two blocking electrodes will be discussed. The experiment involving the microfluidic device designed and built to look at the effects of the electrical double layer formation will be discussed in Chapter 5, and lastly the conclusions from this work will be discussed in Chapter 6.

Chapter 2

Device

2.1 Microfluidic Capacitor Design

2.1.1 Introduction

To study the formation of the electrical double layer a simple device is desired. The simplest way to do this would be with a parallel plate capacitor structure that is modified to have fluid between the plates which can be seen in Figure 2.1. Furthermore, since varying concentrations of ionic fluids will be used, there needs to be at least one insulating layer between the plates to prevent current flowing from one plate to the other and to prevent any chemical reactions from happening at the electrode surface. Since the capacitance of a parallel plate capacitor is inversely related to the distance between the two plates ($C = \frac{A\epsilon}{d}$), the two plates need to be placed fairly close together. Lastly, the device needs to easily interface with the function generator and oscilloscope that controls the experiment. The device also has to allow for easy cleaning of the ionic solutions and a simple way to inject the fluid between the plates. Lastly, the fabrication technique will have to allow for varying the thickness of the insulator between the plates to study the effect of this insulating layer.

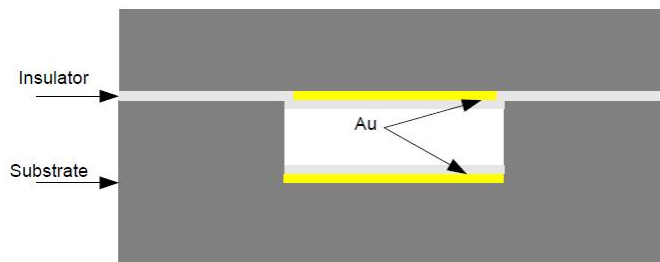


Figure 2.1: The desired design needs to have two electrodes separated by a microchannel and an insulating layer to ensure no current flows from one electrode to the other. The insulating layers are parylene to prevent any current to flow from the fluid in the channel through the electrodes into the external circuit, as well as preventing any electrochemical reactions to happen on the surface of the electrodes. The entire device will be fabricated on 0211 glass substrates.

Another guide for device specifications comes from simulations[6] in which a parallel plate capacitor area of 1 cm^2 and a distance between the plates of $1\text{ }\mu\text{m}$ was assumed. This simulation also has an insulating layer of 10nm . All of these simulation parameters should be kept in mind, and every attempt should be made to use similar physical parameters so comparison can be made with these results. The best route is to use microfabrication techniques to fabricate this device.

2.1.2 Design

A few possible designs were explored and will be discussed. The first attempt was a very simple design which involved lithographically patterning a 1cm^2 electrode on glass slides with thin Chromium/Gold films. The insulating layer used was SiO_2 which was evaporated onto the surface with an electron beam evaporation system. The gap between the two glass slides was created by depositing aluminum through a shadow mask to create aluminum pillars on both sides of the patterned electrodes on one of the glass slides. This design, although simple, suffered from a few problems that could not be overcome.

The first problem was the SiO_2 film. From the deposition process the film was under a lot of stress, and when liquid was applied to it, cracks started to form on the entire domain. This allowed water to reach the electrode and it no longer functioned as an insulating layer. This problem was resolved by using SiO_2 layers thicker than 200nm, but that takes the insulating layer thickness farther away from using ideal simulation parameters for experimental comparison. The other problem was the aluminum pillars. When the two plates were aligned they needed to be secured together. This force was enough to change the pillar thickness and eventually bringing the plates into contact, which damaged the SiO_2 layer and destroyed the capacitor behavior of the device. These issues caused this design to be abandoned.

The next attempt was to make a complete microfluidic device out of polydimethylsiloxane (PDMS) with lithographically patterned capacitor plates. The insulating layer for this device would be PDMS as well, which would allow for the two plates to be easily bonded together. One of the electrodes would be deposited on a glass slide, and then the PDMS would be spun on, and then cured. The microchannel would be cast in PDMS on a patterned piece of Silicon. The back side of this PDMS structure would be bonded to another glass slide to give it strength and the second capacitor plate would be deposited at the bottom of the microchannel on the PDMS. Lastly, the two plates would be aligned and bonded together creating a closed microfluidic capacitor cell. One possible problem with this design is that PDMS can absorb water, and possibly when ionic solutions were used it could absorb some of the ions, which could change the dielectric properties of the PDMS, making experiments unrepeatable. Also, with a closed cell, the only way to clean it would be to pump fluid through the small channels, which would make cleaning very slow. Before these problems became an issue, serious fabrication

problems were encountered. Although a glass plate was bonded to the back of the molded PDMS, it still remained very flexible. This caused the deposited gold layer to have large cracks in it. Not all of the electrodes maintained conductive behavior. Also, enough tests weren't done to see if the conductivity degraded over time, or because of adding and removing fluid to a finished cell. Before PDMS is cured, it is quite a viscous fluid. Spin coating the PDMS only achieved 10 micron layer thickness. Diluting the PDMS with hexane[10] decreased the viscosity, but the thinnest layer achieved this way was still in the single micron range. The last problem with this design related to the flexibility of the PDMS. When attempting to bond the two plates together it bonded unevenly, often leaving large sections without a proper bond. This could cause the entire cell to become delaminated when fluid was injected into the cell. Because of these issues this design was also abandoned.

The third design involves fabricating a microfluidic device out of glass instead of PDMS and not bonding the plates together, so that cleaning is easy and so that fewer samples need to be made. The cleaning can be done by rinsing each individual plate with either water or acetone/IPA, which makes it more thorough and significantly faster. Lastly, Parylene N was used as the insulating layer. Parylene N was deposited using the SCS PDS 2010 Parylene deposition system. Parylene N is a crystalline, linear polymer (poly para-xylylene), which has good dielectric and insulating properties. Also, films can be made anywhere from several angstroms to 10's of microns in thickness. The deposition is done by taking a specific weight of Parylene N and vaporizing it. Parylene N does not have a liquid phase so it provides a conformal coating on the substrate, which can later be measured using a Profilometer (Alpha Step 250) or an Ellipsometer (VASE).

This third design is the one that was ultimately successful and the specific

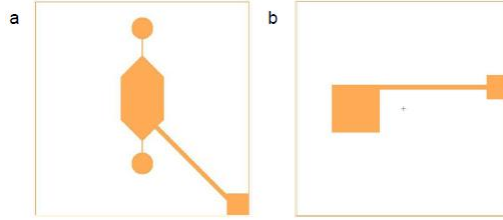


Figure 2.2: Top and bottom plate mask designs made in L-Edit. a) Bottom plate mask design with fluid ports which opens up the possibility to have pressure driven fluid injection. The center has the 1cm^2 electrode in the middle if the fluid injection structure and the contact pad on the bottom right with a thin connecting wire. b) Top plate mask design with 1cm^2 electrode near the middle on the left and the contact pad on the right. When the two plates are aligned, the two contact pads will not be covered by glass from the other plate so they can be connected to the function generator and oscilloscope.

details of the fabrication will now be discussed. The dimensions of each of the chips were approximately $5\text{cm} \times 5\text{cm}$ with a $1\text{cm} \times 1\text{cm}$ contact pad placed near the middle in such a fashion, so that when they were aligned there was uncovered glass from each chip, so that a lead can be patterned on and a contact pad for each chip can be available to solder on to. Figure 2.2a shows what will now be referred to as the top plate, and Figure 2.2b shows what will now be referred to as the bottom plate. The bottom plate had a microchannel etched into the glass before the electrodes were deposited. The microchannel will be etched in the exact same pattern so that electrical contact isn't compromised as the gold is deposited on the etched side walls.

2.2 Device Fabrication

To do the lithography steps photomasks needed to be designed and fabricated. Photomasks consist of patterned Chromium on $5'' \times 5''$ glass substrates. Three masks were made in total, one for the top plate, and two for the bottom plate. All three masks were designed using L-Edit and the design was exported into the GDSII format for use on the Pattern Generator (Heidelberg DWL-200).

The mask for the top plate was a positive photomask, which means that it blocks the exposing UV light where the electrode will be and has Cr in the yellow region in figure 2.2a. The second mask was a negative mask of figure 2.2b, where the UV exposing light passes through where the electrodes will eventually be. This is so that the Cr/Au can first be removed to etch the microchannel. The third mask uses the same design as the second mask, but is instead a positive mask. This allowed etching the unwanted Cr/Au after the second deposition step is done.

The first step in the fabrication process is to properly clean the 4" x 4" 0211 (Paragon Optical Company, Inc) glass substrate. This was done with a Piranha solution (3:1 H_2SO_4 : H_2O_2) for 15 minutes. Next a thin film of Cr/Au was deposited in a Lester Magnetron Sputtering System. The substrate was securely loaded into the rotatable substrate holder above the targets. The system was closed and pumped down to approximately $1 * 10^{-6}$ Torr base pressure using a cryopump. Next, an argon gas was input into the system and the cryopump valve was adjusted until a pressure of $7.0 * 10^{-3}$ Torr was maintained with the argon gas. The power supply was set at 300W for Cr and 75W for Au. The Cr was deposited first for 3 minutes ($\approx 15nm$) and then the gold was deposited for 15 minutes $7.0 * 10^{-3}$ Torr for a total film thickness of approximately 90nm. This was not measured further, as the University of Alberta Nanofab has a prescribed parameter list for desired thicknesses and the thickness of the electrodes isn't important in this experiment as long as they are conducting. The Cr layer is a standard pre-deposition layer for Au on glass and acts as an adhesion layer allowing good adhesion of the Au on the substrate.

After depositing the Cr/Au film on the substrate, was diced into the correct size. This was done using a Diamond Touch Dicing Saw. To get the correct

size each 4'' x 4'' substrate was cut twice to yeild four, approximately 5cm x 5cm chips.

The next process step is the lithography step. For the top plate (Figure 2.2a) only one lithography step is needed. This uses the positive mask created using the same design as figure 2.2a. A film of HPR 504 photoresist was spun on each chip using a Solitec Spinner with 10 seconds at 500rpm to spread the resist over the chip and 40 seconds at 4000rpm to thin the resist layer. The substrates were then baked in an oven at 110^o C for 30 minutes. After the substrates had cooled they were aligned with the mask in the mask aligner (ABM). Once aligned the substrate was brought into contact with the mask and held there with the contact vacuum. The substrate was exposed to UV light for 4 seconds, which is timed by the mask aligner. The exposed resist was developed using 354 Developer, which is mixed in the Nanofab, for approximate 20s. Since the features are very large the development time need not be precise, and when the developing was finished it could be determined by eye, when the residue appeared to be washed away.

Next, the unwanted Cr/Au were removed to leave only the electrode, protected by the patterned photoresist. The Cr and Au etch solutions are pre-mixed by the Nanofab. The chip is first submerged in the Au etch for approximately 20s. This time can be adjusted if the etching isn't completed after 20s. The chip is then thoroughly rinsed with de-ionized water and dried with nitrogen gas before it is submerged in the Cr etch for approximately 20s. Some of the Cr gets oxidized sometime between the deposition and lithography steps, so after the chip is thoroughly rinsed in de-ionized water and dried with nitrogen again it is dipped back into the Au etch for 1 or 2 seconds to remove the CrO_x . After one final rinse with de-ionized water and final dry with nitrogen, the photoresist was ready to be stripped with acetone, then the acetone was

immediately rinsed off the chip with IPA because acetone leaves a residue on the substrate. The substrate was cleaned with Piranha once more to make it ready for the Parylene N deposition.

Once the Parylene N was deposited onto the chip the fabrication of the top plate is complete, however, under normal conditions Parylene N does not bond well to glass, which is most of the area of the substrate. Fortunately the parylene deposition system has a recipe for a solution that promotes adhesion of the Parylene to the glass. This solution is made by mixing equal parts of IPA and water and then adding 1 % of the total volume of this mixture in Silane 174. This adhesion promotion solution is then left overnight, allowing a chemical reaction to take place. Before use, the adhesion promotion solution is tested to make sure it will be effective. This is done by taking 10-15mL of it in a small beaker and dropping a few small grains of potassium permanganate. If the solution is effective it will turn a yellowish colour after swirling it around for a few seconds. If it is not effective it will turn bright pink. Once the effectiveness of the adhesion promotion solution was determined the chip needs to be submerged in it for about 15 minutes. After it has been submerged for 15 minutes the chip was allowed to drip dry for another 15 minutes, and lastly rinsed with IPA for about 30 seconds. The chip was dried with nitrogen and it is ready for deposition.

The Parylene Deposition system (SCS PDS 2010) is very simple to operate. It can be used to deposit Parylene N or C, so a few parameters need to be set depending on the particular deposition being done. For this deposition the vaporizer was set to 160°C, and the deposition pressure was set at 59 mTorr. The thickness of the Parylene N film is controlled by the weight put into the vaporizing chamber. The range of thicknesses achieved were from 3nm (0.5g) to 375nm (5.4g) and the relationship between the weight and deposited thick-

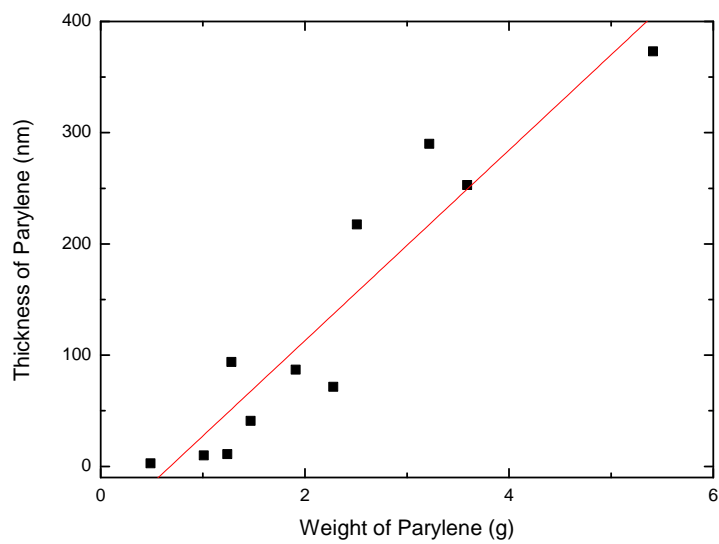


Figure 2.3: Shows the linear relationship between the weight of the parylene N used in the deposition to the thickness of the parylene N film. Because the parylene N provides a conformal coating a minimum weight is necessary to get any coating on the sample, as the parylene N will coat the deposition chamber as well. All depositions used a furnace temperature of 160°C and a pressure of 59mTorr.

ness is shown in figure 2.3. The slope of the linear fit shows the approximate thickness added for an increase in the start weight of the parylene N powder, which works out to be $(85 \pm 10)nm/g$. Much of the parylene that gets vaporized ends up adhering to different parts of the deposition system, and the x-intercept represents a guideline for the minimum weight of parylene that needs to be used in order to get a film, which was $(0.7 \pm 0.4)g$. During the fabrication of the devices, the Parylene deposition system had to be repaired and this probably accounts for the fairly large errors present on the deposition data. Once the deposition parameters are set and the substrate loaded the chamber is pumped down and the program is run. The substrate is then removed after the Parylene deposition system has vaporized and deposited all of the Parylene N. Lastly, the system is cleaned thoroughly to remove all of the remnant Parylene N.

The first several steps of the bottom (microchannel) fabrication were the same as with the top plate. Starting with a 5cm x 5cm glass chip with a Cr/Au layer HPR 504 photoresist was spun on (500rpm for 5 seconds and 4000rpm for 40s) and the photoresist was baked for 30 minutes at 110 C, the negative mask version of Figure 2.2 b was used to expose the chip to UV light for 4s. Then the chip was developed with 354 Developer and lastly etched with Au/Cr/Au etch to remove the Au/Cr/ CrO_2 . The Au was removed from where the electrode will be on the completed chip. The next step is glass etching with a Hydrofluoric acid (HF) based glass etchant.

To ensure the backside of the substrate is not etched, tape is placed on the backside. Using HF requires extra safety precautions. During all work with HF full acid gear (gloves, mask and apron) were worn and a supply of calcium chloride solution was on hand to neutralize any spilled glass etchant, as well as for cleaning after the process was completed. The glass etchant was

placed on a magnetic stirrer and the chip was submerged in the etchant for 5 minutes to determine the etch rate. After 5 minutes the chip was removed and immediately placed in water to stop the etching. The chip was then washed in a dump rinser for 5 cycles to ensure it was safe to handle. The thickness was measured and the etch rate determined. Then the chip was placed back in the solution for the time calculated for the desired microchannel depth. The final thickness for all of the channels was approximately 9 microns. It was actually achieved in the 5 minutes of the etch rate test because the etchant was fresh. Then the glass etchant was put away and any beakers and other tools used were rinsed with the calcium chloride solution before being washed with water to ensure no HF contamination.

The bottom plate was then stripped of its photoresist with acetone, then rinsed with IPA and dried with nitrogen. Then the Au/Cr/CrO_x was removed using Au etch/Cr etch/Au etch to leave a chip with only a patterned microchannel. Piranha was used once more to make sure the bottom plate was sufficiently clean for the next Cr/Au deposition step. This was done exactly the same as the first Cr/Au deposition in the Lester Magnetron Sputtering system, with the only difference being the 5cm x 5cm chips being loaded instead of 4" x 4" wafers.

The bottom plate was once again spin coated with HPR 504 resist and baked. This time the positive mask of Figure 2.2b was used and aligned using the mask aligner (ABM). This was the only lithography step that required precise alignment and used the microscope lenses on the mask aligner to ensure that the substrate was aligned in x, y and θ with the mask. This ensures that the electrode is entirely inside of the etched microchannel and that some of the area is not coming up the side walls and into the glass surface that will come into contact with the other chip. Once the alignment was achieved the

substrate was brought into contact with the mask and held in place with the contact vacuum. The exposure was once again done for 4 seconds, and the bottom plate was developed in 354 Developer. The unwanted Au/Cr/ CrO_x was removed using Au etch/Cr etch/ Au etch and the photoresist stripped with acetone and rinsed with IPA. The last step to complete the bottom plate fabrication is to clean it with Piranha to remove any photoresist residue.

With the microfabrication complete, a sample holder was machined to hold both the top and bottom plate so that they could be aligned and brought into contact. A previously made sample holder that had SMA connectors held in place was used as the base. Then two aluminum pieces had recesses milled into them that were the width of the plates but not as long (so there would be overhang to solder wires onto the contact pads). These recesses were milled to a depth of approximately 250 microns (half the thickness of the 0211 glass substrates used) to hold the chips reasonably still, but to ensure that the plates were in physical contact with each other. In the aluminum piece that holds the top plate a “window” was milled the entire way through the aluminum where the capacitor plate would sit so that alignment could be done. Lastly threaded holes (for 10-32 bolts) were drilled and tapped in the bottom plate holder and wider alignment holes were drilled in the top plate holder to give some alignment room for the holder. The bolts have a spring that slips around it and a large washer to ensure that it presses on the top plate holder while it is fastened into the bottom plate holder. The sample holder with device in can be seen in figure 2.4, which shows the electrodes in the window and the overhangs that have the contact pads.

Thin wires were soldered to all of the contact pads. Because the wire was soldered to a thin film ($\approx 90nm$) a careful procedure was used. One end of the wire was bent into a small loop, then dipped into resin flux. Then it was

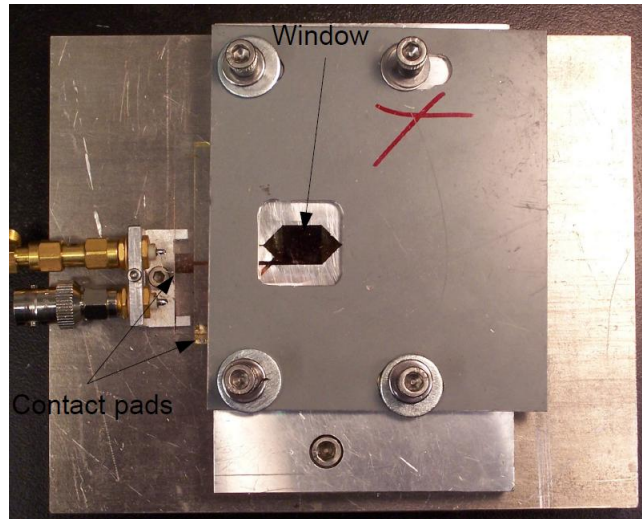


Figure 2.4: Sample holder with top and bottom plates together. The window allows alignment of the two electrodes and wires on the contact pads are soldered to the SMA connectors to the left of the pads. The over hang for both glass plates is visible. The screws are springloaded to apply even pressure to the top plate to resist the surface tension of the fluid trying to separate the plates. The alignment of the electrodes is done using a stereo microscope.

run through a bead of solder on the tip of the soldering iron to get a small amount of solder onto the wire. Next a small spot of flux was applied to the contact pad. A piece of glass was put on top of the chip to insure no flux splattered onto the rest of the chip during soldering. The small loop was brought onto contact with the contact pad and flux and the soldering iron was quickly touched to the wire, which created a small solder joint without damaging the thin film contact pad.

To inject the fluid, a micropipette was used. Several drops of fluid are placed on the bottom plate electrode and then the top plate holder with top plate in the recess (held with double-sided Scotch tape) is positioned and lowered onto the bottom plate. The bolts were loosely fastened so that alignment can be done under a stereo microscope. Once the alignment is complete the bolts were completely fastened, and then the wires soldered to the SMA connectors. The excess fluid was pushed into the rest of the microchannel, as

well as onto some of the rest of the chip. This initially created a problem, as glass is hydrophilic and Parylene N is hydrophobic. The resulting capillary forces pulled the fluid out of the channel. This changed the capacitive behavior rather dramatically in real time and the microchannel emptied completely in approximately 1 hour. Two possible solutions were found. The first solution would be to deposit a very thin layer of Parylene N on the bottom plate. The second would be to treat the surface of the bottom plate with a Silane solution to make the surface hydrophobic.

Depositing a thin layer of Parylene N has the advantage of guaranteeing that capillary forces won't pull the fluid out of the channel because not only will both surfaces be hydrophobic, but both will have the same contact angle. The deposition also won't change the dimensions of the channel because the Parylene deposition is a conformal coating due to the vapor/solid transition and it won't accumulate in the corners or be thicker in the channel compared to on the chip surface, which would happen if a thin film was spin coated on. However, since the Profilometer (Alpha Step 250) used has a minimum resolution of 5nm, the thickness of a very thin film becomes very difficult to measure accurately. This makes modeling the different dielectric layers in the capacitor challenging. Lastly, if any absorption of ions from the high concentration of ionic fluids were to occur it would be very difficult to use the same bottom plate for the multiple top plates.

Treating the surface of the bottom plate with Silane will change the surface from hydrophilic to hydrophobic, however it doesn't ensure the same contact angle, which will still give a possibility of capillary forces removing fluid from the channel, however it would decrease this rate of removal. This has the added benefit of not adding an extra dielectric layer to the system which then needs to be added to the model. The treatment is also very simple to apply.

The chip was cleaned with IPA, then the Silane solution was dropped on and held on the chip for 15 seconds. Lastly, the chip was thoroughly rinsed with methanol and dried with nitrogen gas.

Both methods were tried. The Silane method produced a similar contact angle on the glass to that of the parylene, however, it made the decay times approximately 10 times longer than before the Silane solution was applied. The reason was not understood, so the silane method was abandoned. Thus, depositing a thin layer of parylene N onto the bottom plate was chosen as the method to eliminate the capillary forces.

After all of the samples were fabricated and the experiment was mostly complete, it was discovered that the Profilometer made very inaccurate measurements of the parylene film thicknesses. All of the measurements were repeated with an Ellipsometer (VASE). The Ellipsometer was used in reflection mode, so it could measure the thickness directly over the electrodes. To do this a model of the substrate had to be created. A patterned substrate without parylene deposited on it was used to get the properties of the substrate and specific Au/Cr layer to ensure that the results would be accurate. This gave much more accurate results than the Profilometer, and in some cases very different thickness measurements.

2.3 Molecular Junction Fabrication

The molecular junction[9] structure was patterned on a Quartz substrate cut into a rectangular shape about 1cm in width and 2-3cm in length. The first step was to pattern the bottom semi transparent electrode onto the quartz substrate. This was done using a shadow mask and depositing a Cr adhesion layer of approximately 2nm, followed by an approximately 5nm layer of

platinum, and then a 5nm layer of carbon. All three are deposited using an electron beam evaporation system and the shadow mask used had a $500\mu\text{m}$ wide “bar” opening aligned with the long dimension of the substrate. Shadow mask has four of these “bars” so multiple junctions can be patterned onto the same chip. The next step is to deposit the molecular layer of nitroazobenzene (NAB), which was done by submerging the substrate into a conductive solution and performing cycles of cyclic voltametry, sweeping the voltage from 400mV to -600mV at sweep rate of 200mV/s. The number of cycles of cyclic voltametry will be referenced in the molecular name. (i.e. NAB-4 means that four cycles were performed for the deposition) After the molecular layer was deposited electron beam evaporation was used again to deposit a thin layer (10-15nm) of SiO_2 was deposited on top of the molecular layer, and then a top of the oxide layer a 10nm layer of Pt or Au is deposited.

Chapter 3

Molecular Junction Experiments

3.1 Introduction

On the time scale of 100's of milliseconds to 10's of seconds the absorbance of NAB molecular junctions has been investigated using in-situ optical absorbance spectroscopy.[9] This study found changes in absorbance when a bias was applied across the molecular junction which can be attributed to the chemical reduction of the molecular layer. When biases are applied for shorter times it eliminates chemical reduction and other slower processes from governing optical behavior. There might be other processes happening at these time scales, but but this has not previously been explored. In this experiment this bias will be an AC sine wave, applied across the electrodes of the molecular junction and the transmission of light through the junction of a continuous wave laser (at 410nm and 532nm) will be monitored. The wavelengths of the lasers were chosen because they are close to where the largest changes in the absorbance were observed for the DC biases. The transmission will be observed over a fairly large frequency range (1kHz-100kHz) and over a range of applied bias voltages (10mV-500mV). Since the active area of the molecular junction

is larger than the focused spot size of the laser ($500\mu m$ by $500\mu m$ active area compared to sub $100\mu m$ diameter laser spot size) scans over the entire active area will also be done to ensure that the sample behaves consistently over the entire active area. As well as these optical experiments, the current/voltage characteristics of the samples will be tested.

If reduction of the molecule is what causes the observed changes it is reasonable to assume that the motion of electrons in the molecular layer, even if it is not full electron transfer, will cause some changes in the absorbance even if the molecules don't have time to complete the reduction and gain an electron. A very simple order of magnitude estimate can be made by comparing the shorter times of the applied bias here to get an estimate of the absorbance. For full reduction a change in absorbance, $\Delta A \sim 10^{-3}$ was found for a $100ms$ (10Hz) pulse. A frequency of 1kHz would correspond to a characteristic time of $1ms$ and would give a maximum absorbance change of $\Delta A \sim 10^{-5}$ assuming that there is a linear change in ΔA with time. Since this experiment looks at transmission, then the measured signal should be $\Delta T \leq 10^{-5}$ for a 1kHz bias and should get smaller as the frequency increases.

3.2 Samples

The samples for this experiment were provided by the McCreery group, and they were fabricated as described in Section 2.3. Three different types of samples were provided. The first was a control sample, which consisted of Quartz/Cr(2nm)/Pt(5nm)/C(5nm)/SiO₂(10nm)/Pt(10nm). This sample will be used to compare to the samples with a molecular layer to make sure that any observed behavior is caused by the molecule, and not by any of the other layers in the molecular junction. The second sample consisted of

Quartz/Cr(2nm)/Pt(5nm)/C(5nm)/NAB-1(2nm)/SiO₂(10nm)/Pt(10nm). NAB-1 refers to the number of cyclic voltametry cycles performed and corresponds to a thickness of the NAB-1 layer of $\approx 2nm$. The third substrate consists of Substrate/Cr(2nm)/Pt(5nm)/C(5nm)/NAB-4(5nm)/SiO₂(10nm)/Pt(10nm) where NAB-4 has a thickness of $\approx 5nm$. Each sample had multiple junctions that were tested and a representative sample of the results will be described.

3.3 Optical Set Up

The simple optical set up can be seen in figure 3.1. The laser can be either a blue or green laser which can have its intensity adjusted with the use of a variable neutral density filter as an attenuator. The lens, with a focal length of approximately 20cm is used to focus the beam onto the sample. The long focal length was chosen because the sample holder and stage (Melles Griot Nanomax-HS 3D) is large and forces the photodiode detector to be placed 10-15cm behind the sample. A shorter focal length results in too much spread of the laser light from the time it passed through the sample at its focus to when it reaches the detector. The photodiode in the top of figure 3.1 is used to to independently monitor the power of the laser to monitor any drift.

3.4 Laser Stability

Initially the green (532nm) laser being used was a Verdi diode laser. This laser is used for multiple experiments, and was brought to the sample via a fibre optic cable. This created problems with the power stability of the beam, which fluctuated up to approximately 10% over the course of several hours, which was shorter than some of the experiments to be performed. A different 532nm laser (Millenia) was tested, which still had power stability problems, of

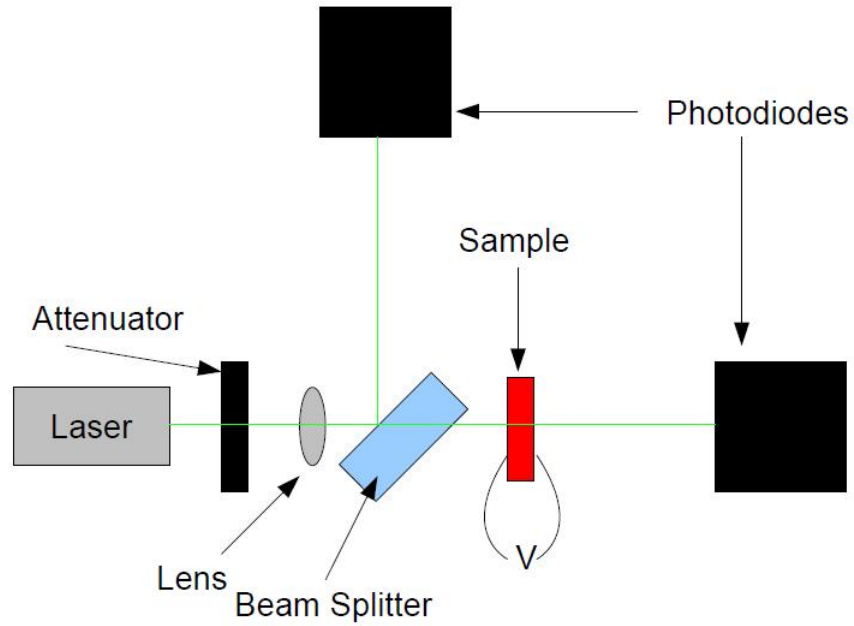


Figure 3.1: Shows a schematic of the optical set up to look at the transmission through a molecular junction. The laser is either a blue (410nm) or green (532nm). The attenuator was used to control the intensity at the sample. The lens used has a focal length of $\sim 20cm$. The beamsplitter splits the beam into two so that the drift of the laser can be monitored separately from the modulated signal through the sample. The signal is then measured by a lock-in amplifier after a pre-amplifier. The sample is biased using the internal oscillator from the lock-in amplifier with frequencies between $1kHz - 100kHz$ and amplitudes between $100mV - 500mV$.

approximate 5% over similar time scales as the Verdi.

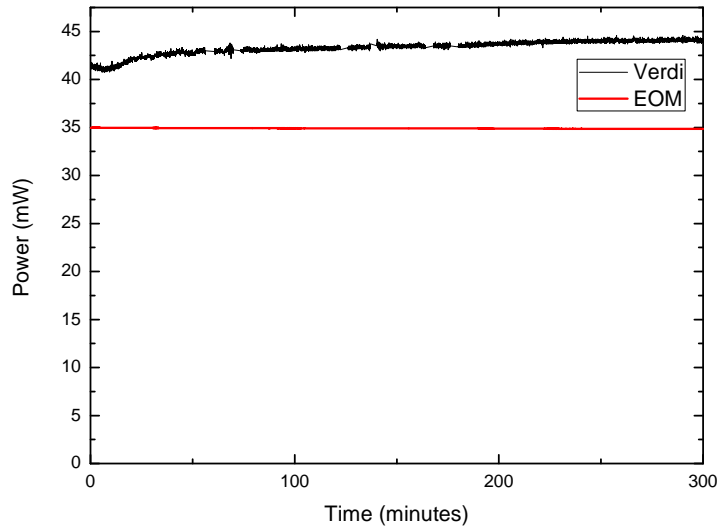
The improvement in power stability can be seen in figure 3.2. Figure 3.2a compares the stability of the Verdi diode laser through the fibre coupler to that of the Millenia beam after it has passed through an Electro-Optic Modulator (LASS II - Con Optics). The EOM was used to modulate the amplitude of the beam. Although in principle the EOM should operate effectively over any range of desired amplitudes which are smaller than the minimum power of the laser, it was found that the EOM worked most effectively between 50-60%. To get the power of the EOM beam in figure 3.2a the initial beam power of the Millenia was turned up to $\approx 60mW$. Figure 3.2b shows the power of the EOM magnified to show the change of scale of the drift. The drift shows approximately an order of magnitude improvement in its stability, which is significant but still requires monitoring for possible corrections.

3.5 Current Voltage Characteristics

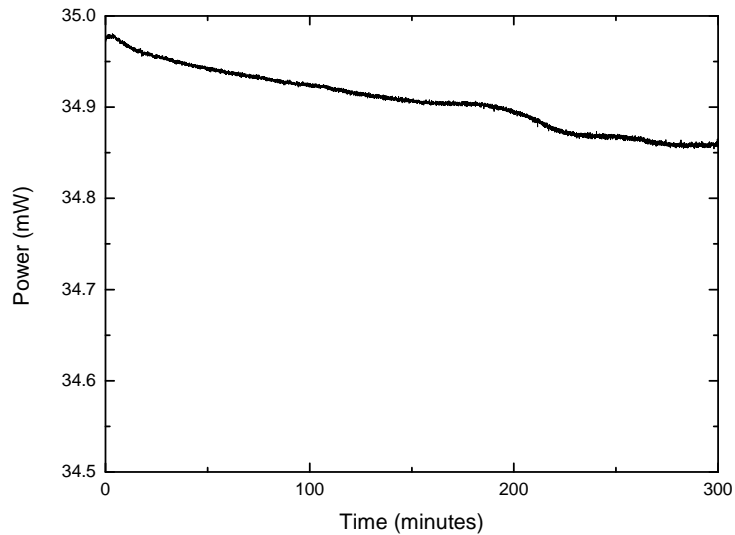
Trying to measure the resistance of the molecular junctions using standard multimeters gave different values of the resistance, which suggests that the current/voltage characteristics of the molecular junction are non-linear.

3.5.1 Experimental Set Up

A schematic of the experimental set up to measure the I-V characteristics of the molecular junction samples is shown in figure 3.3. The simplest way to do this is to apply a DC voltage in steps across a resistor ($2.085M\Omega$) wired in series with the sample. A Data Acquisition device (6221 DAQ - National Instruments) was used to apply the DC voltage. Two multimeters, (HP3478A) were used, one to measure the voltage drop across the resistor, which was used



(a)



(b)

Figure 3.2: (a) Shows the stability of the laser power with the Verdi laser through the fibre optics and the stability of the Millennia after passing through the Electro-Optical Modulator (EOM) for 5 hours. The laser power is reduced by the EOM but is significantly more stable. (b) shows the stability of the beam after passing through the EOM zoomed in which shows that although the power is more stable it still fluctuates $\sim 0.3\%$ over 5 hours.

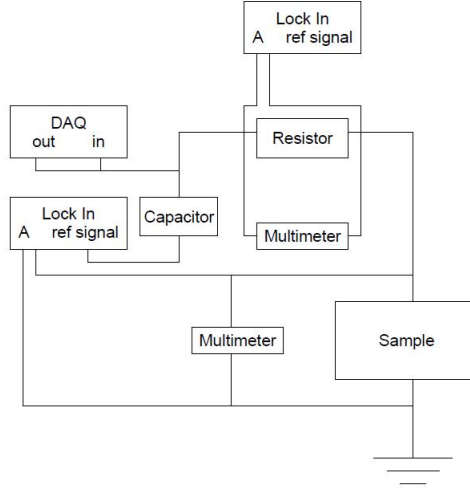


Figure 3.3: Schematic of the electronic set up to measure the I-V characteristics of the molecular junction. The DC signal is from the DAQ and the AC dither is from the lock-in on the left. The potential drops across the sample and the resistor are both measured with multimeters. The capacitor is used to protect the lock-in internal oscillator from the DC voltage. The DC voltage measurements are recorded from the multimeters with the DAQ and the measurements from the lock-ins are measured using a GPIB connection. The entire system is controlled by a custom labview program.

to determine the current in the circuit, and another to measure the voltage drop across the sample. Also of interest is the derivative, $\frac{dI}{dV}$ vs V . If the voltage steps are small enough this could be calculated numerically, however it is better to measure $\frac{dI}{dV}$ directly to avoid any numerical errors. This can be done by adding an AC dither to the DC signal. By taking the AC reference signal off of a Lock in Amplifier (SRS 830 DSP) and coupling that into the DC signal from the DAQ, $\frac{dI}{dV}$ can be measured directly. It is determined by measuring the AC signal with one Lock in Amplifier from the resistor to determine ΔI and using a second Lock in Amplifier to measure the AC voltage signal across the sample to get ΔV . Although $\frac{d^2I}{dV^2}$ was not investigated in this experiment, it could be monitored by looking at the second harmonic in both lock in signals (2f). The I-V curves were made using a custom Labview (National Instruments) program which controlled the DAQ, which outputted

the DC voltage and recorded the output values on one of its input channels. The program also controls the Lock-in Amplifier’s amplitude and frequency of the AC dither applied to the DC voltage steps and records the voltage drops across the sample and resistor. It also allows the amount of averaging to be set for each voltage step.

3.5.2 I-V Results

The I-V curves in figure 3.4a show linear behavior of the control sample with no molecule present. The control sample has the lowest resistance ($133.8\text{k}\Omega$). For the two NAB samples, the resistance is determined by finding the slope of the curve in the low voltage regime where it behaves linearly. The NAB-1 sample has the largest resistance ($665.8\text{k}\Omega$) and doesn’t show linear behavior like the control sample does. The NAB-4 sample has a resistance between the control and NAB-1 sample ($415\text{k}\Omega$), which doesn’t make sense when thinking of the molecular layer as only an extra insulating layer. In such a model, it would be expected for the NAB-4 sample to have the largest resistance since it is the thickest, having a 10nm layer of SiO_2 and a 5nm layer of NAB. However this suggests the NAB’s interaction with the rest of the substrate is dependent on its thickness, and also on the bias between the electrodes. The NAB-4 sample also shows the most pronounced nonlinear behavior in the I-V curves.

Figure 3.4b shows the $\frac{dI}{dV}$ vs V curve for the 3 samples. The control sample has the noisiest results and doesn’t appear to have any interesting behavior in the voltage range measured, however something could just be hidden within the noise. After many attempts, the noise was not able to be removed from the control sample results. The NAB-1 sample showed two symmetric increases in the $\frac{dI}{dV}$ signal at $\pm 0.2\text{V}$, which are well above the noise and were repeatable. The NAB-4 sample showed similar symmetric spikes in the $\frac{dI}{dV}$ signal, however

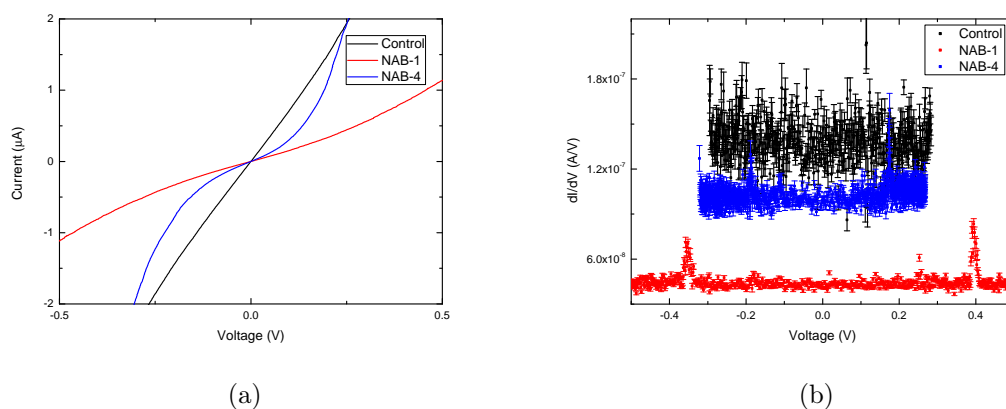


Figure 3.4: (a) Shows a representative current voltage curve for the 3 different samples. The control sample has the lowest resistance. NAB-1 has the highest resistance, and NAB-4 has the most nonlinear behavior of the 3 samples. The control sample has a resistance of $133.8k\Omega$, NAB-1 has a low voltage resistance of $665.8k\Omega$ and the NAB-4 sample has a low voltage resistance of $415k\Omega$. (b) shows a $\frac{dI}{dV}$ vs V curve. The control sample has a very noisy signal, with no noticeable features. Both the NAB-1 and NAB-4 curves are less noisy with distinguishable peaks present. NAB-1 has two peaks that appear at $\sim \pm 0.4V$ and the NAB-4 sample has two peaks that appear at $\sim \pm 0.2V$.

they appeared at $\pm 0.4V$. This would suggest that the cause of these spikes was not something connected with the energy levels in the molecule, but leaves open the possibility that it is related to the thickness of the molecular layer, however no further investigation was done on this.

The characteristics of some samples changed over time. As the samples aged the nonlinear behavior became closer and closer to linear, and in some cases, if the sample was damaged the resistance would drop by several orders of magnitude, suggesting that the insulating layer was compromised.

3.6 Raster Scan

The sample in the optical setup is mounted on a 3 axis translational stage, which allows it to be moved in x, y, or z, where x corresponds to the position of

the sample in the direction of the beam, the y is horizontal and perpendicular to the beam, and z is vertical and perpendicular to the beam. The y and z translation ability is used to move the sample in order to perform a raster scan over the surface of the molecular junction. An AC bias is applied to the sample using the internal oscillator of a Lock-in Amplifier. The lock-in amplifier's internal oscillator has a range of available frequencies from less than 1Hz-100kHz. The range of frequencies used will be from about 1kHz-100kHz so that long integration times on the lock-in can be avoided so the measurement doesn't take too long. The photodiode detector is connected to a pre-amplifier (SRS SR560) which is then connected to the Lock-in Amplifier which is able to detect the amplitude and phase of the laser as it is modulated when it passes through the sample. The DC level of the photodiode is also monitored after the signal is passed through the pre-amplifier. The DC amplitude on the photodiode, and the amplitude and phase from the lock-in are all recorded with a DAQ. The rasterscan was performed by a custom Labview (National Instruments) program written to control the DAQ and read the voltages the photodiode and the lock-in amplifier. Importantly, this program automates the movement of the sample in the translation stage and allows control of the number measurements are taken at each position for averaging.

The DC amplitude as a function of position is a transmission profile of the surface of the sample. This allows the structure of the junction to be checked, and also makes it easier to determine what signal in the phase and amplitude are from the sample by knowing what is the active area and what is not. Figure 3.5 shows the DC transmission for the NAB-1 and NAB-4 samples with 532nm and 410nm lasers respectively. Both plots show the least transmission in the center, revealing where the active area is. Also both have an approximately constant amplitude showing no strange features that affect

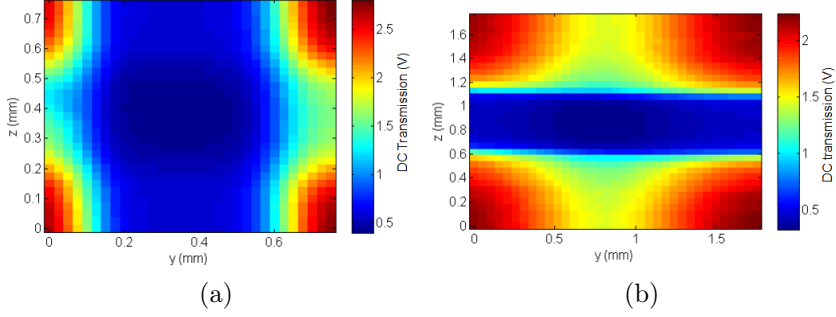


Figure 3.5: (a) shows the DC amplitude raster scan of the NAB-1 chip with the 532nm beam with a modulating amplitude of 400mV at 1kHz. Since the DC amplitude is measured in transmission, the smallest magnitude of the signal is where the active area is, because it's the thickest and transmits the least. The active area can be seen in the middle, with the highest magnitude of the transmission in the corners where there is only the substrate. The top, bottom, left and right in the middle each have one electrode, so there is less transmission than through the glass, but more than in the active area of the molecular junction. (b) shows the DC amplitude of the NAB-4 chip with a 410nm beam of 400mV at 1kHz. Similarly to (a) the smallest magnitude signal is in the center where the active area is. In both (a) and (b) the units for the colour scale are Volts and each spatial step is $50\mu\text{m}$ in both the y and z directions.

the DC transmission, such as scratches to the surface, or pieces of dust or other particles. It shows the most transmission in the corners where the laser only passes through substrate, and shows an intermediate level of transmission over each individual electrode. Because of using different optical powers, and the photodiode detector having different sensitivities to the different wavelengths the scales of the two graphs do not match up.

From the lock-in Amplifier, the modulation of the beam at the frequency of the driving voltage on the sample can be measured. Figure 3.6a shows this amplitude measurement for an NAB-1 junction taken with a 532nm beam and the sample modulated at 400mV and 1kHz. The active area of the sample has a significantly larger signal than that of the background. (which includes both the single electrodes where they haven't intersected and the glass) Although the entire active area has a signal larger than the background, the corners

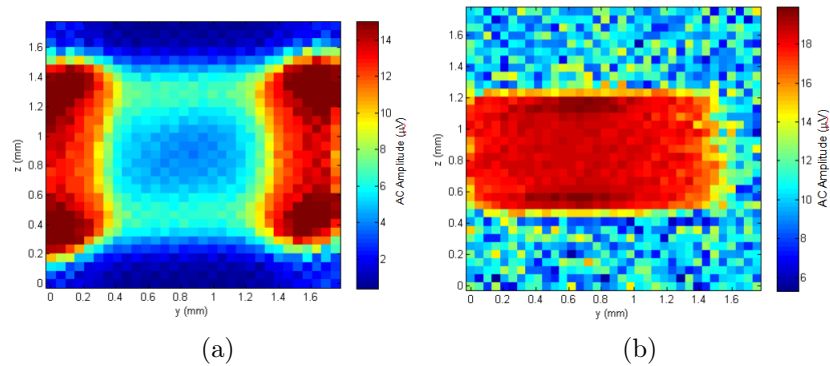


Figure 3.6: (a) shows the change in amplitude of the sample surface for an NAB-1 active area at 1kHz and 400mV driving voltage of the sample and a 532nm beam. The active area can be seen, with the largest amplitude being at the four corners, but the entire active area having a signal that stands out from the almost zero signal of the surrounding single electrodes and glass. (b) shows the change in amplitude of the sample surface for the NAB-4 sample with a 410nm beam and a driving voltage of 400mV at 1kHz. The active area can clearly be seen in this raster scan as well, however the corners do not show a pronounced increase in the amplitude. For both (a) and (b) the units of the colour scale are μV and each spatial step is $50\mu m$ in both the y and z directions.

have the largest signal, and the edges have a larger signal than the middle. This is quite possibly some artifact of the edge, and not really a characteristic of the sample. Figure 3.6b shows the results for the amplitude on an NAB-4 molecular junction illuminated with a 410nm beam. The sample is again modulated at 400mV and 1kHz. This rasterscan had a larger scan field, but the active area of the sample stands out from the background quite strikingly as well. However, this sample does not have the strong increase in amplitude associated with the corners and edges and has a pretty consistent amplitude.

As well as measuring the change in amplitude of the modulated signal, the lock-in amplifier measures the phase change of the signal. Figure 3.7a shows the phase over the scanned region of the NAB-1 sample with a 532nm beam and a sample modulation of 400mV at 1kHz. The active area stands out as a consistent region with a constant phase change compared to the

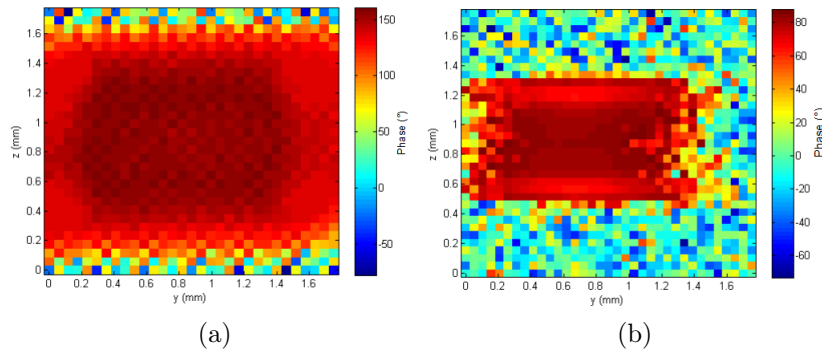


Figure 3.7: (a) shows the phase change of the 532nm beam passing through the NAB-1 sample, which is modulated at 400mV and 1kHz. The active area can be seen in red and orange having a consistent phase. Outside the phase changes rapidly and the lock-in amplifier was not actually locked into a signal when off of the active area. (b) shows the phase change of a 410nm beam passing through the modulated NAB-4 sample at the same driving amplitude and frequency as in (a). The active area can be seen to stand out from the background again here, with the background having a signal that was not locked into. For both (a) and (b) the units of the colour scale are degrees and each spatial step is $50\mu m$ in both the y and z directions.

background which changes rapidly over spatial position. The raw data showed wild fluctuations off of the active area, showing that there wasn't a strong enough modulation in the signal to be picked up by the lock-in amplifier. Figure 3.7b shows a similar raster scan over the surface of an NAB-4 sample, which is modulated at 400mV and 1kHz and probed with a 410nm beam. Again, the active area stands out strongly from the background, with the background modulated signal too small to be properly picked up with the lock-in amplifier, and having wildly changing phases.

The results showing in figures 3.5, 3.6 and 3.7 show fairly consistent behavior over the surface of the active area. This means that as long as care is taken to keep the beam in approximately the center of the sample (which has an area much larger than the spot size of the beam) that the results of any further studies should be consistent and repeatable. The spatial position of the beam on the active area should not be a particularly sensitive parameter

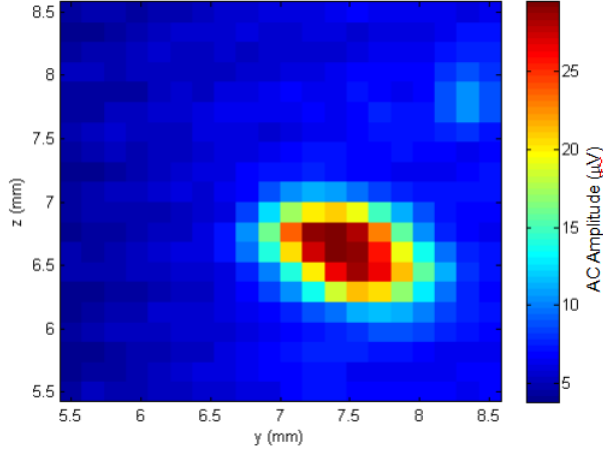


Figure 3.8: Shows the active area surface profile of a sample which was damaged and had its I-V characteristics dramatically changed. Measurements taken with 532nm beam at 1kHz and 400mV. The units of the colour scale are μV and each spatial step is $50\mu m$ in both the y and z directions. This was taken on a larger sample where the entire active area was larger than the range of the stepper motors, so the entire region of the graph is on the active area. Since the large spike in signal corresponded to a large change in resistance, falling by approximately 2 orders of magnitude, it could be damage to the insulating layer at this position.

and one that doesn't need to have any special precautions taken in order to control.

As mentioned in section 3.5.2, samples can get damaged. When this happens, dramatic changes in the electrical properties were observed (Resistance drops from $\sim 100k\Omega$ to $\sim 100\Omega$) and similarly, dramatic changes were observed in the modulated laser amplitude through the sample. Figure 3.8 shows part of the active area of a large sample (4mm x 4mm) that was modulated with a 400mV bias at 1kHz and was illuminated by a 532nm beam. A large increase in the amplitude was observed over a small area of the active area. This suggests that there was some localized damage in that region, and combined with the drop in resistance measured in the I-V characteristics, this suggests that there might have been a pinhole in the insulating layer, or some other physical damage.

3.7 Modulation

Now that the molecular junctions have been characterized with their I-V curves, and their behavior over the entire active area has been found to be consistent, the samples can be modulated over the range of frequencies from 1kHz-100kHz and voltages from 100mV-500mV. Another custom Labview program was written for this function, which records the frequency and amplitude of the applied bias, as well as the modulated amplitude, phase, x and y signals from the lock-in amplifier. Since the internal oscillator of the lock-in is used for the bias, the Labview program controls everything through the GPIB connection between the lock-in and the computer. The program controls all of the features of the lock-in, so they can be set from the computer, as well as specifying how many measurements will be taken at each frequency and voltage step for averaging.

Many measurements were taken with both the 532nm and 410nm beams. Figure 3.9 shows the amplitude of a few runs for an NAB-1 sample with a 532nm beam at 400mV bias from 500Hz-100kHz. It shows that some of the features remain qualitatively similar, however the amplitude from run to run was not constant and not reproducible. The first peak for all three runs happens at approximately 25kHz, but has a different amplitude for all three runs. The second peak occurs at approximately 75kHz and for the first and third run happens at the same amplitude, however for run two happens at a much higher amplitude. Also, the amplitude of run three is higher leading up to the second peak than in the first run. The changes in amplitude don't seem to follow a trend with time, so this doesn't appear to be attributable to aging of the sample. It was not checked, but it could be as a result of temperature fluctuations in the lab, which were known to fluctuate by a few degrees Celsius over the course of days. The same problems with reproducibility were seen

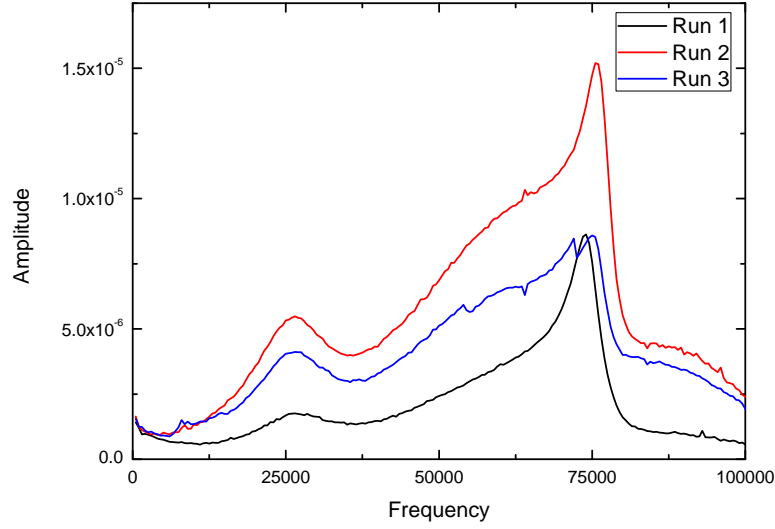


Figure 3.9: Shows the amplitude for three separate runs sweeping the frequency from 500Hz-100kHz with 500Hz steps at 400mV at 532nm on the NAB-1 sample. This shows that all of them have a qualitatively similar shape, with the first peak at around 25kHz and the second peak at around 75kHz, but the amplitude of the first peak is different for all three runs. The first and third runs have similar amplitudes for the second peak, but different slopes to get there, and this amplitude is different from the second run. These runs are representative of the poor quantitative reproducibility for the samples.

with using the 410nm beam.

Figure 3.10a shows the amplitude of the control sample with no molecule layer as well as the NAB-1 sample. Both samples have the same qualitative shape, suggesting that the shape of the curves is not related to the molecular layer. Because of the poor reproducibility of the curves it is difficult to draw any solid conclusions. Figure 3.10b shows the results for the phase for the same two samples. The behavior of the phase is very similar from one curve to the other after approximately 20kHz. The local minimum in the phase at 75kHz appears to line up exactly with the peaks in the amplitude signals, and the control sample is shifted slightly to the right compared to the NAB-1 sample. Figure 3.11 shows NAB-1 and NAB-4 illuminated with a 410nm beam through

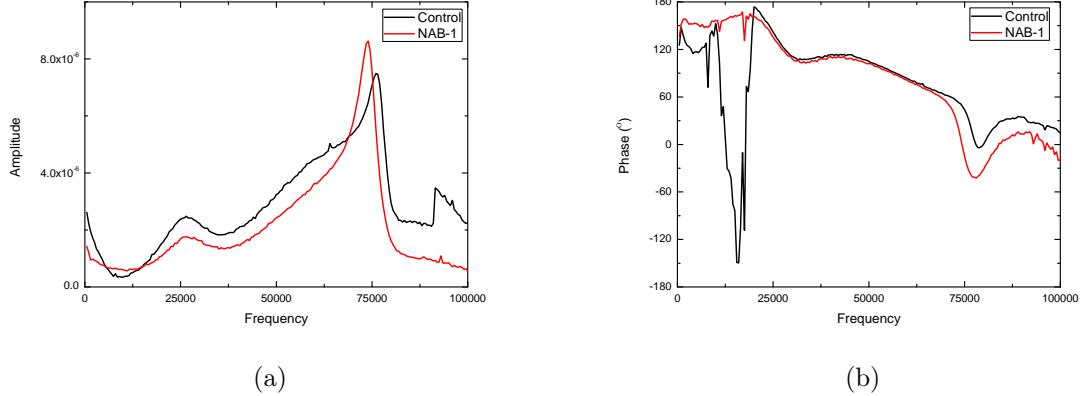


Figure 3.10: (a) Shows results for the amplitude while varying the frequency from 500Hz-100kHz with frequency steps of 500Hz at 400mV for the control sample and the NAB-1 with a 532nm beam. (b) shows the phase results for the same samples, showing a pretty consistent phase over the range of 25kHz-70kHz or so. As for any individual sample the results varied from run to run no real conclusions can be drawn from this figure.

a frequency range of 500Hz-100kHz at a bias of 400mV. Similar to the 532nm beam, two peaks are seen, however the shape of the peaks is different and the second peak seems to be shifted slightly to the left to approximately 65kHz.

Figure 3.12 shows the amplitude signals for four experiments done on the same sample at 400mV and a frequency range of 500Hz-100kHz with a 410nm beam. The black curve shows the signal from the active area of the sample, showing two peaks similar to the peaks that have been seen previously in all of the amplitude vs frequency plots for the molecular junctions. The red curve shows the signal off to the side of the active area on just bare quartz. The blue and purple curves show the amplitude signal on the horizontal top electrode, and the vertical bottom electrode respectively. All of these signals have the same qualitative shape, further indicating that the peaks are not caused from the molecule, but most likely from the substrate. As the amplitudes are known to change from run to run, it is not certain if the strength of the signals is related to the position of the beam was, or just a coincidence of the variation

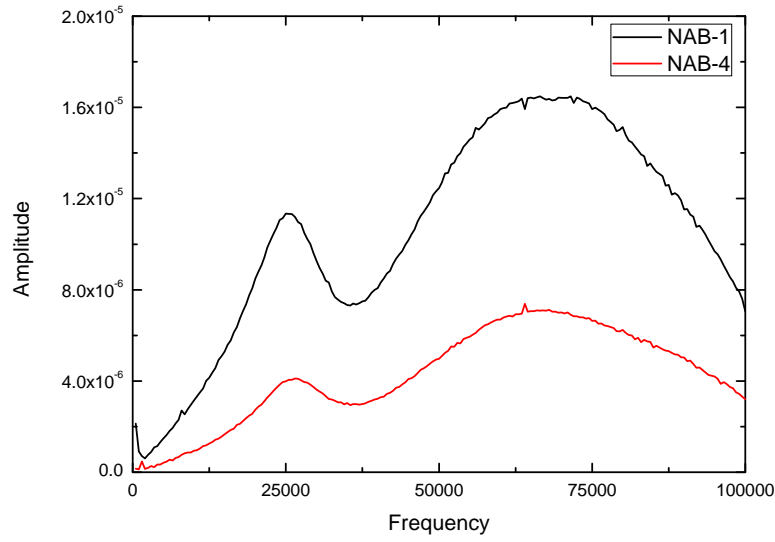


Figure 3.11: Shows the amplitude for NAB-1 and NAB-4 samples for a frequency range of 500Hz-100kHz with 500Hz frequency steps at a 400mV bias illuminated with a 410nm beam. Similarly to when the sample is illuminated with a 532nm beam, there are two peaks, except they are broadened with the 410nm beam.

from run to run.

As well as varying the frequency, some runs were done varying both the frequency and amplitude. Figure 3.13 shows a representative plot of one of these experiments with the NAB-1 sample. The frequency was varied from 500Hz-100kHz and the AC bias was varied from 100mV-500mV and the sample was illuminated with a 532nm beam. Similarly to the previous experiments done at a constant AC bias, figure 3.13a shows that for the amplitude there are still two peaks, and that as the AC driving voltage is increased the amplitude increases. The first peak is still at approximately 25kHz and the second peak is still at approximately 75kHz. The amplitude does not appear to undergo any qualitative changes as the AC bias changes, only changes in its scale. Figure 3.13b shows the phase from the same experiment and shows the same decrease in the phase as the frequency increases as seen in figure 3.10b, as an increase

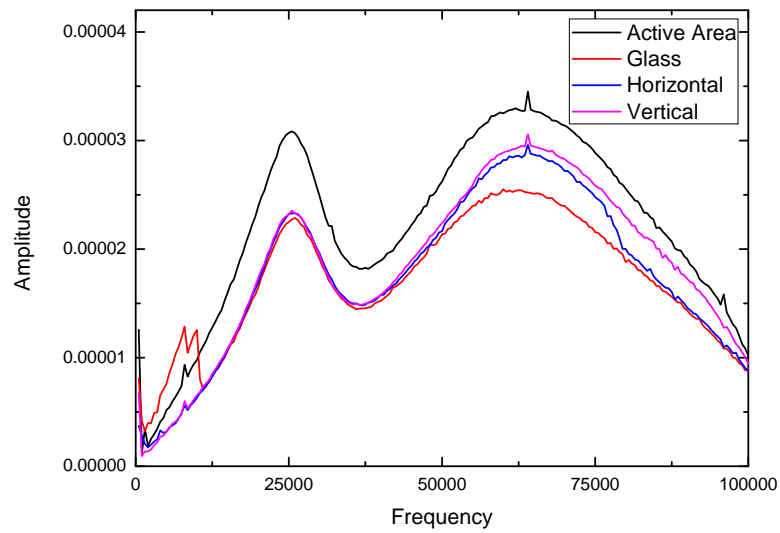


Figure 3.12: Shows the amplitude measurements for an NAB-1 sample with an AC bias of magnitude of 400mV from 500Hz-100kHz with 500Hz frequency steps and a 410nm beam. The black curve is with the beam on the active area, the red is off of the active area passing directly through the quartz substrate, the blue curve is with the beam on the horizontal top electrode, but off of the active area and the purple curve is off of the active area on the vertical bottom electrode.

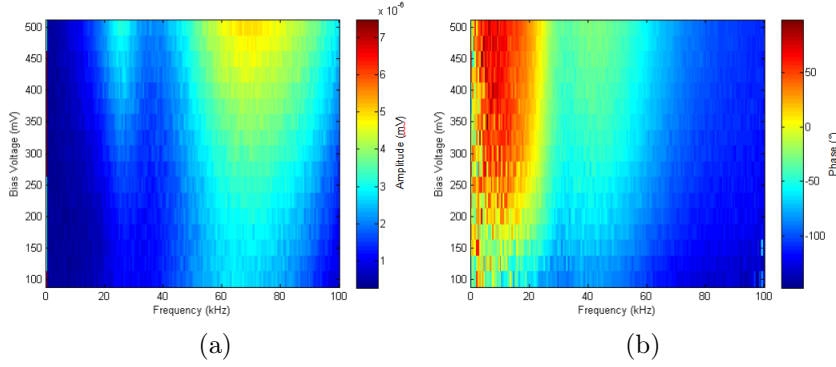


Figure 3.13: (a) shows the amplitude response of an NAB-1 sample as the frequency was varied from 500Hz-100kHz in 500Hz steps and the AC bias was varied from 100mV-500mV in 25mV steps with a 532nm beam. The response shows the same frequency dependence as the earlier experiments at a constant bias potential as well as the magnitude of the signal increasing as the bias potential is increased. (b) shows the phase response for the same experiment.

in the phase while the AC bias is increased.

3.8 Experimental Conclusions

In this chapter the experiments performed on the molecular junctions the problems encountered were discussed. The problem with the optical power was solved by introducing an EOM into the system and an order of magnitude improvement in the stability of the optical power was achieved, which provided a better architecture to perform the optical experiments. The I-V characteristics were investigated and the NAB samples were found to exhibit non-linear behavior, with the thicker NAB-4 layer showing stronger non-linear behavior than the NAB-1 sample. The $\frac{dI}{dV}$ vs V curves found symmetric increases at $\pm 200mV$ for the NAB-1 sample and $\pm 400mV$ for the NAB-4 sample, which suggests that these spikes were not related to the specific energy levels of the molecule, but are possibly due to the thickness of the molecular layers.

The first optical experiment performed was to scan the change in amplitude and phase across the entire active area of the sample to see if there was a spatial

dependence of either signal. It was found that the active area had consistent behavior, and as long as the beam stayed near the middle of the sample this should not cause any problems with reproducibility.

Lastly the frequency and bias were both varied at a single spot on the active area to see if the behavior changed in response to frequency of bias. For all of the samples, the qualitative behavior was reproducible, however the amplitude was not quantitatively reproducible. This made solid conclusions difficult to draw, however qualitative conclusions can still be drawn. For both the 410nm and 532nm beams increases in the amplitude were seen at around 25kHz and 75kHz. These were for the control sample, as well as the NAB-1 and NAB-4 samples. On a single sample, when looking at the amplitude response on the active area, on either electrode, as well as just on the quartz substrate, the same qualitative behavior was seen. This suggests that the frequency dependent features were not a result of the molecular layers, but a property of the substrate. Although changes in the absorbance spectrum were found in response to applied voltages at long time scales, at shorter time scales there is no evidence for changes in the transmission that can be attributed to the molecular layers and the signal did not appear to be reproducible enough for a pump probe type of experiment to provide much useful insight into the electron transfer in the molecular layers.

Chapter 4

Electrical Double Layer Simulation

4.1 Introduction

Although much is known about the electrical double layer in equilibrium, analytic solutions for the dynamical behavior can not be derived from equations 1.1, 1.2 and 1.3, so to learn about the dynamical behavior numerical simulations must be done. There have been many simulations done to study the ion behavior at blocking electrodes under the simple geometry presented here. [6, 11, 12, 13] These simulations all use different numerical schemes of varying accuracy. Franceschetti[12] uses a sophisticated PDE package and a finite element scheme as well as breaking up equations 1.1, 1.2 and 1.3 into a system of six coupled first order differential equations. Tankovsky[11] uses the same system of coupled first order differential equations, but uses a first order numerical scheme which suffers from numerical diffusion which increases as the potential increases. This numerical diffusion causes the total ion number of both the positive and negative ions not to be conserved. Both of these simulations use transformations which cast the variables into dimensionless form with the Debye length

$$\lambda_D = \sqrt{\frac{\epsilon k_B T}{4\pi e^2 p_0 (Z_n + Z_p)}} = \frac{0.304 nm}{\sqrt{p_0}} \quad (4.1)$$

and the dielectric relaxation time

$$\tau_D = \frac{\epsilon}{4\pi e^2 p_0 (\mu_n + \mu_p)} \quad (4.2)$$

as the characteristic length and time scales of the system.

The simulation done by Morrow[6] uses a method called Flux-Corrected Transport (FCT) which has been used for plasma physics and gas discharge models[14, 15, 16] as well as a flux limiting method.[17]

The first simulation attempted was the first order method by Tankovsky[11], but it suffered from the numerical diffusion already mentioned. Even at small potential, the size of the microchannel could only be increased out to approximately 10 Debye lengths before the simulation became very inaccurate. As the concentration increases, the Debye length decreases, which means that the characteristic length of the system becomes small compared to the size of the system. This makes the first order method unsuitable and it was abandoned in favor of the FCT method.

4.2 Flux-Corrected Transport Method

4.2.1 Introduction

The FCT algorithm is an algorithm that allows two different types of solutions to be combined in a way that uses the strengths of both solutions and avoids their weaknesses. Equations 1.1 and 1.2 are advective-diffusive continuity equations and have been studied in constant electric fields previously.[18, 19] Certain lower order solutions have the strength of being smoothly varying and

positive everywhere, but the weakness is that they suffer from large amounts of numerical diffusion. On the other hand, higher order solutions suffer from less numerical diffusion and can pick up sharper features, but suffer from oscillations and possible negative solutions, even though these negative solutions are unphysical. FCT allows an accurate solution to be built onto the lower order solution which uses the higher order solution as much as possible without adding the oscillations or any negative and unphysical aspects to the solution. As well as using the ion density, as the name suggests, the density's flux for both the higher and lower order solutions is used to calculate the flux corrected solution. In most of the previous studies the electric field was constant, but in this work, as with the electrical double layer simulation by Morrow[6], equation 1.3 has to be solved simultaneously with the two continuity equations. Lastly the results of the FCT solution will be used to calculate the current flowing in the circuit, which will be compared to the current measured experimentally for the microfabricated devices. Then, in this case the electric field and potential can be compared to the Gouy Chapman solutions (Equations 1.7 and 1.4) to determine the accuracy of the solutions.

4.2.2 The Model

The model for this simulation is a 1 dimensional microchannel between two blocking electrodes. The electrode is blocked by dielectric layers between the electrodes and the microchannel, as can be seen in figure 1.1. This dielectric layer, which experimentally is parylene N, ($\epsilon_{parylene} = 2.65$) causes a potential drop of the initial magnitude of the potential on the electrodes, so the potential in the channel depends on the thickness of the parylene layer, even though the input pulse magnitude is kept constant. The blocking electrodes also ensure that ions don't flow out of the channel, and also prevent the need to model

any chemical reactions that might otherwise take place between the ions and the electrodes. There will only be a non-Faradiac current flowing inside the channel. Like the experiment, the channel length will be $9\mu m$ and two ion species will be used, Potassium, K^+ , and Chlorine, Cl^- . At the boundaries, no ions can flow out of the channel, and no ions can diffuse from the dielectric layer into the channel. This means that at the boundaries the ion mobility, $\mu_p = \mu_n = 0$ and the diffusion constants, $D_p = D_n = 0$.

4.2.3 Lower Order Method

The Lower order method that was found to be non-negative and non-oscillating[19] involved using a differencing of the diffusion term in equations 1.1 and 1.2 at the current time step, and an explicit upwind differencing of the advective term at the previous time step as well as backwards time differencing of the time derivative.

This gives an implicit equation,

$$\begin{aligned}
& -2s_{j-\frac{1}{2}}\tilde{p}_{j-1} + (2 + 2s_{j-\frac{1}{2}} + 2s_{j+\frac{1}{2}})\tilde{p}_j - 2s_{j+\frac{1}{2}}\tilde{p}_{j+1} = \\
& (c_{j-\frac{1}{2}} + |c_{j-\frac{1}{2}}|)p_{j-1}^n + \left(2 - (c_{j+\frac{1}{2}} + |c_{j+\frac{1}{2}}|) + (c_{j-\frac{1}{2}} - |c_{j-\frac{1}{2}}|)\right)p_j^n - (c_{j+\frac{1}{2}} - |c_{j+\frac{1}{2}}|)p_{j+1}^n
\end{aligned} \tag{4.3}$$

where $s_{j+\frac{1}{2}} = \frac{D_p \Delta t}{\Delta x^2}$, $c_{j+\frac{1}{2}} = \frac{\mu_p \Delta t}{2\Delta x}(E_{i+1} + E_i)$, p_j^n is the known solution for the ion density at time step n and \tilde{p}_j is the lower order solution at the time step $n+1$ on a uniform mesh. This implicit equation forms a tridiagonal matrix system which can be solved once the appropriate boundary conditions have been implemented. Many efficient solvers have been written, and for this work the tridiagonal matrix solver from the GNU Scientific Library has been

used. Rather than rederiving equation 4.3 for the negative ion case, the sign of the mobility, μ_n was changed from positive to negative for movement in the opposite direction.

The positive ion flux is given by

$$\phi_{j+\frac{1}{2}}^L = \frac{\Delta x}{2} \left[(c_{j+\frac{1}{2}} + |c_{j+\frac{1}{2}}|) p_j^n + (c_{j+\frac{1}{2}} - |c_{j+\frac{1}{2}}|) p_{j+1}^n - (2s_{j+\frac{1}{2}}(\tilde{p}_{j+1} - \tilde{p}_j)) \right]. \quad (4.4)$$

The tridiagonal matrix, which is in the form

$$\begin{pmatrix} b_0 & c_0 & 0 & 0 & 0 & 0 & 0 & 0 \\ a_0 & b_1 & c_1 & 0 & 0 & 0 & 0 & 0 \\ 0 & a_1 & b_2 & c_2 & 0 & 0 & 0 & 0 \\ 0 & 0 & \dots & \dots & \dots & 0 & 0 & 0 \\ 0 & 0 & 0 & \dots & \dots & \dots & 0 & 0 \\ 0 & 0 & 0 & 0 & \dots & \dots & \dots & 0 \\ 0 & 0 & 0 & 0 & 0 & a_{N-2} & b_{N-1} & c_{N-1} \\ 0 & 0 & 0 & 0 & 0 & 0 & a_{N-1} & b_N \end{pmatrix} \begin{pmatrix} p_0 \\ p_1 \\ \cdot \\ \cdot \\ \cdot \\ \cdot \\ \cdot \\ p_N \end{pmatrix} = \begin{pmatrix} d_0 \\ d_1 \\ \cdot \\ \cdot \\ \cdot \\ \cdot \\ \cdot \\ d_N \end{pmatrix} \quad (4.5)$$

the coefficients equation 4.3 can be written in the form $a_{j-1}p_{j-1} + b_j p_j + c_j p_{j+1} = d_j$. Where $a_{j-1} = -2s_{j-\frac{1}{2}}$ and $c_j = -2s_{j+\frac{1}{2}}$. $b_j = (2 + 2s_{j-\frac{1}{2}} + 2s_{j+\frac{1}{2}})$ are defined everywhere except at the boundaries. Since $s_{j-\frac{1}{2}} = s_{j+\frac{1}{2}} = s$, so

$$a_j = -2s \quad (4.6)$$

$$b_j = (2 + 4s) \quad (4.7)$$

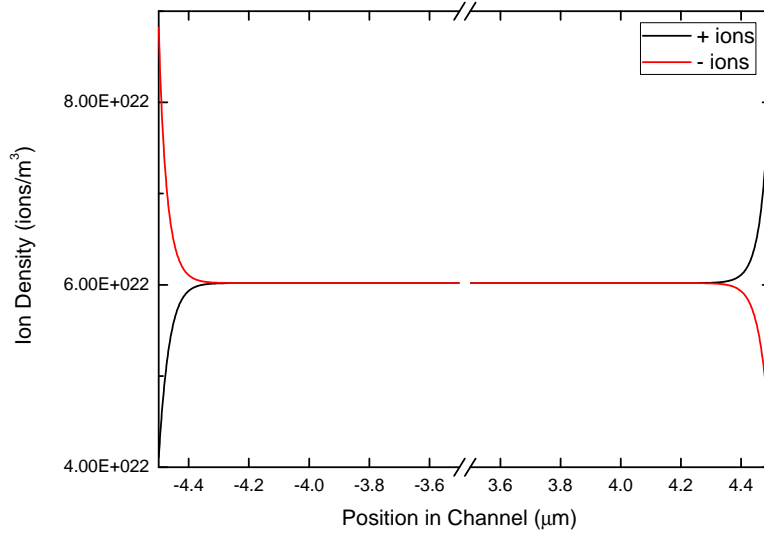


Figure 4.1: Equilibrium ion density for the positive and negative ion solutions for the Low order algorithm. It can be seen that, since the ions being depleted at a boundary are restricted to remain non-negative, there is a visible difference in the magnitude of the depletion compared to the equilibrium and that of the accumulation compared to the equilibrium. The channel width is $9\mu m$, and the concentration of the solution is 0.0001mol/L . At this concentration the cell is 296 Debye lengths and 5921 grid points are used with $\Delta x = 1.5nm$ and an adaptive scheme which calculates a new time Δt for each time step is employed.

$$c_j = -2s \quad (4.8)$$

$$d_j = (c_{j-\frac{1}{2}} + |c_{j-\frac{1}{2}}|)p_{j-1}^n + \left(2 - (c_{j+\frac{1}{2}} + |c_{j+\frac{1}{2}}|) + (c_{j-\frac{1}{2}} - |c_{j-\frac{1}{2}}|)\right)p_j^n \quad (4.9)$$

$$-(c_{j+\frac{1}{2}} - |c_{j+\frac{1}{2}}|)p_{j+1}^n.$$

Equations 4.6, 4.7, 4.8 and 4.9 along with non conducting boundary conditions will allow the simulation to behave appropriately, where at one electrode positive ions will accumulate and negative ions will be depleted, and the opposite will happen at the other electrode. As mentioned in 4.2.2 the conditions at

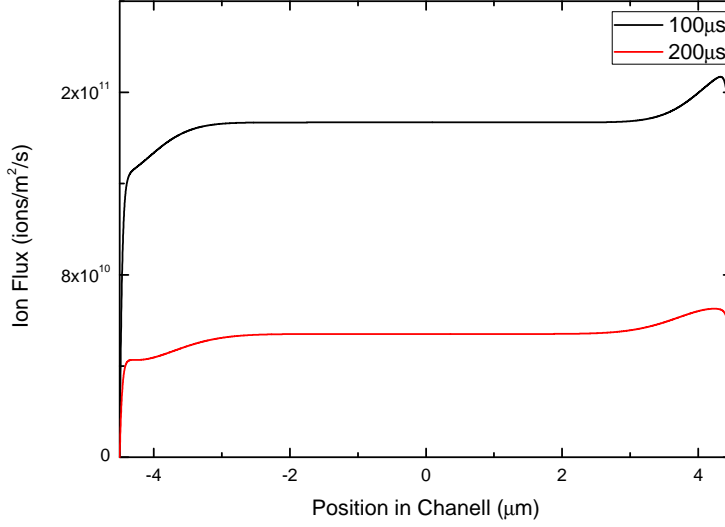


Figure 4.2: Showing the positive ion flux, as calculated from equation 4.4 for two different times. The channel width is $9\mu m$, and the concentration is 0.0001mol/L . At this concentration the cell is 296 Debye lengths and 5921 grid points are used with $\Delta x = 1.5\text{nm}$ and an adaptive scheme is employed to calculate Δt . The slightly lower flux on the left is a result of the imbalance of the depletion of the positive ions at one electrode, and the slightly higher flux at the right is because of the same imbalance of the accumulation of ions at the other electrode.

the boundary are that $\mu_p = \mu_n = 0$ and $D_p = D_n = 0$, which means that $c_{-\frac{1}{2}} = c_{N+\frac{1}{2}} = 0$ and $s_{-\frac{1}{2}} = s_{N+\frac{1}{2}} = 0$. Applying this to equations 4.6, 4.7, 4.8 and 4.9 gives $a_{-1} = 0$, $c_N = 0$, $b_0 = 2 + 2s$ and $b_N = 2 + 2s$ as well. The boundary conditions applied to d_j are

$$d_0 = \left(2 - (c_{\frac{1}{2}} + |c_{\frac{1}{2}}|) + (c_{-\frac{1}{2}} - |c_{-\frac{1}{2}}|)\right) p_0^n - (c_{\frac{1}{2}} - |c_{\frac{1}{2}}|) p_1^n \quad (4.10)$$

and

$$d_N = (c_{N-\frac{1}{2}} + |c_{N+\frac{1}{2}}|) p_{N-1}^n + \left(2 - (c_{N+\frac{1}{2}} + |c_{N+\frac{1}{2}}|) + (c_{N-\frac{1}{2}} - |c_{N-\frac{1}{2}}|)\right) p_N^n. \quad (4.11)$$

Figure 4.1 shows the behavior of the ion density. This shows the accumulation

of positive ions and depletion of the negative ions on the right and the opposite behavior on the left. In the middle the ion density has not changed, and as the concentration of the solution increases, and the Debye length gets smaller the change from the initial ion density to the high ion density at the boundaries happens much closer to the boundary. The ion flux is shown for two different times in figure 4.2 and shows that the ion flux is relatively flat in the middle, with slight dip near the electrode where the depletion occurs and a slight increase near the electrode where the accumulation occurs. This is because the ions can't deplete below zero, although there is not a similar condition at the accumulation electrode, causing a slight asymmetry, which increases as the ion concentration and applied potential increase. The ion flux also goes to zero at both boundaries because of the non-conducting boundary conditions. The decrease in the ion flux as time progresses is because the ions screen the electric field as they accumulate and weaken its effects.

4.2.4 High Order Method

The Higher order method used was taken from[19]. To derive their equation they started with a fourth order finite difference equation for the advective part of equation 1.2[16] and combined that with a second order differencing of the diffusion term in equation 1.2. For a uniform spatial mesh the Higher Order Method equation is

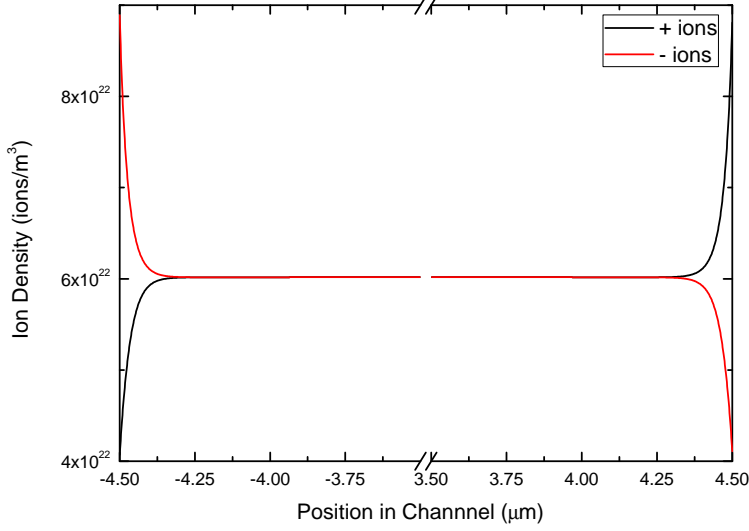


Figure 4.3: Shows the positive and negative ion density at equilibrium for the higher order algorithm. The parameters for this simulation were a channel width of $9\mu\text{m}$ and a concentration of 0.0001mol/L . At this concentration the cell is 296 Debye lengths and 5921 grid points are used with $\Delta x = 1.5\text{nm}$ and an adaptive scheme is employed to calculate Δt .

$$\begin{aligned}
& \left(2 - 3c_{j-\frac{1}{2}} + (c_{j-\frac{1}{2}})^2 - 6s_{j-\frac{1}{2}}\right) \bar{p}_{j-1} + \left(8 + 3(c_{j+\frac{1}{2}} - c_{j-\frac{1}{2}}) \right. \\
& \quad \left. - (c_{j+\frac{1}{2}})^2 - (c_{j-\frac{1}{2}})^2 + 6s_{j+\frac{1}{2}} + 6s_{j-\frac{1}{2}}\right) \bar{p}_j + \left(2 + 3c_{j+\frac{1}{2}} + \right. \\
& \quad \left. + (c_{j+\frac{1}{2}})^2 - 6s_{j+\frac{1}{2}}\right) \bar{p}_{j+1} = \left(2 + 3c_{j-\frac{1}{2}} + (c_{j-\frac{1}{2}})^2 + 6s_{j-\frac{1}{2}}\right) p_{j-1}^n \quad (4.12) \\
& + \left(8 - 3(c_{j+\frac{1}{2}} - c_{j-\frac{1}{2}}) - (c_{j+\frac{1}{2}})^2 - (c_{j-\frac{1}{2}})^2 - 6s_{j+\frac{1}{2}} - 6s_{j-\frac{1}{2}}\right) p_j^n \\
& \quad + \left(2 - 3c_{j+\frac{1}{2}} + (c_{j+\frac{1}{2}})^2 + 6s_{j+\frac{1}{2}}\right) p_{j+1}^n
\end{aligned}$$

again, where $s_{j+\frac{1}{2}} = \frac{D_p \Delta t}{\Delta x^2}$, $c_{j+\frac{1}{2}} = \frac{\mu_p \Delta t}{2\Delta x} (E_{i+1} + E_i)$, p_j^n is the solution at time step n and at mesh point j and \bar{p}_j is the solution of the higher order ion density at $n+1$ and at mesh point j . Equation 4.12 forms a tridiagonal system in the form of equation 4.5 which is also solved by using the tridiagonal matrix solver from the GNU Scientific Library with

$$a_{j-1} = 2 - 3c_{j-\frac{1}{2}} + (c_{j-\frac{1}{2}})^2 - 6s_{j-\frac{1}{2}} \quad (4.13)$$

$$b_j = 8 + 3(c_{j+\frac{1}{2}} - c_{j-\frac{1}{2}}) - (c_{j+\frac{1}{2}})^2 - (c_{j-\frac{1}{2}})^2 + 6s_{j+\frac{1}{2}} + 6s_{j-\frac{1}{2}} \quad (4.14)$$

$$c_j = 2 + 3c_{j+\frac{1}{2}} + (c_{j+\frac{1}{2}})^2 - 6s_{j+\frac{1}{2}} \quad (4.15)$$

$$\begin{aligned} d_j &= \left(2 + 3c_{j-\frac{1}{2}} + (c_{j-\frac{1}{2}})^2 + 6s_{j-\frac{1}{2}}\right) p_{j-1}^n \quad (4.16) \\ &+ \left(8 - 3(c_{j+\frac{1}{2}} - c_{j-\frac{1}{2}}) - (c_{j+\frac{1}{2}})^2 - (c_{j-\frac{1}{2}})^2 - 6s_{j+\frac{1}{2}} - 6s_{j-\frac{1}{2}}\right) p_j^n \\ &+ \left(2 - 3c_{j+\frac{1}{2}} + (c_{j+\frac{1}{2}})^2 + 6s_{j+\frac{1}{2}}\right) p_{j+1}^n. \end{aligned}$$

The same idea is applied for the boundary conditions as for the lower order. $a_{-1} = 0$ and $c_n = 0$, even though, with just the boundary conditions, these would have a constant value of 2. Applying the boundary conditions to b_n and d_n gives

$$b_0 = 8 + 3(c_{\frac{1}{2}} - c_{-\frac{1}{2}}) - (c_{\frac{1}{2}})^2 - (c_{-\frac{1}{2}})^2 + 6s \quad (4.17)$$

$$b_N = 8 + 3(c_{N+\frac{1}{2}} - c_{N-\frac{1}{2}}) - (c_{N+\frac{1}{2}})^2 - (c_{N-\frac{1}{2}})^2 + 6s \quad (4.18)$$

$$\begin{aligned} d_0 &= \left(8 - 3(c_{\frac{1}{2}} - c_{-\frac{1}{2}}) - (c_{\frac{1}{2}})^2 - (c_{-\frac{1}{2}})^2 - 6s\right) p_0^n \\ &+ \left(2 - 3c_{\frac{1}{2}} + (c_{\frac{1}{2}})^2 + 6s\right) p_1^n \quad (4.19) \end{aligned}$$

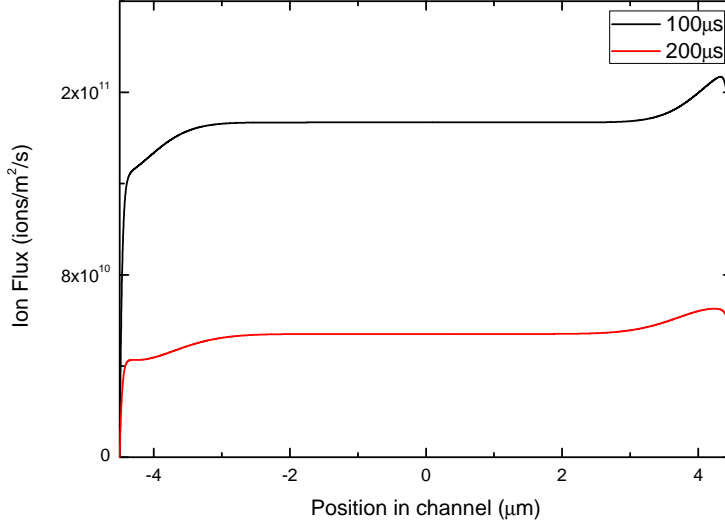


Figure 4.4: shows the ion flux for two different times in the simulation, which shows the flux decreasing with time. Like in the lower order case (figure 4.2) the lower value of the flux on the left is from the smaller amount of depletion of ions at the left electrode with respect to the larger amount of accumulation of ions at the right electrode. The channel width is $9\mu m$ and the concentration is $0.0001 mol/L$. At this concentration the cell is 296 Debye lengths and 5921 grid points are used with $\Delta x = 1.5 nm$ and uses an adaptive scheme is employed to calculate Δt .

$$d_N = \left(2 + 3c_{j-\frac{1}{2}} + (c_{j-\frac{1}{2}})^2 + 6s_{j-\frac{1}{2}}\right) p_{j-1}^n \quad (4.20)$$

$$\left(8 - 3(c_{j+\frac{1}{2}} - c_{j-\frac{1}{2}}) - (c_{j+\frac{1}{2}})^2 - (c_{j-\frac{1}{2}})^2 - 6s_{j+\frac{1}{2}} - 6s_{j-\frac{1}{2}}\right) p_j^n.$$

Just like for the lower order method, the negative ion solution is computed by changing the sign of the ion mobility from positive to negative rather than rederiving equations 4.13-4.20 for the negative ion system. The ion density for the higher order solution looks very similar to that of the lower order solution as is shown in figure 4.3. The two methods will be compared later.

The higher order flux is given by

$$\begin{aligned} \phi_{j+\frac{1}{2}}^H = & \frac{\Delta x}{12} \left[\left(2 + (c_{j+\frac{1}{2}})^2 \right) (\bar{p}_{j+1} - \bar{p}_j - p_{j+1}^n + p_j^n) + 3c_{j+\frac{1}{2}} (\bar{p}_{j+1} + \bar{p}_j + p_{j+1}^n + p_j^n) \right. \\ & \left. - 6s_{j+\frac{1}{2}} (\bar{p}_{j+1} - \bar{p}_j + p_{j+1}^n - p_j^n) \right] \end{aligned} \quad (4.21)$$

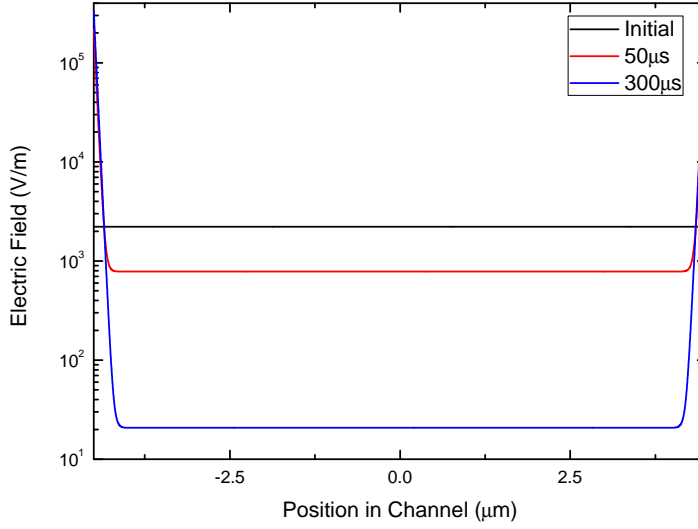
and can be seen in figure 4.4 which again shows similar behavior to the lower order solution and qualitatively makes sense.

4.2.5 Electric Field and Potential

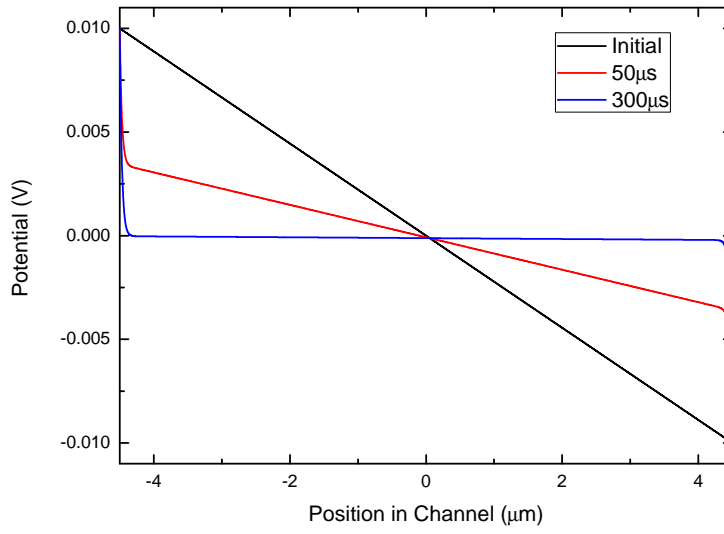
Assuming an initial known electric field and assuming it is constant over some small time step, the redistribution of the positive and negative ion densities can be calculated for either the higher or lower order methods. However, once the new ion densities are known, the electric field must be updated by solving Poisson's equation (equation 1.3). The 4th order Runge Kutta method[20] was chosen for this simulation to calculate the updated electric field for each time step. Using the fact that $E = -\frac{\partial V}{\partial x}$, equation 1.3 can be rewritten as

$$\frac{\partial E}{\partial x} = \frac{e}{\epsilon_w \epsilon_0} (Z_p p - Z_n n) \quad (4.22)$$

which is in the correct form for the Runge Kutta method. However, since Runge Kutta is a marching scheme, and a solution for initial value problems, this poses some difficulties. The electric field has neither an initial value, nor known boundary values (since the largest changes in the electric field happen precisely at the boundaries[6]). However, the potential has two known boundary values (one at each electrode). The Shooting Method[21] is a way to solve initial value problems in the form of boundary value problems. In this case, this is done by guessing an initial value for the electric field at the left boundary, which is enough information to complete the electric field



(a)



(b)

Figure 4.5: (a) Shows the evolution of the electric field as the positive and negative ions redistribute, like in figures 4.1 and 4.3. As can be seen the electric field changes sharply where the ions are accumulating, effectively screening the electric field applied between the electrodes. (b) Shows how the potential evolves as the ion densities change, again showing the largest change near the electrodes. In equilibrium all of the potential drops across the electrical double layer. The channel width is $9\mu\text{m}$ and the concentration of the solution is $0.0001\text{mol}/L$. At this concentration the cell is 296 Debye lengths and 5921 grid points are used with $\Delta x = 1.5\text{nm}$ and an adaptive scheme is employed to calculate Δt .

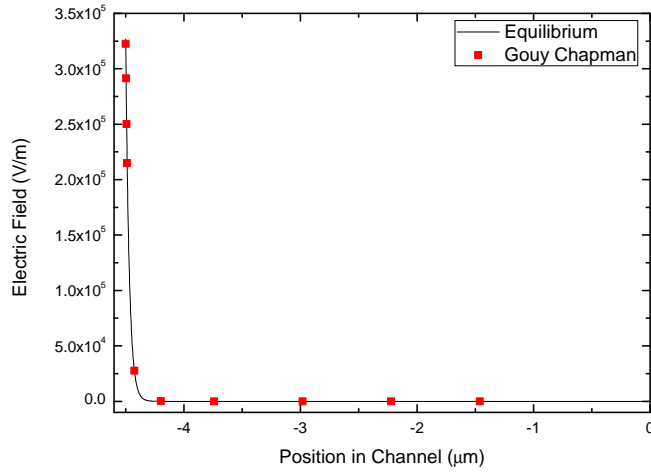
calculation. Then, the electric field can be used to determine the potential. The potential is calculated using a Simpson's[22] integration scheme with linear interpolation.

$$V_{j+1} = V_j - \frac{\Delta x}{2} (E_{j+1} + E_j). \quad (4.23)$$

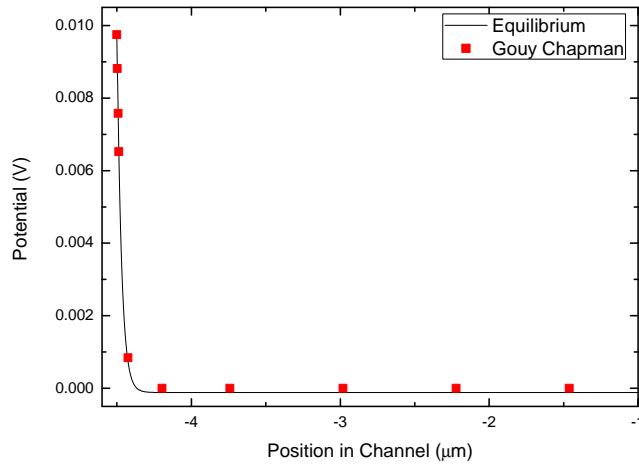
This requires the use of the left boundary condition on the potential to start the calculation, as the Simpson's integration scheme is also a marching scheme. Once the potential has been determined, the calculated value at the right boundary can be compared to the boundary condition. If it is within some tolerance the calculation will stop, but if it is not, a new guess for the initial electric field point is chosen and the calculation proceeds. The key with the shooting method is to make smart initial guesses for the electric field. This can be done by initially calculating both the electric field and potential with two initial guesses, q_0 and q_1 , and defining the difference between the two right boundary values as $d = f_1 - f_0$ where f_1 is the value of the right boundary calculated with initial guess q_1 and f_0 is the value of the right boundary calculated with initial guess q_0 . Although the choice of the first two initial guesses should be made reasonably carefully, the important thing is to choose any further required guesses in a clever manner. This can be done by defining the next initial guess as

$$q_2 = q_1 + (B - f_1) \frac{(q_1 - q_0)}{(f_1 - f_0)}. \quad (4.24)$$

Next $q_0 = q_1$ and $q_1 = q_2$ and the same procedure is repeated, calculating the electric field and potential for both guesses. The calculation stops when $d < tolerance$ which can be changed depending on the accuracy of the solution required. The Shooting method generally converges within a few iterations, at least for these systems.



(a)



(b)

Figure 4.6: (a) Shows the agreement of the electric field once the system has reached equilibrium with the semi-infinite Gouy-Chapman solution (equation 1.7). (b) Shows the agreement of the potential of the system in equilibrium with the semi-infinite Gouy-Chapman solution (equation 1.4). Both show excellent agreement, but there is a slight error in the potential, which is because Simpson's method with a linear interpolation is only a second order method. The better agreement for the electric field is because the Runge Kutta method used is accurate to 4th order. The channel width is $9\mu m$ and the solution concentration is $0.0001 mol/L$. At this concentration the cell is 296 Debye lengths and 5921 grid points are used with $\Delta x = 1.5 nm$ and an adaptive scheme is employed to calculate Δt .

Using the current solver for the tridiagonal system, the Courant number ($c_{j+\frac{1}{2}} = \frac{\mu_p \Delta t}{2\Delta x} (E_{i+1} + E_i)$) needs to be less than one ($c_{j+\frac{1}{2}} < 1$) everywhere, which is a necessary condition for convergence of the simulation. And since the Courant number depends on the electric field, as the electric field grows at the electrodes, Δt needs to be modified at each time step. This is simply done by finding the maximum value of the ($E_{j+\frac{1}{2}}$) term and using that to calculate Δt , where

$$\Delta t = \frac{0.9\Delta x}{\mu_p E_{j+\frac{1}{2}}} \quad (4.25)$$

and the minimum Δt is used after it is calculated for all $E_{j+\frac{1}{2}}$. The factor of 0.9 is used as the value of the Courant number, as a number close to, but less than 1. Its choice was somewhat arbitrary. This works very well for keeping the simulation going, but as the electric field nears equilibrium this makes Δt very small and takes many more time steps for the simulation to reach equilibrium. The behavior of the electric field as the calculation proceeds can be seen in figure 4.5a starting at a constant value and increasing rapidly at the boundaries and decreasing towards zero in the middle. Figure 4.5b shows the evolution of the potential when the the two electrodes are held at V_0 and $-V_0$ where the potential profile starts as a linear decrease from V_0 to $-V_0$ and finishes moving sharply from the left boundary at V_0 to zero and then decreasing sharply from zero to $-V_0$ at the opposite boundary. Both the potential and the electric field show the effects of screening that the accumulation of ions at the boundaries produces.

Now that the evolution of the electric field and potential have been seen to behave qualitatively as expected, they can be compared to the Gouy-Chapman solutions discussed in the introduction. To decide when to stop the simulation, some criterion is needed. Since the simulation asymptotically approaches the solution, it needs to be cut off at some point which is effectively the equilibrium.

To do this, the simulation was run for a long time, and the maximum value of the flux at a time step where the ion densities don't change noticeably. This value of the flux was found to be approximately $10^5 \text{ ions}/m^2s$, so the simulation was run until the flux in the middle of the channel was greater than $5 * 10^4 \text{ ions}/m^2s$. Figure 4.6a compares the calculated electric field after the cut off to the Gouy-Chapman solution, showing excellent agreement. The agreement for the potential is not quite as good, as can be seen in figure 4.6b and this is because the potential is calculated only using a first order method. Using a higher order integration scheme could improve this, but it would make dealing with the boundary conditions for the shooting method more difficult. Since the potential was only used for its boundary conditions and the electric field agreed with the Gouy-Chapman solution well, it was determined to be unnecessary.

4.2.6 Flux Corrected Transport Algorithm

Now that two algorithms have been introduced, which both have different strengths, the Flux Corrected Transport algorithm can be introduced to combine the two algorithms into a more accurate solution. The lower and higher order fluxes, defined by equations 4.4 and 4.21 can be combined to define the anti-diffusive flux,

$$\phi_{j+\frac{1}{2}}^A = \phi_{j+\frac{1}{2}}^H - \phi_{j+\frac{1}{2}}^L \quad (4.26)$$

which allows the higher order solution to be transformed into the lower order solution.

$$\bar{p}_j = \tilde{p}_j - \frac{1}{\Delta x}(\phi_{j+\frac{1}{2}}^A - \phi_{j-\frac{1}{2}}^A). \quad (4.27)$$

At this point nothing has been gained. The lower order solution still has numerical diffusion, and the higher order solution can still suffer from oscillations

caused from over-shooting sharp features. The strength of the FCT algorithm is the application of a flux limiter. This flux limiter modifies the anti-diffusive flux to eliminate any oscillations that are present in the higher order solution, but also to use the higher order solution as much as possible to achieve less numerical diffusion. There exists more than one flux limiting scheme, but in this thesis a limiter defined by Zalesak[17] will be used. The correction of the flux was achieved with a simple multiplier

$$\phi_{j+\frac{1}{2}}^C = C_{j+\frac{1}{2}} \phi_{j+\frac{1}{2}}^A, \quad 0 \leq C_{j+\frac{1}{2}} \leq 1 \quad (4.28)$$

where $C_{j+\frac{1}{2}}$ is the correction multiplier. The algorithm devised to apply the limiter is fairly straightforward. First a condition is set on the anti-diffusive flux.

$$\begin{aligned} \phi_{j+\frac{1}{2}}^A = 0 \quad & \text{if} \quad \phi_{j+\frac{1}{2}}^A (\tilde{p}_{j+1} - \tilde{p}_j) < 0 \\ \text{and either} \quad & \phi_{j+\frac{1}{2}}^A (\tilde{p}_{j+2} - \tilde{p}_{j+1}) < 0 \\ \text{or} \quad & \phi_{j+\frac{1}{2}}^A (\tilde{p}_j - \tilde{p}_{j-1}) < 0 \end{aligned} \quad (4.29)$$

After these conditions have been applied to the anti diffusive flux, p_j^{max} and p_j^{min} will be defined as

$$p_j^{max} = \max(p_{j-1}^n, p_j^n, p_{j+1}^n, \tilde{p}_{j-1}, \tilde{p}_j, \tilde{p}_{j+1}) \quad (4.30)$$

$$p_j^{min} = \min(p_{j-1}^n, p_j^n, p_{j+1}^n, \tilde{p}_{j-1}, \tilde{p}_j, \tilde{p}_{j+1}) \quad (4.31)$$

then, using p_j^{max} and p_j^{min} as well as the anti-diffusive flux

$$P_j^+ = \max(0, \phi_{j-\frac{1}{2}}) - \min(0, \phi_{j+\frac{1}{2}}) \quad (4.32)$$

$$Q_j^+ = (p_j^{max} - \tilde{p}_j)\Delta x \quad (4.33)$$

$$R_j^+ = \begin{cases} \min\left(1, \frac{Q_j^+}{P_j^+}\right) & P_j^+ > 0 \\ 0 & P_j^+ = 0 \end{cases} \quad (4.34)$$

$$P_j^- = \max(0, \phi_{j+\frac{1}{2}}) - \min(0, \phi_{j-\frac{1}{2}}^A) \quad (4.35)$$

$$Q_j^- = (\tilde{p}_j - p_j^{min})\Delta x \quad (4.36)$$

$$R_j^- = \begin{cases} \min\left(1, \frac{Q_j^-}{P_j^-}\right) & P_j^- > 0 \\ 0 & P_j^- = 0 \end{cases} \quad (4.37)$$

where P_j^+ and P_j^- are the sums of the anti-diffusive fluxes into mesh point j and out of mesh point j respectively. R_j^+ represents the smallest upper bound of the fraction which corrects the antidiffusive flux to ensure that there is no overshoot of the ion density at mesh point j . Similarly R_j^- is the smallest upper bound for the anti-diffusive flux correction which ensures no under-shoot at mesh point j . [17] Since if the anti-diffusive flux is directed away from one mesh point it will be directed towards an adjacent mesh point, the flux limiting will take place with respect to undershoots for antidiffusive flux directed away from a mesh point, and will take place with respect to overshoots for antidiffusive flux directed towards a mesh point. To ensure that the correction is applied

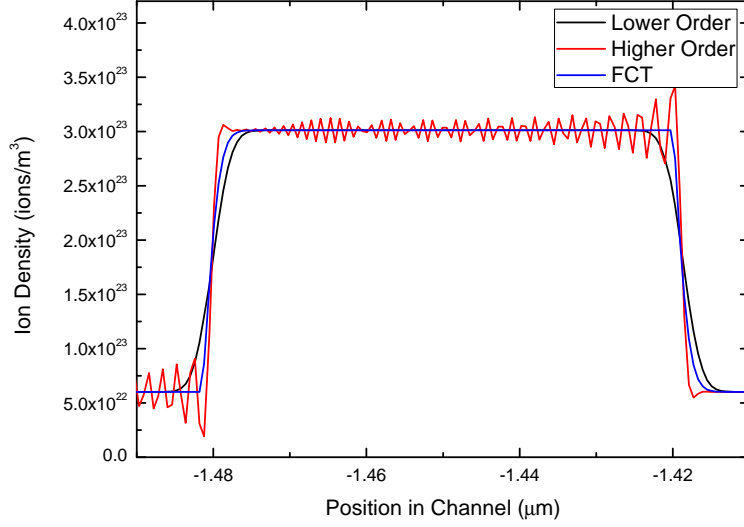


Figure 4.7: FCT, Higher and Lower Order algorithms applied to an input density pulse, which is 5 times the concentration elsewhere in the channel, propagated forward for 1000 time steps. The FCT solution is free from the oscillations that are prevalent in the higher order solution, as well as being much sharper than the lower order solution, illustrating that it is a superior solution to both methods. For this test the electric field is held constant and not recalculated each time step and the diffusion constant is made extremely small to allow the pulse to hold its shape for over 1000 time steps. For this simulation there are 14803 grid points and $\Delta x = 0.6nm$ in the $9\mu m$ channel and a constant $\Delta t = 1ns$.

properly

$$C_{j+\frac{1}{2}} = \begin{cases} \min(R_{j+1}^+, R_j^-) & \phi_{j+\frac{1}{2}}^A \geq 0 \\ \min(R_j^+, R_{j+1}^-) & \phi_{j+\frac{1}{2}}^A < 0 \end{cases}. \quad (4.38)$$

Then after correcting the flux, with equation 4.28 the flux corrected ion density can be found with

$$p_j = \tilde{p}_j - \frac{1}{\Delta x}(\phi_{j+\frac{1}{2}}^C - \phi_{j-\frac{1}{2}}^C). \quad (4.39)$$

The FCT procedure will produce a more accurate solution for the ion density than both the lower and higher order algorithms alone. The same procedure was followed to determine the flux corrected negative ion density solutions.

Figure 4.7 compares all three methods with the propagation of an initial ion density pulse in a constant electric field. The electric field calculations described in Section 4.2.5 were turned off and the diffusion constant was changed to a very small value so that the ion density pulse wouldn't smooth out appreciably over the 1000 time steps of the calculation. The lower order solution maintains its shape fairly well, with a lot of smoothing. The higher order method picks up the sharp change at the edges of the ion density pulse very well, however suffers from extreme over-shoots and undershoots and the density oscillations take a long time to decay. However, the FCT solution is a significant improvement over both other methods. The FCT algorithm smooths out the under-shoots and over-shoots very nicely, as well as maintaining sharper edges in the ion density pulse compared to the lower order method. Figure 4.7 shows that the FCT algorithm is a significantly better algorithm and confirms that more accurate results will be achieved by using this algorithm to simulate the electrical double layer formation.

4.2.7 Realistic Voltage Pulse

Up into this point the simulation has been basically the same as the simulation done by Morrow et al.[6] except for using a uniform mesh, rather than a logarithmically varying mesh, which is simpler to program, although costly for computation time. However, there are several modifications to make so that the simulation matches the specific parameters of the experiment. In the simulation done by Morrow et al. they define the potential in such a way that it has a finite rise time, to be a more realistic pulse. The first attempt to make a realistic voltage pulse was to record the applied pulse from the SRS function generator and use that as a realistic voltage pulse. Figure 4.8 shows a sample real pulse as well as a cubic spline interpolation so that any value of the pulse

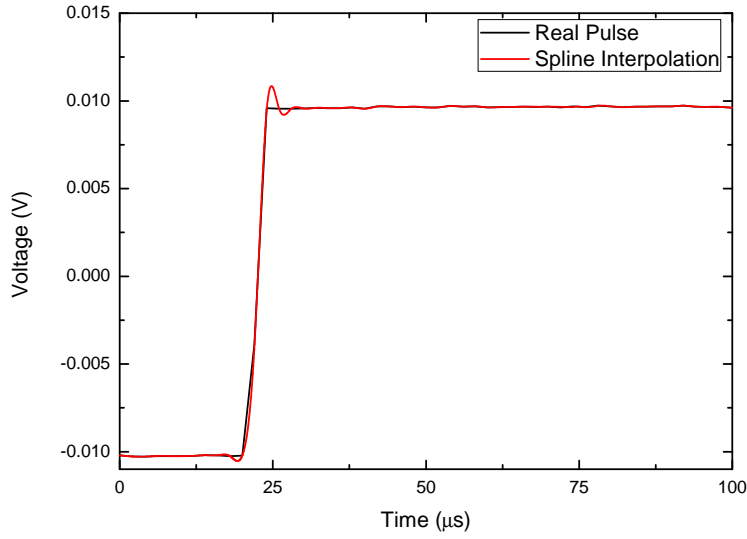


Figure 4.8: Shows the real pulse created from the function generator compared with the cubic spline interpolation. The interpolation uses 2000 points from the file recorded from the function generator on the oscilloscope. The agreement is quite good, with some slight undershoot and overshoot at the sharp change in the pulse.

can be found. Using this pulse allowed some of the fluctuations that appeared in the real input pulse to be present in the simulated response. However, although the pulse is applied to one side of the channel quickly from the function generator, the potential drop across the cell, which is the important parameter, is limited by the RC time of the total circuit. This means the voltage drop is applied slower than if it came only from the function generator. The applied voltage can then be given by $V_{RC} = V_0(1 - e^{-\frac{t}{RC_{eq}}})$. Simulations were run using both types of input pulses, and it was found that the double layer time constant was long enough that the pulse shape made very little difference to the current generated from the ion flow.

In the Morrow simulation the input voltage pulse starts at $V = 0$ and after the rise time is $V = V_0$, however the function generator doesn't actually generate a voltage pulse, but a square wave which is centered at $V = 0$, and has

a minimum value of $V = -V_0$ and a maximum value of $V = V_0$. This means physically, that the initial ion density distributions are not at equilibrium with $V = 0$ (and constant throughout the channel). If the pulse is positive, it means that the initial ion density distribution is that of the system having reached equilibrium with $V = -V_0$ (a double layer has formed with $V = -V_0$). To have this initially formed double layer requires the program to be modified to read in a file with an initial positive and negative ion distributions and to have previously run the program with the parameters of interest (channel width, number of mesh points, concentration, maximum magnitude of the voltage pulse) with the signs on the voltage boundary conditions reversed. Since just the final ion density distributions are required from this calculation, it can be run with a perfect voltage pulse (*rise time* = 0) to simplify everything.

4.2.8 Current

The ultimate goal of this simulation is to calculate the current in the circuit, which can be compared to the measured current from the experiment. The starting current equation used is the modified Sato equation[23] which Morrow used in his original double layer simulation. The equation is

$$I = \frac{A}{d} e \int_0^d \left[pW_p - nW_n + D_p \frac{\partial p}{\partial x} - D_n \frac{\partial n}{\partial x} \right] dx + C \frac{dV}{dt} \quad (4.40)$$

where $W_p = \mu_p E$ and $W_n = \mu_n E$ are the ion velocities. The integral term is an average of the non-Faradiac current at each grid point over the entire cell generated from the flow of the ions, and the term with the time derivative of the potential is the displacement current.[6] The ion drift terms (pW_p and nW_n) are calculated at each grid point. Through the bulk of the cell the diffusion derivatives are calculated with a centered difference formula ($\frac{\partial p}{\partial x} = \frac{(p_{j+1} - p_{j-1})}{2\Delta x}$)

which has the diffusion centered at the grid point j . However, at the boundaries this centered difference formula can't be used, and a forward or backwards difference equation must be used, which has the diffusion centered between the two grid points. This means that the current calculated for the grid point at the boundary is less accurate than the current calculated elsewhere, but the accuracy can be improved by increasing the number of grid points. Figure 4.9 shows the spatial dependence of the current. The current is consistent everywhere in the channel except at the boundaries. At the boundaries not only the magnitude of the current is different, but it is no longer an exponential decay as well. Figure 4.10 shows the current calculated at the left boundary of the channel as the number of grid points is varied. As the number of grid points is increased the steady state current at the boundary decreases towards a constant, non-zero value. This shows that at the boundary, where the gradient of the ion densities is largest, there are significant numerical errors. However, these errors don't extend far from the boundary, so the effect on the current from the Morrow-Sato equation is small and doesn't effect the time constants that are determined from it.

The average current from equation 4.40 gives good qualitative agreement with the measured current, with both following an exponential decay, but is dominated by the non-Faradic current. The external circuit current term in equation 4.40 is dependent on the choice of input pulse. Using $V_{RC} = V_0(1 - e^{-\frac{t}{RC_{eq}}})$ ensures that the current calculated for the external circuit is accurate. If the currents from the two terms were of similar magnitudes, the choice of which voltage to use would be very important, however it turned out that it was insignificant in the simulation. The simulation also found that the double layer time constant was much larger than the RC time constant of the circuit.

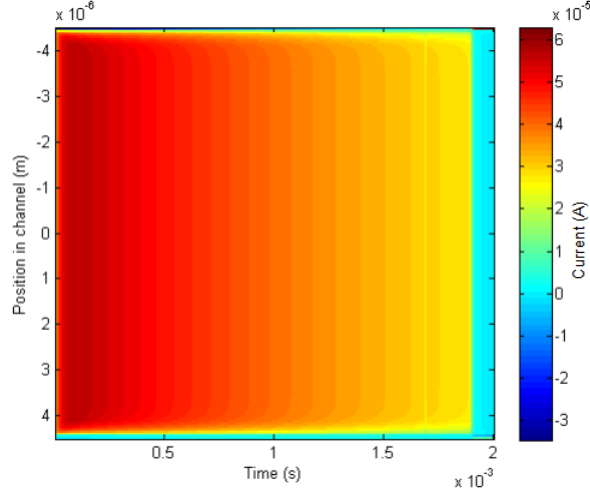


Figure 4.9: Shows the spatial distribution of the current in the microchannel as a function of time. Through the majority of the channel the current is constant, but near the boundaries the current changes in both magnitude and shape of the current. This simulation was run at $p_0 = 1 * 10^{-5} mol/L$ with 1872 grid points and $\Delta x = 4.8nm$. The simulation ran with a constant time step $\Delta t = 5ns$ until the initial double layer was driven through the uniform density. Then the simulation switched to the adaptive algorithm for setting Δt .

4.2.9 Parylene Model

Another addition to the simulation is to include the voltage drop across the parylene layers, which decreases the strength of the initial voltage pulse. This was done using a 3 level dielectric model with the two parylene layers ($\epsilon_{parylene} = 2.65$) and the channel filled with water ($\epsilon_{water} = 80$). Figure 4.12 shows a schematic of this dielectric model. The electric field in any layer is given by $E_i = \frac{\sigma}{\epsilon_0 \epsilon_i}$, where σ is the surface charge and ϵ_i is the dielectric constant of the i th layer. The potential drop across any layer is given by the electric field in the layer multiplied by its thickness, and the total potential is the sum of each of the potential drops:

$$V = E_1 a + E_w b + E_2 c. \quad (4.41)$$

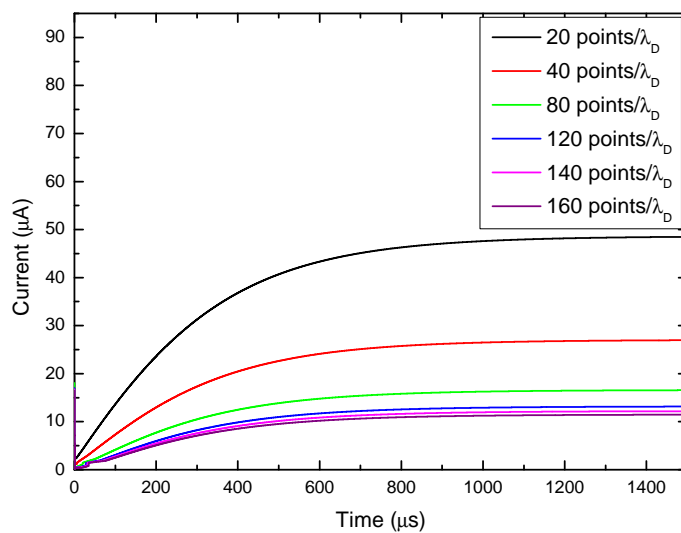


Figure 4.10: Shows the current calculated at the first grid point varying the number of grid points from 20-160 points per Debye length (1872-14979 total grid points). As the grid gets finer the current approaches a stable value where it becomes independent of the number of grid points, showing that the numerical error is large at the boundaries where the gradients of the ion densities change the most significantly. The simulation was run for $p_0 = 1 * 10^{-5} mol/L$ with a $9\mu m$ channel depth which gives 93.6 Debye lengths in the length of the channel and a constant $\Delta t = 10ns$ was used for all of the simulations and $\Delta x = 4.8nm - 0.6nm$ from the least number of grid points to the most.

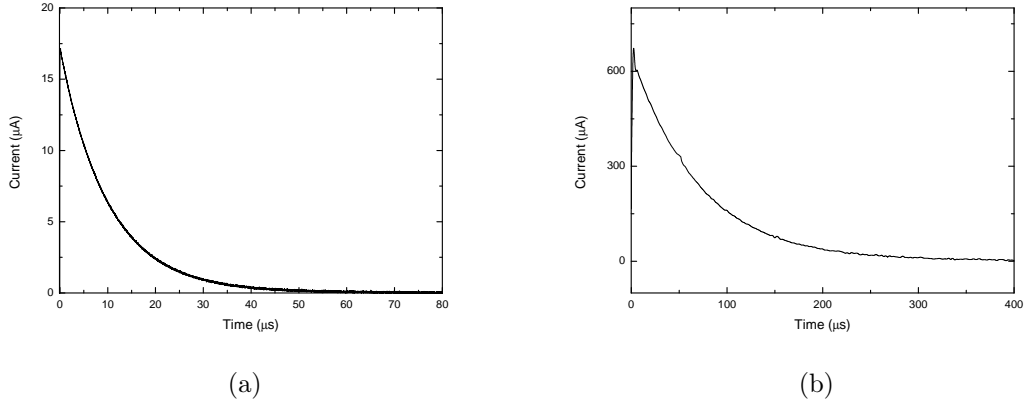


Figure 4.11: (a) shows sample measured current from the experiment, showing a slightly noisy exponential decay which is more evident in figure 4.13b. This signal is taken with a sample with a top plate thickness of 93.8nm and a concentration of 0.0001mol/L taken with the variable load resistance set at $1\text{k}\Omega$. (b) shows the current calculated in the FCT simulation with $9\mu\text{m}$ channel depth and 0.0001mol/L which has 5921 grid points ($\Delta x = 1.5\text{nm}$) and used the adaptive algorithm to adjust Δt each time step. The simulated spatially averaged current in (b) has some of the same qualitative features as the measured current, although the time scales are significantly different and the relative scales of the current are different, with the simulated current from the double layer being larger.

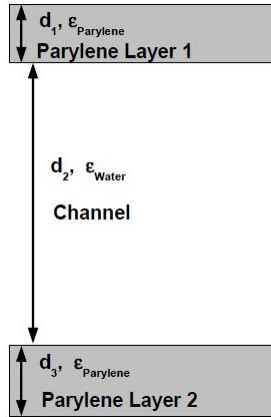


Figure 4.12: Shows a schematic of the three layer dielectric model. This consists of two layers of parylene, of thicknesses d_1 and d_3 , separated by a channel filled with water, of thickness d_2 . This model doesn't take into consideration the formation of the electrical double layer.

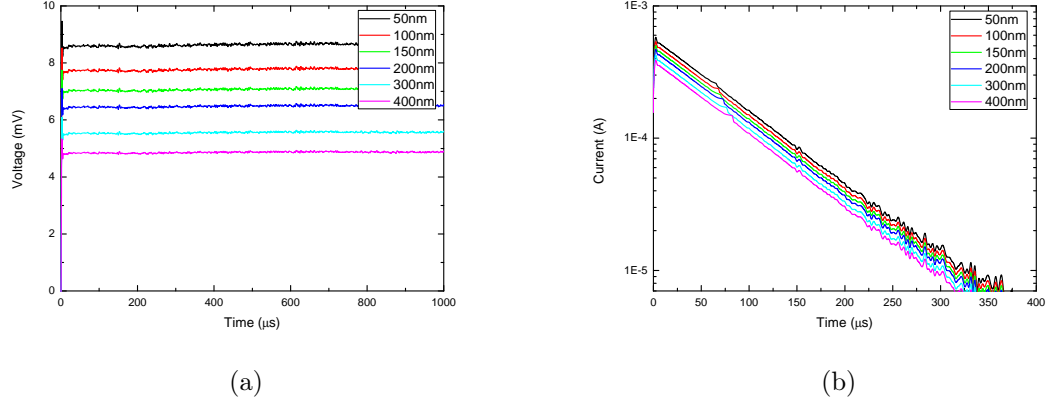


Figure 4.13: (a) The parylene model for different thicknesses of the parylene layer on the top plate applied to a 10mV input pulse. As the thickness of the parylene increases, the magnitude of the pulse decreases. (b) The current calculated using the modified input pulses from (a) for a channel thickness of $9\mu m$ and a concentration of $0.0001mol/L$. At this concentration the cell is 296 Debye lengths and 5921 grid points were used with $\Delta x = 1.5nm$ and an adaptive scheme was employed to calculate Δt .

Substituting the expression for the electric field into equation 4.41 and solving for the surface charge gives

$$\sigma = \frac{V_0 \epsilon_{parylene} \epsilon_{water} \epsilon_0}{\epsilon_{water} (a + c) + b \epsilon_{parylene}}. \quad (4.42)$$

Equation 4.42 can be substituted into $\Delta V_i = \frac{\sigma d_i}{\epsilon_i \epsilon_0}$ to give the potential drop of the i th layer. Assuming that the potential drop across the parylene layer is independent of the ion behavior in the channel, equation 4.42 can be applied to the voltage pulse to get a reduction in the magnitude of the voltage pulse.

The potential drop through the parylene layer for various thicknesses of parylene is shown in figure 4.13a using the pulse from the function generator. As the thickness of the parylene increases, the potential drop across the parylene layer increases (meaning a decrease in the potential across the channel), but the pulse maintains the same basic shape. Figure 4.13b shows the current calculated for the various input pulses with a concentration of $0.0001mol/L$

and a channel thickness of $9\mu m$. As the thickness of the parylene layer increases and the magnitude of the input pulse decreases, the maximum current also decreases. The time constant appears to remain constant over this range of potential, however this will be investigated over a larger potential range later.

4.3 Simulation Parameters

In this simulation the diffusion constants used are $D_{Cl} = 1.77 * 10^{-9} m^2/s$ and $D_K = 1.83 * 10^{-9} m^2/s$ for Cl^- and K^+ respectively and their ion mobilities are $\mu_{Cl} = 6.88 * 10^{-8} m^2/Vs$ and $\mu_K = 7.12 * 10^{-8} m^2/Vs$ [24]. The concentration of the KCl solution was varied from $1 * 10^{-6} mol/L$ to $0.1 mol/L$. As the concentration of the solution increases, so does the number of grid points. The number of points varied with the Debye length of the solution, and for each Debye length there were 20 grid points. As the number of grid points increased, the number of calculations per time step increased by the same factor, and the number of time steps also approximately doubled, based on the fact that Δt , from equation 4.25, is proportional to the spacing, Δx . The run time for the simulations varied from approximately one minute for the smallest concentrations, to days for the highest concentration on a Intel Core 2 Duo 2.1 GHz cpu with 4GB of ram.

4.4 Results

Since the external circuit current was so small compared with the current from the ion flow, direct comparison of the currents in the experiment and simulation might not be possible, so comparison with the experiment needs to be made in a different manner. For this, the calculated current, using equation

4.40 will be used. Figure 4.14 shows how the time constant for the double layer formation time decreases as the concentration increases. It also shows that the magnitude of the current increases significantly as the concentration increases. This makes sense as the current depends mostly on the ion flux, which increases as the concentration, and thus, total number of ions, increases. Figure 4.15 shows the relationship between the concentration and the time constant. It also shows a power law fit, with $\tau = 0.8402p_0^{-0.4932}\mu s$, compared to the data from the simulations. This power law is similar in form to equation 4.1 for the Debye length. The exponents are almost exactly the same suggesting that the electrical double layer formation time is proportional to the Debye length. A similar conclusion was found in the simulation work of Morrow et al.[6]. The different coefficient between the the power law equation found by Morrow et al, and found here is most likely a result of starting this simulation with a fully formed double layer for a negatively valued voltage pulse and the use of a real voltage pulse, rather than a finite rise time, analytic approximation for a voltage pulse.

Lastly for $p_0 = 1 * 10^{-4}mol/L$ the magnitude of the input pulse was varied from 5mV-40mV to see how the time constant of the double layer formation varies with voltage. Figure 4.16a shows how the current varies with a constant concentration as the magnitude of the input pulse varies. The maximum current increases as the strength of the input pulse increases. Because of the higher initial current, the larger input pulse requires a longer time to decline to the same value, as can be seen by the increased value of the x-intercept for a higher input pulse value. However, since the slopes look similar further analysis needs to be done to determine the time constant. The time constant was found the same way as before, and the results can be seen in figure 4.16b. As the magnitude of the input pulse was increased the time constant can be

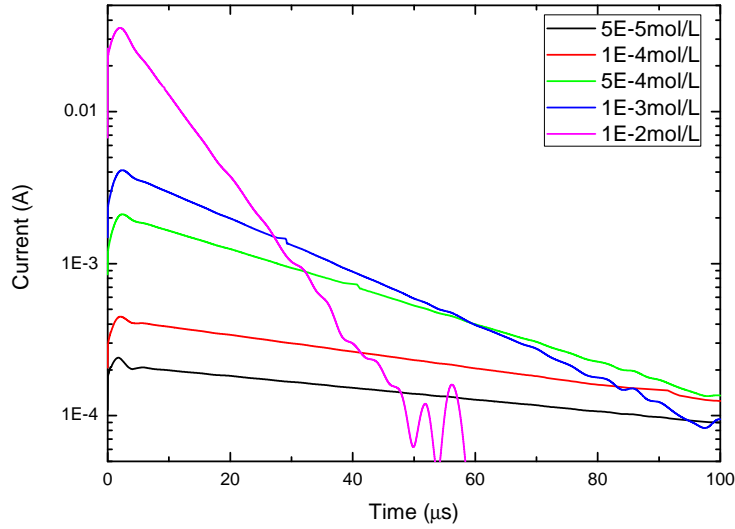


Figure 4.14: The decay of the simulated current calculated using equation 4.40 for concentrations ranging from $5 \times 10^{-5} \text{ mol/L}$ to $1 \times 10^{-2} \text{ mol/L}$. From these concentrations the number of grid points varies from 4187 to 59211 which corresponds to $\Delta x = 2.15 \text{ nm}$ to $\Delta x = 0.15 \text{ nm}$ and uses the adaptive algorithm to change Δt .

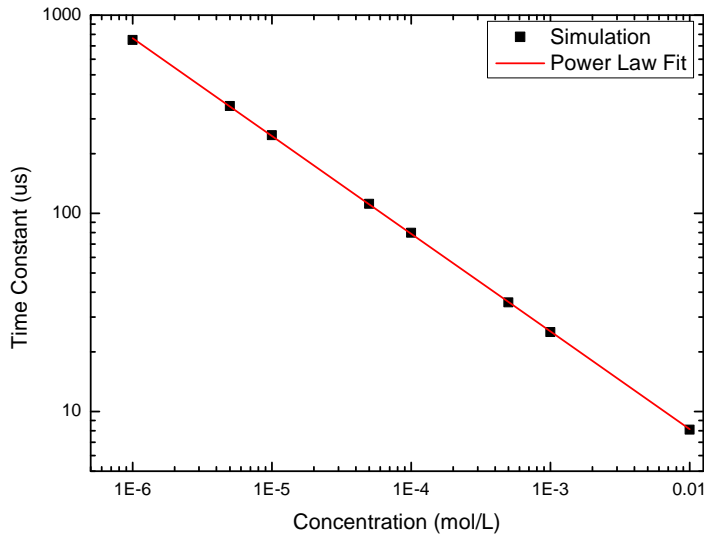


Figure 4.15: Shows the time constants calculated from the simulated currents for the different concentrations shown in figure 4.14. The red curve is a power law fit giving the equation $\tau = 0.8402p_0^{-0.4932} \mu s$.

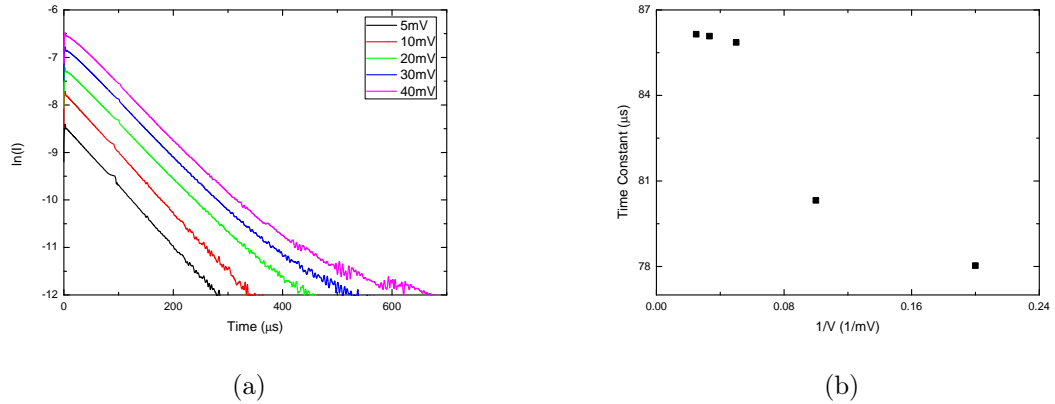


Figure 4.16: (a) shows the natural logarithm of the current plotted against time for input pulse magnitudes of 5mV-40mV. (b) shows the value of the time constant plotted against the input pulse magnitude. The channel thickness used was $9\mu m$ and the concentration was $0.0001 mol/L$. All of the simulations used 5922 grid points and a spacing $\Delta x = 1.5nm$ and the adaptive algorithm for the time step, Δt . The input pulses were all generated from the function generator.

seen to increase, but not in a linear fashion, and appears to be approaching some maximum value.

4.5 Future Work

The majority of the change inside the microfluidic cell happens within a few λ_D of each boundary. This simulation is inefficient in the sense that it has a constant grid spacing. This means that to increase the accuracy at the boundaries a very large number of points needs to be added to the simulation which causes long run times for the simulation. The next step would be to make this simulation much more efficient by using a variable mesh which had very small spacing between grid points near the boundaries and a larger spacing near the middle of the cell where very little change is occurring in the ion densities. Morrow used a logarithmically varying mesh[6]. However, to use a variable mesh the higher order and lower order equations need to be modified

for this. Equation 4.3 for the lower order ion density becomes

$$\begin{aligned}
& -2\Delta x_{j-\frac{1}{2}}s_{j-\frac{1}{2}}\tilde{p}_{j-1} + \left(2\Delta x_j + 2\Delta x_{j+\frac{1}{2}}s_{j+\frac{1}{2}} + 2\Delta x_{j-\frac{1}{2}}s_{j-\frac{1}{2}}\right)\tilde{p}_j \\
& -2\Delta x_{j+\frac{1}{2}}s_{j+\frac{1}{2}}\tilde{p}_{j+1} = \Delta x_{j-\frac{1}{2}}(c_{j-\frac{1}{2}} + |c_{j-\frac{1}{2}}|)p_{j-1}^n \\
& + \left(2\Delta x_j - \Delta x_{j+\frac{1}{2}}(c_{j+\frac{1}{2}} + |c_{j+\frac{1}{2}}|) + \Delta x_{j-\frac{1}{2}}(c_{j-\frac{1}{2}} - |c_{j-\frac{1}{2}}|)\right)p_j^n \quad (4.43) \\
& -\Delta x_{j+\frac{1}{2}}(c_{j+\frac{1}{2}} - |c_{j+\frac{1}{2}}|)p_{j+1}^n
\end{aligned}$$

and the lower order ion flux becomes

$$\phi_{j+\frac{1}{2}}^L = \frac{\Delta x_{j+\frac{1}{2}}}{2} \left[(c_{j+\frac{1}{2}} + |c_{j+\frac{1}{2}}|)p_j^n + (c_{j+\frac{1}{2}} - |c_{j+\frac{1}{2}}|)p_{j+1}^n - 2s_{j+\frac{1}{2}}(\tilde{p}_{j+1} - \tilde{p}_j) \right] \quad (4.44)$$

where $\Delta x_{j+\frac{1}{2}} = x_{j+1} - x_j$ and $\Delta x_j = (\Delta x_{j+\frac{1}{2}} + \Delta x_{j-\frac{1}{2}})/2$. The Courant number becomes $c_{j+\frac{1}{2}} = \frac{U_{j+\frac{1}{2}}\Delta t}{\Delta x_{j+\frac{1}{2}}}$, where $U_{j+\frac{1}{2}} = \mu(E_{j+1} + E_j)/2$ is the ion drift velocity and the diffusion constant is given by $s_{j+\frac{1}{2}} = \frac{D_{j+\frac{1}{2}}\Delta t}{(\Delta x_{j+\frac{1}{2}})^2}$ where the diffusion coefficient is given by $D_{j+\frac{1}{2}} = (D_{j+1} + D_j)/2$. The higher order ion density and flux equations can be modified similarly to give

$$\begin{aligned}
& \left(-3\Delta x_{j-\frac{1}{2}}c_{j-\frac{1}{2}} + \Delta x_{j-\frac{1}{2}} \left[2 + (c_{j-\frac{1}{2}})^2 - 6s_{j-\frac{1}{2}}\right]\right)\bar{p}_{j-1} + \left(12\Delta x_j + 3\Delta x_{j+\frac{1}{2}}c_{j+\frac{1}{2}}\right. \\
& \left.- 3\Delta x_{j-\frac{1}{2}}c_{j-\frac{1}{2}} - \Delta x_{j+\frac{1}{2}} \left[2 + (c_{j+\frac{1}{2}})^2 - 6s_{j+\frac{1}{2}}\right] - \Delta x_{j-\frac{1}{2}} \left[2 + (c_{j-\frac{1}{2}})^2 - 6s_{j-\frac{1}{2}}\right]\right)\bar{p}_j \\
& + \left(3\Delta x_{j+\frac{1}{2}}c_{j+\frac{1}{2}} + \Delta x_{j+\frac{1}{2}} \left[2 + (c_{j+\frac{1}{2}})^2 - 6s_{j+\frac{1}{2}}\right]\right)\bar{p}_{j+1} = \left(-3\Delta x_{j-\frac{1}{2}}c_{j-\frac{1}{2}}\right. \\
& \left.+ \Delta x_{j-\frac{1}{2}} \left[2 + (c_{j-\frac{1}{2}})^2 + 6s_{j-\frac{1}{2}}\right]\right)p_{j-1}^n + \left(12\Delta x_j - 3\Delta x_{j+\frac{1}{2}}c_{j+\frac{1}{2}}\right. \\
& \left.+ 3\Delta x_{j-\frac{1}{2}}c_{j-\frac{1}{2}} - \Delta x_{j+\frac{1}{2}} \left[2 + (c_{j+\frac{1}{2}})^2 + 6s_{j+\frac{1}{2}}\right] - \Delta x_{j-\frac{1}{2}} \left[2 + (c_{j-\frac{1}{2}})^2 + 6s_{j-\frac{1}{2}}\right]\right)p_j^n \quad (4.45) \\
& + \left(-3\Delta x_{j+\frac{1}{2}}c_{j+\frac{1}{2}} + \Delta x_{j+\frac{1}{2}} \left[2 + (c_{j+\frac{1}{2}})^2 + 6s_{j+\frac{1}{2}}\right]\right)p_{j+1}^n
\end{aligned}$$

and

$$\phi_{j+\frac{1}{2}}^H = \frac{\Delta x_{j+\frac{1}{2}}}{12} \left[(2 + (c_{j+\frac{1}{2}})^2)(\bar{p}_{j+1} - \bar{p}_j - p_{j+1}^n + p_j^n) + 3c_{j+\frac{1}{2}}(\bar{p}_{j+1} + \bar{p}_j + p_{j+1}^n + p_j^n) - 6s_{j+\frac{1}{2}}(\bar{p}_{j+1} - \bar{p}_j + p_{j+1}^n - p_j^n) \right]. \quad (4.46)$$

Using equations 4.43-4.46 for the lower and higher order solutions, applying the boundary conditions in the same way, will increase the speed of calculations by not wasting many calculations in the middle of the solution where there is very little change, but also improving the overall accuracy of the solution by allowing for more grid points within the first few λ_D where the ion densities change the most over time.

Chapter 5

Electrical Double Layer

Experiment

5.1 Introduction

A lot is known about the properties of the electrical double layer in equilibrium. It is known how the electrical double layer changes the capacitance of the system[7] as well as many other or its chemical characteristics, however, there are few experimental studies of the dynamics of the electrical double layer formation. The capacitance of the double layer suggests electric detection of the double layer dynamics. Morrow and colleagues[25] performed an experiment that looks at the formation of the electrical double layer, however their experiment was on a much larger system, that was very different from the simulation described in Chapter 4. Their system involved a large length scale ($\sim 5\text{cm}$). They used a four point scheme where they applied a voltage pulse between a working electrode and a counter electrode and then measured the voltage drop in a region between the two outer electrodes to observe the voltage drop of the system. When observing the time dependence of this volt-

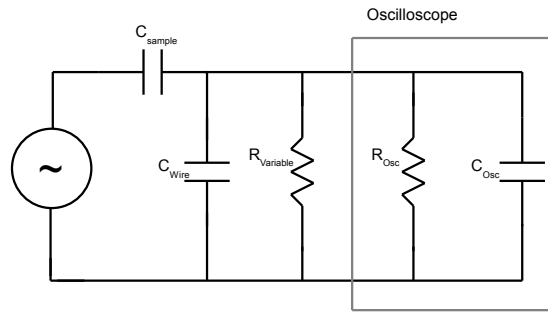
age drop they were able to reconstruct the voltage profile of the system and from an equivalent circuit model were able to determine the charging time of the circuit.

In this experiment a two probe detection scheme will be used. In a microfluidic system it would be very difficult to get two suspended electrodes between the outer electrodes to have a 4 point probe detection scheme. A voltage pulse was applied to one of the two electrodes, and the response of the system was measured at the other electrode. The circuit that describes the system with the capacitor structure connected to a function generator (SRS DS345) to apply a voltage pulse, and connected to an oscilloscope (Tektronix TDS 3052B) to detect the response can be seen in figure 5.1a. The equivalent circuit can be seen in figure 5.1b where R_1 is the resistance of the function generator, R_2 is the total resistance of the oscilloscope and variable load resistor in parallel, C_1 is the total capacitance of the sample and C_2 is the equivalent capacitance of the capacitive elements of the external circuit. The circuit was analyzed from point P1. The oscilloscope is terminated at $1M\Omega$ for the entire experiment. A second order differential equation to describe the system can be derived,

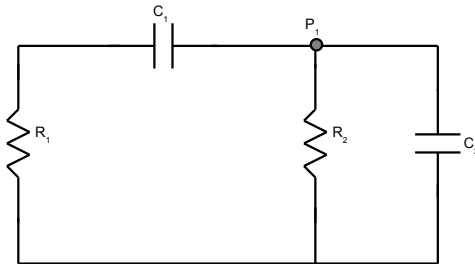
$$R_2 R_1 C_2 \frac{d^2 Q_1}{dt^2} + \left[R_2 \left(\frac{C_2}{C_1} + 1 \right) - R_1 \right] \frac{dQ_1}{dt} - \frac{Q_1}{C_1} = 0. \quad (5.1)$$

The solution to equation 5.1 isn't a simple exponential with an RC time constant, however the second order term will be much smaller than the first order term for any parameters of this experiment (by $\sim 10^9$) and be neglected. From this approximation, equation 5.1 becomes

$$\left[R_2 \left(\frac{C_2}{C_1} + 1 \right) - R_1 \right] \frac{dQ_1}{dt} - \frac{Q_1}{C_1} = 0 \quad (5.2)$$



(a)



(b)

Figure 5.1: (a) Schematic of the circuit used in the experiment, without the wire capacitance between the function generator and sample capacitor, C_1 , because that capacitance was found not to make a difference. The oscilloscope is enclosed in the box. (b) Schematic of the equivalent circuit during the discharging of a capacitor, where the function generator has been replaced by a resistor, R_1 , R_2 is the equivalent resistance of the variable resistor and terminating resistance of the oscilloscope. C_2 is the equivalent capacitance between the coaxial wire and the oscilloscope. The analysis of the circuit is done starting at the point, P_1

C_2 (pF)	$R_2 = 47619\Omega$		$R_2 = 4975\Omega$	
	τ_{Model}	$\tau_{Experiment}$	τ_{Model}	$\tau_{Experiment}$
210	14.76	15.93	1.54	1.61
310	19.52	20.07	2.03	2.08
620	34.28	33.68	3.58	3.21
760	41.42	40.42	4.32	3.89
1010	52.85	50.97	5.52	4.96
1070	59.99	58.71	6.26	5.83

Table 5.1: This table compares the model to the experiment while varying C_2

which has a solution

$$Q_1 = Ae^{\left(\frac{-t}{C_1[R_2(\frac{C_2}{C_1}+1)-R_1]}\right)}. \quad (5.3)$$

The solutions for equations 5.1 and 5.2 were compared and the deviation between the two is only at the nanosecond time scale. The denominator in the exponent of equation 5.3 is the RC time constant,

$$\tau = C_1 \left[R_2 \left(\frac{C_2}{C_1} + 1 \right) - R_1 \right]. \quad (5.4)$$

Equation 5.4 is derived assuming the capacitance, C_2 of the equivalent circuit is constant and is known, and compares quite well with measured values for the time constant when tested with proper capacitors for C_2 as can be seen in table 5.1. Table 5.2 compares the measured value of the RC time constant to the predicted value from the model when varying C_1 . Since $\tau \propto R_2$ changing the value of R_2 seems like a reasonable way of probing the system to look at different time scales. A smaller value of τ should allow the effects of the electrical double layer formation to be more easily observed. The double layer effects would appear in a deviation from the normal exponential decay associated with the discharge of a capacitor.

C_1 (pF)	$R_2 = 47619\Omega$		$R_2 = 4975\Omega$	
	τ_{Model}	$\tau_{Experiment}$	τ_{Model}	$\tau_{Experiment}$
560	29.50	28.76	3.06	2.94
390	21.41	21.09	2.22	2.24
150	9.99	10.56	1.04	1.09
100	7.61	8.49	0.79	0.86

Table 5.2: Comparing the model to experiment while varying C_1

5.2 Dielectric Model of Microfluidic Capacitor

There are two possible situations for the system. Case 1 will be when a step function input pulse is applied that starts at $V = 0$ for $t < 0$ and steps to $V = V_0$ at $t=0$. The second case is when the input pulse is bipolar and flips between $V = -V_0$ when $t < 0$ and $V = V_0$ when $t \geq 0$.

Case 1

When $V = 0$ at $t < 0$ the system can be thought of as a three component system with three dielectric layers, as shown in figure 5.2a. When the voltage is turned on and the electrical double layers begin to form, a five layer model becomes more appropriate, as shown in figure 5.2b. In this section a model will be developed for this formation process based on the potential and the capacitance of the system.

The three layer system, from figure 5.2a has an associated geometric capacitance, C . When the voltage is turned on, and the ions in the electrolyte begin to form the electrical double layer, the capacitance will also start to change from the geometric capacitance, however for now C will be assumed to be constant. When the voltage between the electrodes at the outside of the system, V is turned on at $t = 0$ the electrode of the capacitor will have some charge which is related to the capacitance and potential by $Q = CV$. The

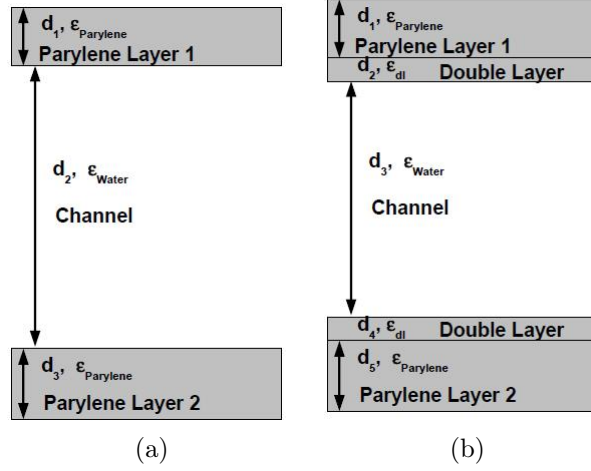


Figure 5.2: (a) Schematic of the 3 layer dielectric model at $t = 0$. The two layers of parylene have thicknesses d_1 and d_3 , and the channel has a thickness of d_2 . (b) shows a schematic of the system for $t > 0$ where there are five different regions. The double layers start to form at the boundaries of the channel and modifies the 3 layer system by placing the double layers between the channel and the parylene layers.

opposite electrode will have a charge $-Q$. The surface charge density is given by $\sigma = \frac{Q}{A} = \frac{CV}{A}$. Since at this point we can think of the system as three linear dielectrics, each region will have an associated electric field and potential drop, such that the total potential is

$$V = V_1 + V_2 + V_3 \quad (5.5)$$

where $V_i = E_i d_i$ where E_i is the electric field in that region and d_i is the thickness of that region. Rearranging equation 5.5 to solve for the potential in the channel gives $V_2 = V - V_1 - V_3$. The electric field on region 1 or region 3 can be calculated using Gauss's law[26] for linear dielectrics,

$$\oint \epsilon_1 \vec{E}_1 \cdot d\vec{A} = \frac{Q_{enc}}{\epsilon_0} \quad (5.6)$$

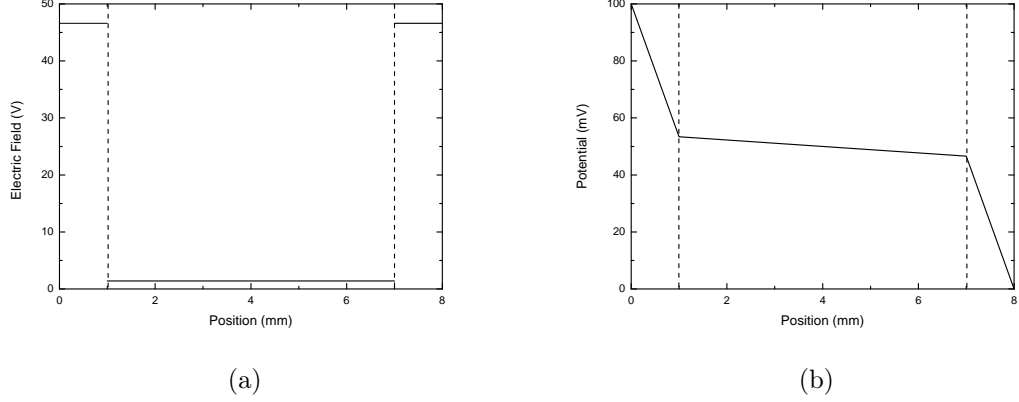


Figure 5.3: The three layer dielectric model using parameters $V = 100mV$, $A = 10^{-4}m^2$, $d_1 = d_3 = 1mm$ and $d_2 = 6mm$ and those distances, as well as the dielectric constants define the geometric capacitance as $C = 1pF$. (a)Electric field in the two parylene regions and the channel. The regions are separated with the vertical dashed lines. In each region the electric field is a constant value and is discontinuous at the boundaries. (b)Potential in the three regions. The potential is continuous, but has a different slope in the channel because of the different dielectric constant of water.

which gives the electric field in region one to be

$$E_1 = \frac{Q_{enc}}{\epsilon_1 \epsilon_0 A} = \frac{\sigma}{\epsilon_1 \epsilon_0} \quad (5.7)$$

where $\epsilon_1 = \epsilon_{parylene}$. Similarly the electric field in region 3 is $E_3 = \frac{\sigma}{\epsilon_3 \epsilon_0}$ where $\epsilon_3 = \epsilon_{parylene}$. The electrostatic boundary conditions in linear dielectrics state that

$$\epsilon_{above} E_{above} - \epsilon_{below} E_{below} = \sigma_f \quad (5.8)$$

where σ_f is the free surface charge, however, since all of the charge between two dielectric layers is bound charge, the free charge is zero between region 1 and 2, and between region 2 and 3. ($\sigma_f = 0$) So equation 5.8 simplifies to

$$\epsilon_1 E_1 = \epsilon_2 E_2$$

and gives the electric field in region 2 to be $E_2 = \frac{\sigma}{\epsilon_2 \epsilon_0}$ which is of the same form as equation 5.7, and is the same whether calculated from the top or the bottom. Combining the equations for the electric fields in the three regions with equation 5.5 gives the potential in the three regions. The electric field for the three layer model can be seen in figure 5.3a where the three regions are separated by the dashed lines. The electric field is constant in each region, but has a different value in the channel because of the different dielectric constant of water compared to that of parylene. The parameters are $V = 100mV$, $A = 10^{-4}m^2$, $d_1 = d_3 = 1mm$ and $d_2 = 6mm$ which define the geometric capacitance to be $C = 1pF$. The potential is shown in figure 5.3b. Each region shows a linear decrease in the potential, but the slope of the potential in the channel is smaller because the dielectric constant of water is larger than that of parylene. When $t > 0$ and the ions in the channel start to move, the system becomes more complicated. The original three regions turn into five regions, with the behavior of the three regions in the channel (figure 5.2b) all being time dependent. The effects of the electrical double layer increase with time, and the behavior of the bulk channel region changes to compensate. The potential in the five layer system becomes

$$V = V_1 + V_2(t) + V_3(t) + V_4(t) + V_5. \quad (5.9)$$

When rewriting in terms of the electric field, equation 5.9 becomes

$$V = E_1 d_1 + E_2(t) d_2 + E_3(t) d_3 + E_4(t) d_4 + E_5 d_5 \quad (5.10)$$

where the electric field is still given by $E_i = \frac{\sigma}{\epsilon_i \epsilon_0}$. It is expected, and seen in the simulation, that the free ions in the channel move to screen the electric field in the channel, so $E_3(t)$ should go to zero in the limit of $t = \infty$. Also, as

ions flow into the double layer region, the electric field in this region should increase. Once this charge moves into the double layer region, however, it will be modelled by thinking of it, not as a free charge, but a “fictitious” bound charge so it can be modelled as another dielectric layer. Since to change the field, the surface charge density must be changed, the time dependence in regions 2, 3 and 4 will be added to the charge density. Also, since charge is flowing from the channel (region 3) into the double layers, the charge in regions 2 and 4 is related to the charge in region 3. The surface charge density in the double layer is defined as

$$\sigma_{dl}(t) = \sigma_{dl}^{\infty}(1 - e^{-\frac{t}{\tau}}) \quad (5.11)$$

where τ is the time constant of the formation of the electrical double layer. Equation 5.11 gives $\sigma_{dl}(0) = 0$ and $\sigma_{dl}(\infty) = \sigma_{dl}^{\infty}$ so that the surface charge density is turned on when $t > 0$ and increases to a constant value. Similarly the surface charge density in the channel layer can be thought of as exponentially decaying from some starting value at time $t = 0$.

$$\sigma_{channel}(t) = \sigma_{channel}^0 e^{-\frac{t}{\tau}}$$

where τ is the same time constant as in equation 5.11 and $\sigma_{channel}(0) = \sigma_{channel}^0$ and $\sigma_{channel}(\infty) = 0$. Since, at $t = 0$ the system is a 3 layer system, $\sigma_{channel}^0 = \frac{CV}{A}$ as defined for the 3 layer system. Since the charge flowing out of the channel is related to the charge flowing into the double layer and should be proportional to the charge flowing out of the channel ($\sigma_{dl}^{\infty} \propto \sigma_{channel}^0$). Applying the time dependence to equation 5.10 gives

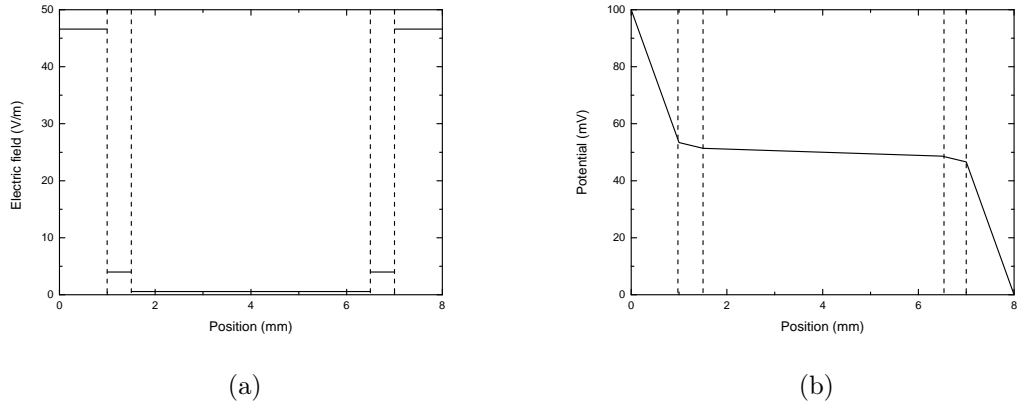


Figure 5.4: Using the same parameters as in figure 5.3 except adding $d_2 = d_4 = 0.5mm$ and changing the distance of the water layer to $d_3 = 5mm$. The regions are separated by the vertical dashed lines. (a) shows the electric field in the 5 regions. The electric field is highest in the parylene layer, and smallest in the channel and at an intermediate value in the forming double layers. (b) shows the potential in the same regions. The slope is different in each region because of the different dielectric constants, and in the 2nd, 3rd and 4th region because the surface charge density is changing.

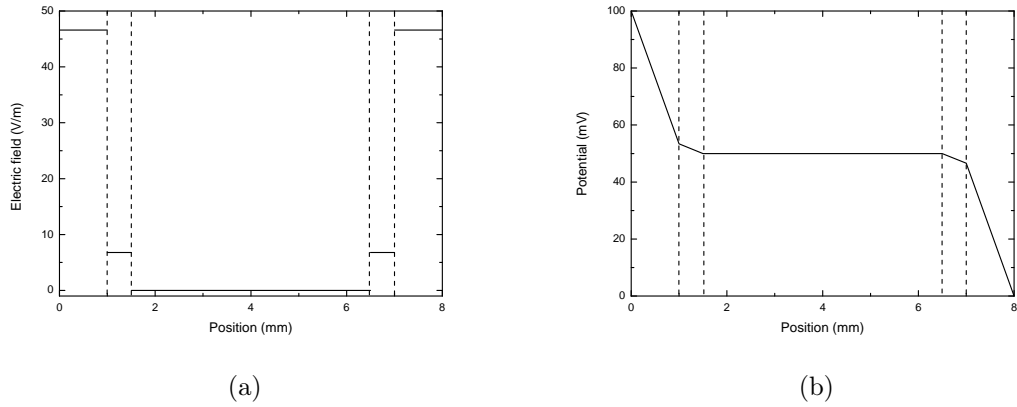


Figure 5.5: Using the same parameters as figure 5.4 but at $t = \infty$. The regions are separated by the vertical dashed line. (a) shows the electric field, where the ions have moved completely to screen the electric field in the channel so it is zero through the bulk of the electrolyte. The electric field in the double layers is at its maximum value. (b) shows the potential in the different regions. Since the electric field in the electrolyte is zero, the potential through the electrolyte is constant. The double layer has its maximum potential drop across it at $t = \infty$.

$$V = \frac{\sigma d_1}{\epsilon_{\text{parylene}} \epsilon_0} + \frac{\sigma_{dl}^\infty d_2 (1 - e^{-\frac{t}{\tau}})}{\epsilon_{dl} \epsilon_0} + \frac{\sigma d_3 e^{-\frac{t}{\tau}}}{\epsilon_{\text{water}} \epsilon_0} + \frac{\sigma_{dl}^\infty d_4 (1 - e^{-\frac{t}{\tau}})}{\epsilon_{dl} \epsilon_0} + \frac{\sigma d_5}{\epsilon_{\text{parylene}} \epsilon_0}. \quad (5.12)$$

Equation 5.12 represents the total potential across the device at intermediate times. Figure 5.4a shows the electric field in the five different regions at some intermediate time where the double layer has started to form, so the electric field in it is higher than the electric field in the bulk of the electrolyte. As the electric field in the forming double layer becomes different from that in the bulk electrolyte there is a potential drop across it, as seen in figure 5.4b. This potential drop has a different slope than in the electrolyte because of the different dielectric constant in the double layer. The effective dielectric constant of the double layer can vary[7] between $\epsilon_{dl} = 6 - 32$, so $\epsilon_{dl} = 20$ was chosen. As time progresses the potential drop across the double layers increases and the potential across the channel in region 3 decreases. At $t = \infty$ the surface charge density in region 3 goes to zero, and so does the electric field as seen in figure 5.5a and the potential in the bulk electrolyte remains constant, as seen in figure 5.5b. If a bipolar input pulse, which varies from $-V_0$ to V_0 instead of 0 to V_0 , is used, the bulk electrolyte has a value of the potential, $V = 0$, as long as the two parylene layers are the same thickness. At $t = \infty$ equation 5.12 becomes

$$V = \frac{\sigma d_1}{\epsilon_{\text{parylene}} \epsilon_0} + \frac{\sigma_{dl}^\infty d_2}{\epsilon_{dl} \epsilon_0} + \frac{\sigma_{dl}^\infty d_4}{\epsilon_{dl} \epsilon_0} + \frac{\sigma d_5}{\epsilon_{\text{parylene}} \epsilon_0}. \quad (5.13)$$

The thickness of the electrical double layers, $d_2 = d_4 = \lambda_d$, which is a function of the concentration of the solution. The electric field in the channel, as a

function of time is the electric field in region 3 and is given by

$$E_c(t) = \frac{\sigma e^{-\frac{t}{\tau}}}{\epsilon_{water}\epsilon_0} \quad (5.14)$$

where d_c is the depth of the channel. The reason that the electric field is of interest is to calculate specifically the displacement current in the channel. The displacement current is given by[27]

$$I_d(t) = \epsilon_{water}\epsilon_0 \frac{d\Phi}{dt} \quad (5.15)$$

where the flux, $\Phi = E_c(t)A$. This allows an analytic equation for the displacement current, which is

$$I_d(t) = -\frac{A\sigma}{\tau} e^{-\frac{t}{\tau}}. \quad (5.16)$$

This “displacement current” is caused by the motion of ions in the channel, which are prevented from being a “real” current in the external circuit because of the insulating parylene layer, preventing the charge to be physically moved out of the channel. Though this current has the correct form, it is negative which does not make sense. This equation does not include the current in the circuit. The current in the external circuit, when the double layer is in equilibrium, has an equivalent capacitance, C_{eq} , which includes the capacitance of the wires and oscilloscope, as well as the device with the formed double layer, as well as the equivalent resistance, R_{eq} which consists of the resistance of the oscilloscope, as well as that of the variable load resistor. The current from this is defined as

$$I_{RC}(t) = \frac{V}{R_{eq}} e^{-\frac{t}{R_{eq}C_{eq}}}. \quad (5.17)$$

The total current defined similarly as in the Morrow and Franceschetti work, is the sum of these two currents. The sign of the displacement current is wrong, suggesting this method is incorrect. To arbitrarily make the displacement current positive. The total current is given by

$$I(t) = I_{RC}(t) + |I_d(t)| = \frac{V}{R_{eq}} e^{-\frac{t}{R_{eq}C_{eq}}} + \frac{A\sigma}{\tau} e^{-\frac{t}{\tau}}. \quad (5.18)$$

So far in this derivation, the capacitance of the device has been assumed to be constant. However, as the system evolves, with the three inner layers evolving in time, the capacitance also changes. If we start with the 5 layer system, it can be modeled as five capacitors in series, where the equivalent capacitance is given by

$$\frac{1}{C_{eq}} = \frac{1}{C_1} + \frac{1}{C_2} + \frac{1}{C_3} + \frac{1}{C_4} + \frac{1}{C_5}$$

where C_1 is the capacitance of region 1, C_2 is the capacitance of region 2, and so on. C_1 and C_5 are constant in time, and are just given by the geometric capacitances of the parylene layers, however $C_2 = C_4 = C_{dl}^\infty = \frac{\epsilon_{dl}\epsilon_0 A}{\lambda_D}$ and $C_3^0 = \frac{\epsilon_{water}\epsilon_0 A}{d_c}$ when both are in equilibrium. However, at $t = 0$ the electrical double layer hasn't started forming so there is no voltage drop across it, and at $t = \infty$ there is no voltage drop through the channel, so in both cases, the capacitance, as defined by $C = \frac{Q}{V}$, is infinite. When any of the capacitances is infinite, it doesn't contribute to the equivalent capacitance of the system. The time dependent double layer capacitance will be defined as

$$C_{dl}(t) = \frac{C_{dl}^\infty}{1 - e^{-\frac{t}{\tau}}} \quad (5.19)$$

and the time dependent capacitance of the channel is given by

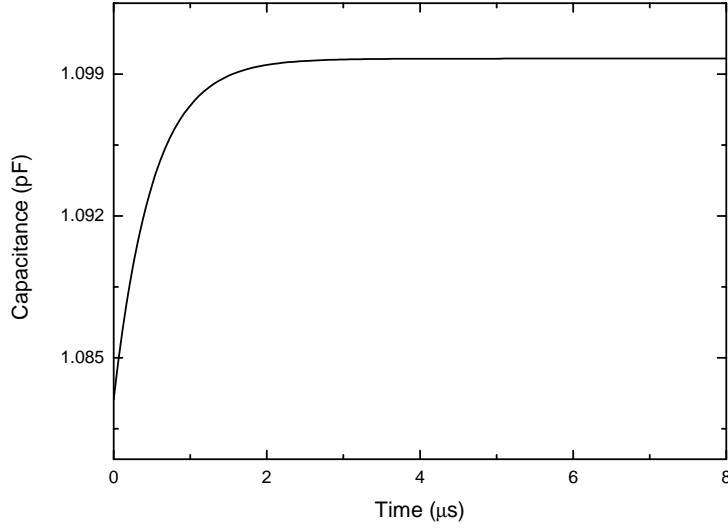


Figure 5.6: Using the same parameters as for figure 5.4 and 5.5 as well as a double layer formation time of $\tau = 500ns$ the time dependent capacitance from equation 5.21 is plotted against time, showing an exponential increase from the value of the three layer dielectric to the final value of the capacitance.

$$C_c(t) = \frac{C_3^0}{e^{-\frac{t}{\tau}}}. \quad (5.20)$$

The equivalent capacitance can then be defined as

$$\frac{1}{C_{eq}(t)} = \frac{1}{C_1} + \frac{2(1 - e^{-\frac{t}{\tau}})}{C_{dl}^\infty} + \frac{e^{-\frac{t}{\tau}}}{C_3^0} + \frac{1}{C_5}. \quad (5.21)$$

Figure 5.6 shows the time dependent capacitance defined with equation 5.21 for the same parameters used to illustrate the electric field and potential behavior of the model, as well as a characteristic double layer formation time of $\tau = 500ns$. This shows the capacitor starting at the geometric capacitance of the three layer dielectric system and increasing in an exponential manner to the equilibrium value of the 4 layer system. The intermediate region is the time when all 5 layers are contributing to the equivalent capacitance of the sample. Figure 5.7 shows the displacement current calculated from equation

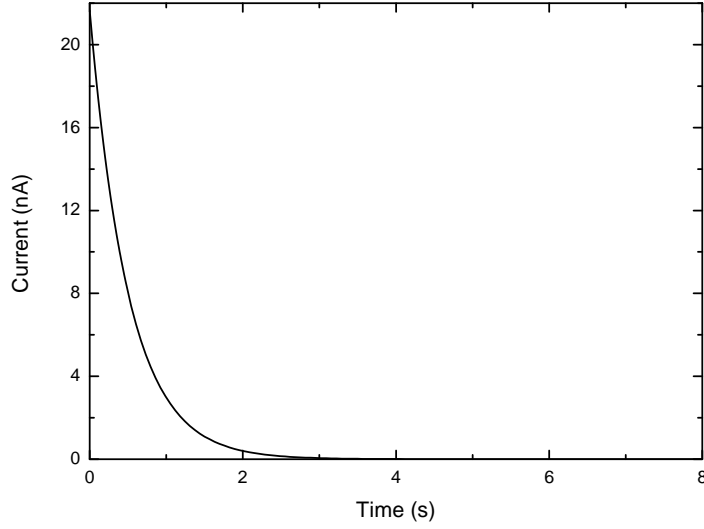


Figure 5.7: Shows the displacement current calculated from equation 5.16 using the parameters used in the previous figures. These parameters cause a small change in the electric field so the displacement current is quite small.

5.16 including the time dependent contribution to the surface charge density from the capacitor. The parameters used produce a small change in the electric field so the displacement current is quite small. To be able to compare the predicted displacement current with the RC current more realistic values for the thicknesses of each of the layers will need to be chosen. The parameters chosen for here were to make it easy to visualize the behavior in the different regions.

Figure 5.9 shows a comparison using more realistic parameters, such as parylene layers $d_1 = d_5 = 100nm$, a channel depth of $d_3 = 9\mu m$, a concentration of $p_0 = 1 * 10^{-5}mol/L$ which defines the thickness of the double layers, $d_2 = d_4 = \lambda_D = 96.1nm$. These parameters define a capacitance in equilibrium of $C_{max} = 10.4nF$, and an equivalent resistance of $R_{eq} = 50\Omega$ was used to calculate the RC current. An infinite rise time step function was used, with a magnitude of $V_0 = 10mV$. Figure 5.8 shows the total current using these

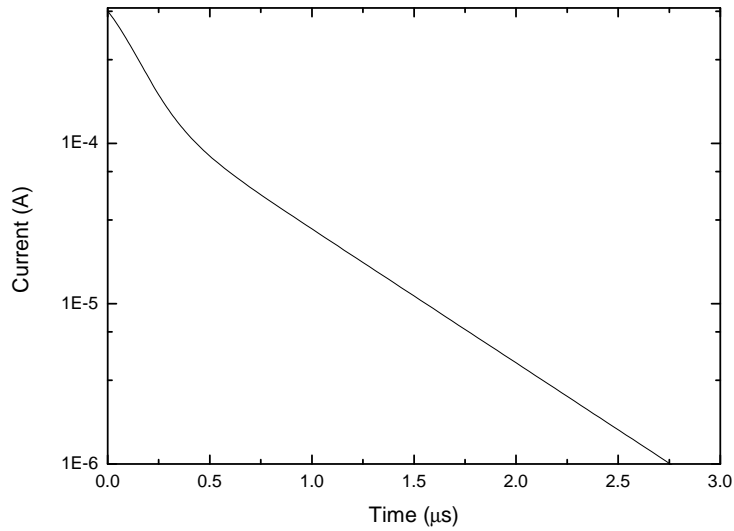


Figure 5.8: Shows the total current, calculated from equation 5.18 using a double layer formation time of $\tau = 100ns$, parylene layer thicknesses of $d_1 = d_5 = 200nm$, a channel thickness of $d_3 = 9\mu m$, a concentration of $1 * 10^{-5}mol/L$, which defines the Debye length, $\lambda_D = 96.1nm$, which is the thickness of the two double layers. The dielectric constants used earlier were used here as well. These parameters define a maximum capacitance of $C_{max} = 10.4nF$ and an equivalent resistance of $R_{eq} = 50\Omega$ was used for the RC current.

parameters as a function of time, plotted on a logarithmic scale. This shows the two regimes, the short time regime, showing the displacement current, which has a characteristic formation time of $\tau = 100ns$, and the longer time regime with the RC exponential decay. This looks qualitatively like the current produced in the experiment, however the capacitance calculated using the geometry of the device doesn't compare well with the capacitance measured in the experiment, so to use this model to make quantitative comparisons, the capacitance equation will need to be modified slightly so that a more accurate capacitance can be used.

A comparison of one of the experimental curves taken with $R = 50\Omega$ variable load resistance compared with the model both with the time dependent capacitance from equation 5.19 (red) and with a constant capacitance (blue) is shown in figure 5.9. The natural logarithm of the current is plotted against time for all three, but the model currents are shifted down slightly because an infinite rise time voltage pulse ($V_0 = 10mV$) causes a larger initial current than a finite rise time pulse. The capacitor model was adjusted to give an equilibrium capacitance of $C_{eq} = 25.5nF$. This capacitance was used for the time independent capacitance. The difference in the slope for the long time behavior is because tweaking the capacitance for the model couldn't get closer to the experimental capacitance ($C_{exp} = 22.8nF$). The model uses a double layer formation time of $\tau = 200ns$ for the time dependent capacitance model, and $\tau = 400ns$ for the time independent capacitance model. The red curve shows a slight downturn at the earliest times, which qualitatively does not agree with the experiment. Although the agreement between the blue curve and the experiment is not perfect, it is better than the red curve, and the value of the double layer formation time was very similar to that found in the experiment ($\tau_{exp} = 390ns$), whereas the double layer formation time constant

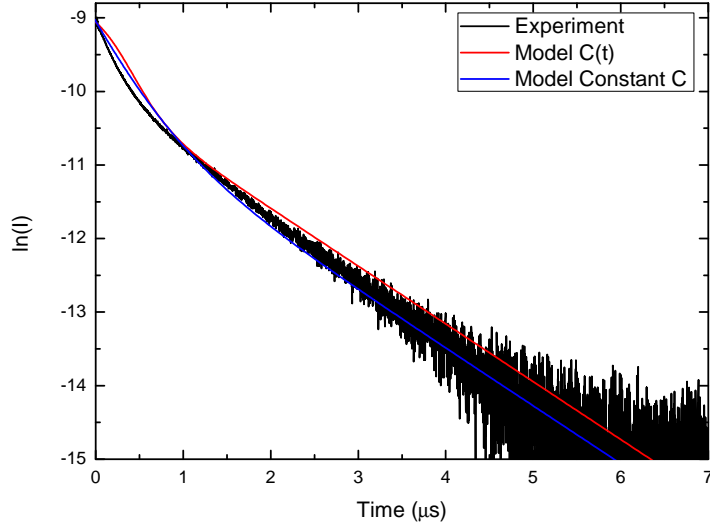


Figure 5.9: The experiment compared to the model from Case 1 plotting the natural logarithm of the current against time for both the time dependent capacitance (red) and time independent capacitance (blue). The experiment has an equilibrium capacitance of $C_{exp} = 22.8nF$ and the capacitor model was tweaked to to have an equilibrium capacitance of $C_{eq} = 25.5nF$. This was the the value that was used for the time independent capacitance. The double layer formation time for the time dependent capacitance plot was $\tau = 200ns$ and for the time independent capacitance $\tau = 400ns$. An infinite rise time $V_0 = 10mV$ input voltage pulse. The model current was shifted down, because using an infinite rise time pulse makes the current larger. An external circuit resistance of $R = 50\Omega$ was used in the experiment and the model.

chosen for the time dependent capacitance model was chosen for the best fit, not based on a value close to the experiments.

Case 2

The difference between the bipolar case and case 1 is in the initial conditions. When the system has reached equilibrium with $V = -V_0$ applied to the sample, it starts out with fully formed electrical double layers. The system has capacitances from both electrical double layers, as well as from both parylene layers. When the voltage is initially switched, the transient current is then

not from the formation of the electrical double layer, but from its discharge. It could also be argued that the formation of the electrical double layer can't form faster than the RC time of the total circuit, because this RC time constant is going to be the relevant time scale of the potential drop across the sample. If we think of the sample as a simple capacitor, the potential drop across it is going to be given by

$$\Delta V_{Sample} = V_0(1 - e^{-\frac{t}{RC_{sample}}}) \quad (5.22)$$

and the ions in the electrolyte are going to be driven harder at later times when the potential drop across the sample is larger. This goes against the interpretation in case 1, where the transient current is given by the formation of the electrical double layer, which is happening faster than everything else.

Starting from equation 5.10 again, but modifying the time dependence of the electric field in a different way for the discharge, rather than formation of the electric field is a natural place to start. The electric field is again given by $E_i(t) = \frac{\sigma_i(t)}{\epsilon_i \epsilon_0}$. Since the double layer starts off fully formed its expression needs to start at a maximum value and end at $\sigma_{dl} = 0$ and in the channel, the surface charge density needs to start at zero and end at its maximum value. This can be achieved by applying the opposite time dependences as in case 1, where this time $\sigma_{dl}(t) = \sigma_{dl}^0(1 - e^{-\frac{t}{\tau}})$ and the surface charge density in the channel is given by $\sigma_c(t) = \sigma_c^\infty e^{-\frac{t}{\tau}}$. Applying this, and finding the displacement current gives the same magnitude as equation 5.16 except the current is positive. Since the double layer forms at the same time scale as the external circuit, it won't need to be included as another term in the current. However, since the potential change at $t = 0$ is now twice as large, the voltage in the RC current needs to be multiplied by a factor of two. A fit parameter for the external circuit current will also be used to account for any voltage division of the initial input

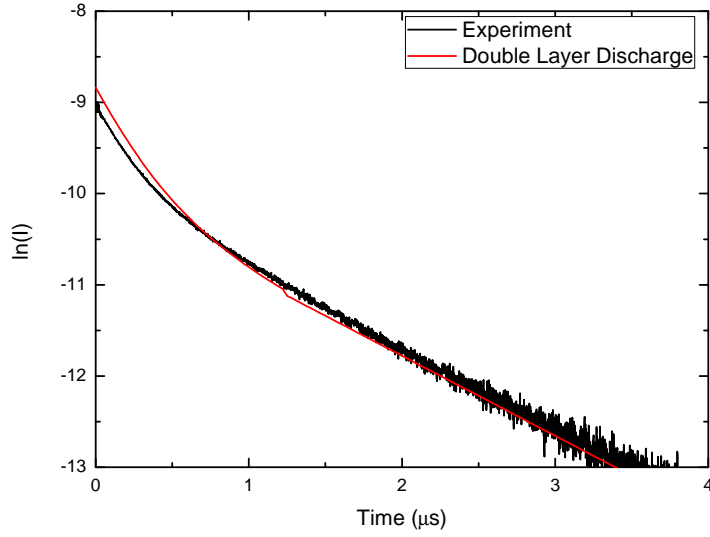


Figure 5.10: The model found in Case 2 compared against the same experimental data. The model uses the same capacitance as in figure 5.9, but $\tau = 250ns$. The red (Double layer discharge model) curve was also shifted down slightly.

pulse by the resistive elements in the circuit. Putting the RC current and the double layer current together gives

$$I = \frac{2V_0}{R_{eq}} e^{-\frac{t}{R_{eq}C_{eq}}} + \frac{A\sigma}{\tau} e^{-\frac{t}{\tau}} \quad (5.23)$$

which is the same final result as in case 1, however it didn't need to have any arbitrary sign changes made on the displacement current. It also assumed the same initial conditions as were found in the experiment. Figure 5.10 shows this model compared to the experiment. The same external circuit parameters as in figure 5.9 were used ($R_{eq} = 50\Omega$, $C = 25.5nF$) but a different double layer time constant was used ($\tau = 250ns$) and the plot from the model had to be shifted down to lay onto the experimental data. However, there is good qualitative agreement, with the model picking up both the short time scale, and long time scale features. Another important distinction with this model is that the argument that the transient current is from the discharge of the

electrical double layer, and not the charging of it, can be tested. If the charging really happens at the same time scale as the RC time constant of the circuit, this could be seen by applying a pulse from $V = 0$ to $V = V_0$. If the arguments in this case are correct, no transient behavior would be seen in that situation. This would provide evidence that the model in case 2 is qualitatively correct, but needs modification to better fit the behavior quantitatively.

Figure 5.10 shows the results subtracting a single offset from the total current. However, justification can be made for having separate fit parameters on the external circuit term and on the double layer discharge term. For the low resistances, the response was scaled, as if the initial pulse was scaled by a voltage divider in the circuit. Equation 5.23 uses the surface charge density that would be found on one plate of the capacitor, but in the channel it makes sense that only a fraction of this charge is moved, due to screening of the dielectric layers. Another fit parameter can be used for this term. This will modify equation 5.23 to become

$$I = \frac{a2V_0}{R_{eq}} e^{-\frac{t}{R_{eq}C_{eq}}} + \frac{bA\sigma}{\tau} e^{-\frac{t}{\tau}} \quad (5.24)$$

where a is the “voltage divider” scaling factor and b is the fraction of the surface charge on that plate that is used to form the double layer. Figure 5.11 shows the fit to equation 5.24 and gives $\tau = 375.1 \pm 0.1ns$, $a = 0.1651 \pm 0.0002$ and $b = 0.5802 \pm 0.0004$. Its not surprising that a better fit is found using equation 5.24 because it has more flexibility. Although the fit parameters can be justified, it would be expected that a would be the same throughout the experiment, which it is not. Its justification as a voltage dividing scaling factor is probably not correct. For all of the samples, the values of the double layer discharge time constant ranges from $\tau = 37.9 \pm 0.1ns \rightarrow 439.7 \pm 0.2ns$ and was within this range no matter the thickness of the parylene layer on the top

plate. From all of the data the equation for the time constant as a function of the ion density is found to be

$$\tau = (47 \pm 5)p_0^{-0.15 \pm 0.01} ns. \quad (5.25)$$

This does not compare well with the power law equation from the simulation, which was found to have an exponent of approximately $-\frac{1}{2}$. The actual measured time constants in the experiment ranged from $\approx 500ns$ and decreased down to $\approx 50ns$ as the concentration was increased, however once the concentration increased to greater than $\sim 0.001mol/L$ the double layer time constant could not be measured accurately, so it is expected to get smaller than $50ns$. Equation 5.23 can be used to estimate the time constants for higher potentials although not having the data, the predicted time constants should be used as a guideline.

Lastly, using the displacement current in the channel, the magnetic field in the channel can be calculated using Ampere's law[28]

$$\oint \vec{B} \cdot d\vec{l} = \mu_0(I_c + I_d)_{enc}. \quad (5.26)$$

However, since in the channel there is only the displacement current, equation 5.26 reduces to

$$\oint \vec{B} \cdot d\vec{l} = \mu_0 I_d. \quad (5.27)$$

The capacitor is a square, a magnetic sensor would want to be placed farther away than the diagonal from the center of the capacitor to one of the corners. In such a case, the magnetic field would be

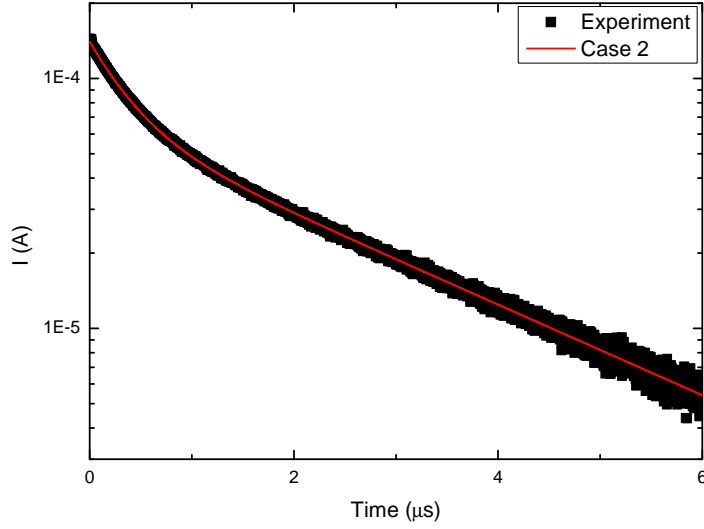


Figure 5.11: Shows the fit of equation 5.24 to the raw data for $1 * 10^{-5} mol/L$ KCl for the 290nm thick parylene layer on the top plate. τ , a and b were used as fit parameters and it was found that $\tau = 375.1 \pm 0.1 ns$, $a = 0.1651 \pm 0.0002$ and $b = 0.5802 \pm 0.0004$. This modified fit (equation 5.24) gives a much better fit than equation 5.10.

$$B = \frac{\mu_0 I_d}{2\pi r} \quad (5.28)$$

where r is the distance from the center of the capacitor and $r > \sqrt{2}L$ where L is the length of the sides of the square capacitor. If the magnetic sensor was placed in the channel, the displacement current would have to be modified because not all of the area of the capacitor would be enclosed in an Amperian loop. For typical parameters this gives a maximum magnetic field of approximately $B = 5 * 10^{-5} gauss$.

5.3 Analysis

5.3.1 Initial Data Analysis

As a first check to make sure the devices are behaving properly, the capacitance of the devices with the channel only containing air will be measured and compared to the expected values of the capacitance for a capacitor with three dielectric layers. A capacitor with three dielectric layers can be modeled as three capacitors in series, with each capacitor having the geometric capacitance of that layer. Since the device uses the same microchannel bottom plate and just varies the top plate, the thickness of the parylene layer on the bottom plate is constant ($d = 103nm$) and the depth of the channel is also constant ($d = 9\mu m$), so the only parameter that is varied is the thickness of the parylene layer on the top plate, which varies from $2.7nm$ to $373nm$. Figure 5.12 shows how the capacitance should vary with top layer thickness according to the simple capacitor model. Its variation is quite small and the measured capacitances don't show any trend based on their thicknesses, however, they are reasonably close to the values that are expected, only off by $\sim 10\%$. This could easily be accounted for by slight misalignment of the electrodes, or stray capacitances from the micropatterned leads which were not accounted for. These measurements don't show the expected trend, however appear to be reasonable enough to suggest that the devices are working as designed. When the channel is filled with water, which has a much higher dielectric constant than air, the dependence of capacitance on thickness (neglecting the double layers) is expected to be much larger.

The microfluidic structure that allows the probing of the electrical double layer can be thought of like the schematic in figure 5.13 where the capacitance of the electrical double layer is time dependent. Then the equivalent

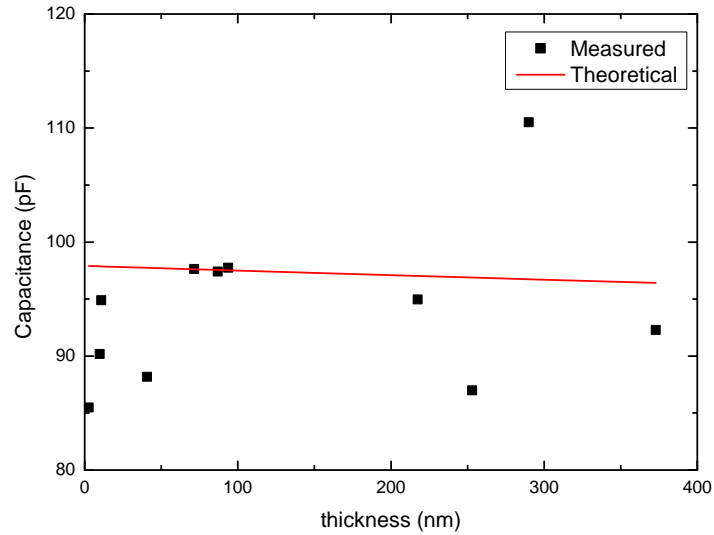


Figure 5.12: Shows how the capacitance is expected to vary with the thickness of the top plate parylene layer with air filling the microchannel in red, and the measured values of the capacitance in black. The bottom plate parylene thickness was 103nm and the channel thickness was $9\mu\text{m}$.

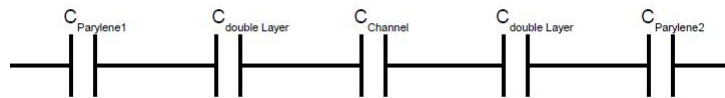


Figure 5.13: Schematic of the different components of the capacitances of the microfluidic structure. The capacitances of the Parylene layers as well as the channels are fixed based on the thicknesses of the parylene layers and their dielectric constants, as well as the depth of the channel and dielectric constant of water. The capacitance of the electrical double layer are time dependent, reaching its final value once the system has reached equilibrium.

capacitance will be given by

$$\frac{1}{C_{eq}} = \frac{1}{C_{Parylene1}} + \frac{1}{C_{Parylene2}} + \frac{1}{C_{Channel}} + \frac{2}{C_{DoubleLayer}(t)} \quad (5.29)$$

where each capacitance is defined by its geometric capacitance ($C = \frac{\epsilon A}{d}$). To ensure that before the formation of the electrical double layer its capacitance has no effect on the equivalent capacitance of the circuit, at $t=0$ $C_{DoubleLayer} = \infty$. Although this at first seems like an odd way to treat the capacitance, it can be imagined that the “thickness” of the double layer at this point is zero, which would lead to the infinite double layer capacitance before the input of a voltage.

The time dependence of the input voltage pulse and of the response are both recorded using the oscilloscope into data files which can be analyzed. An example of one of the raw data for the response can be seen in figure 5.14 along with the input voltage pulse which caused this response. The sample used in this measurement had parylene layers of $217.5 \pm 0.7nm$ for the top plate and $103.0 \pm 0.5nm$ for the bottom plate, and it can be seen that the peak-to-peak amplitude of the input pulse is larger than the height of the pulse. This voltage drop can be attributed to the parylene layers and this maximum amplitude of the response varied with the thickness of the parylene, though not as predictably as was expected.

Since the input pulse was recorded for each experiment, the maximum height of each response, normalized with the input pulse was plotted against the thickness of the parylene layer on the top plate. The bottom plate had a consistent parylene layer thickness of $103.0 \pm 0.5nm$. Figure 5.15 shows a lot more spread than expected. A much more consistent trend was expected

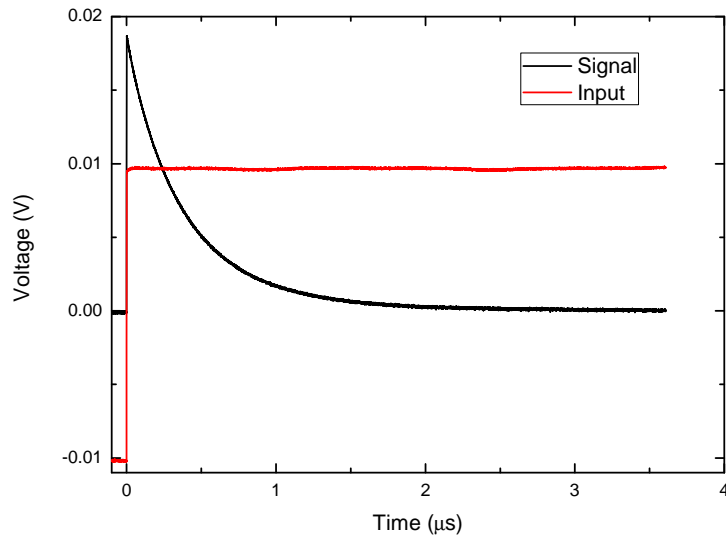


Figure 5.14: Shows a sample plot of the raw data of an input square wave voltage pulse and a sample response with $R_2 = 50\Omega$ and a concentration of $1 * 10^{-5} mol/L$.

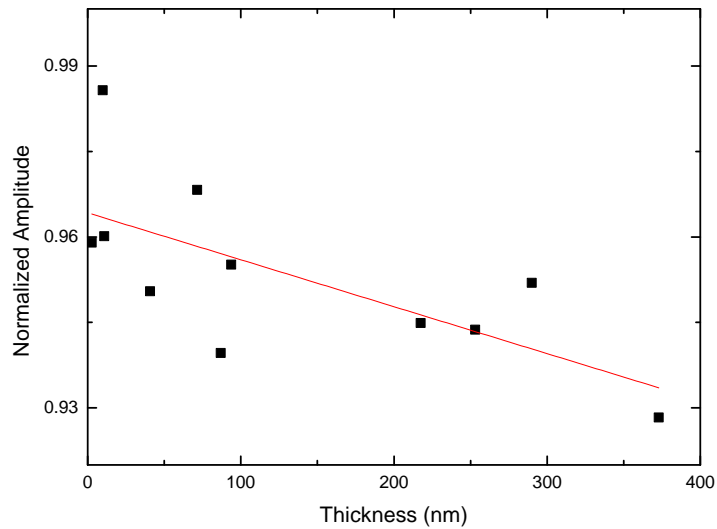


Figure 5.15: Maximum height of the response signal normalized with the peak to peak voltage of the pulse that it is in response to. The red line is a line of best fit.

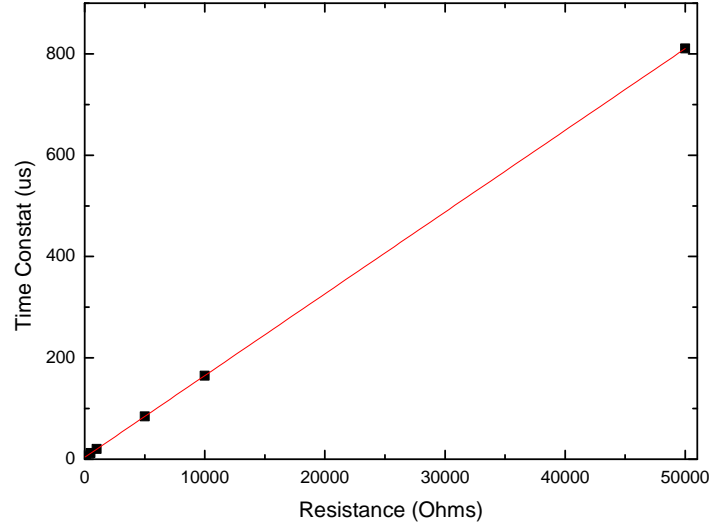


Figure 5.16: Plotting the exponential decay's time constant, τ vs R allows the capacitance of the system to be determined from the relationship $\tau = RC$ where the slope of the linear fit is the capacitance. This particular plot shows the top plate with a 93.8nm parylene layer and the capacitance of the system in this case would be 16.1nF.

for the voltage drop across the parylene layer, however the trend still shows a potential drop as the parylene gets thicker. Figure 5.15 shows that the potential drop across the parylene is quite small.

The variable resistor used in parallel with the oscilloscope has seven different resistance values (50k Ω , 10k Ω , 5k Ω , 1k Ω , 500 Ω , 100 Ω and 50 Ω) which makes it easy to probe different timescales. The equation relating the time constant to the resistance for an exponential decay of an RC circuit is $\tau = RC$ so plotting τ vs R gives the capacitance, C directly from the slope of the graph. Figure 5.16 shows the time constant plotted against the resistance for the top plate with a 93.8nm layer of parylene which has an equivalent capacitance of 16.1nF if this is to be interpreted entirely as a capacitance. The linear fit looks very good for the resistances ranging from 50000 Ω to 500 Ω but deviations at the 100 Ω and 50 Ω points are apparent. This suggests that the effect of the

electrical double layer is not being masked at these smaller time scales.

For this experiment both the concentration of the Potassium Chloride (KCl) solution and the thickness of the parylene layer of the top plate were varied. The top plate thickness varied from 2.7nm-373nm. The concentration of the KCl solution was varied from 0.1mol/L - $1 * 10^{-6}$ mol/L.

A bit of data analysis needs to be done on the raw data. A sample raw data curve can be seen in figure 5.17 which shows the device response in black to the input square wave in red. A large, exaggerated offset of the response can be seen. This offset is from the function generator. Because the square wave switches between $-V_0$ to V_0 , the offset in front of the rise in the response could include some non zero current from the previous decay from the $-V_0$ portion of the square wave. Because of this the response was recorded for both the positive portion of the pulse, zoomed in to the initial decay, as well as the negative portion of the pulse. This was done so that the tail of the positive decay would be picked up in the negative response, and the negative response tail is picked up at the beginning of the positive response. It is also important to choose the frequency of the input pulse so that there are several time constants within the cycle to ensure that the response has a chance to decay to a constant value. The offsets for both the negative and positive portions of the response are subtracted from the signal. The positive and negative responses after the subtraction of the offsets can be seen in figure 5.18 which also has the responses triggered at the same time, since they are recorded in two separate files. Since the voltage decay is exponential, (of the form $V \sim e^{-t/\tau}$) the time constant can be found from the slope of the plot of $\ln(V)$ vs t . Figure 5.19 shows the natural logarithm of the positive response and the natural logarithm of $-V$ for the negative response for the sample with a 103nm layer of Parylene for the bottom plate and a 93.8nm layer of parylene

for the top plate with a $1 * 10^{-5} mol/L$ concentration of KCl measured across a 50Ω resistor. The graph shows two distinct regions of the decay, a fast non linear portion at the beginning and a slower linear portion, which has a time constant, $\tau_1 = 2.2\mu s$.

5.3.2 Data Driven Model

This fast non linear portion shows up only for small resistances and gets faster as the concentration of the KCl solution increases. Since as the resistance is decreased shorter time scales are probed, this suggests that this feature is related to the electrical double layer dynamics. To add further support to this non linear feature being related to the double layer dynamics, the fact that it decays to the linear region faster as the concentration increases, similarly to the fact that the double layer time constant decreases with increasing concentration. Since the time constant, τ is obtained from the linearized decay curve, and is related to the RC characteristics of the circuit, the non linear portion of the graph also makes sense because the capacitance of the device would be changing with respect to time and should produce some time dependent behavior that would appear as a non linear part to the otherwise linear $\ln(V)$ vs t relationship. To further look at this, first a linear fit was done on the data, and the linear “background” was subtracted from the signal. This can be seen in figure 5.20. The behavior in the short time scales still appears not to be linear. The data looks like it might again be an exponential decay, so to check this, the natural logarithm of this data is taken one more time. Figure 5.21 shows that the non linear part displayed exponential behavior after the first natural logarithm was taken. This suggests a physical model such as

$$V = V_0 e^{-\frac{t}{\tau_1} + A e^{-\frac{t}{\tau_2}}} \quad (5.30)$$

where V_0 is the maximum amplitude of the initial response if there was no non linear part. τ_1 is the RC time constant for the component of the circuit that is not time dependent. τ_2 is the time constant of the electrical double layer formation and A is a fitting constant. If a linear fit is done to the data in figure 5.21 all of the fit parameters can be extracted and the curve from equation 5.30 can be constructed and compared to the raw data. Figure 5.22 shows how the empirical model fits to the raw data. Figure 5.22a shows the fit between the raw data and equation 5.30 directly, showing very good agreement. Figure 5.22b shows the fit between the natural logarithm of the data to the natural logarithm of equation 5.30, also showing excellent agreement, further supporting the use of this pieced-together model. Using this model allows an easy way to extract a “time constant” for the formation of the electrical double layer which can then be compared to the formation times from the FCT simulation. For most of the data, this fast, non linear component was not present, and in those cases, just the model $V = V_0 e^{-\frac{t}{\tau}}$ can be used to find the time constant. This time constant should be the time constant of the entire system, including the sample while it is in equilibrium with the applied voltage pulse. Being in equilibrium, the electrical double layer should be formed and be contributing fully to the capacitance of the system.

5.4 Results

The total capacitance can be calculated using equation 5.29. The double layer capacitance is given by $C_{DoubleLayer} = \frac{\epsilon_{DoubleLayer} A}{\lambda_D}$. The Debye length, λ_D , is the thickness of the double layer and is calculated using equation 4.1 and the dielectric constant of the double layer is $\epsilon_{DoubleLayer} = 20$, which is in the middle of the range of dielectric constants quoted for the double layer.[7] Figure

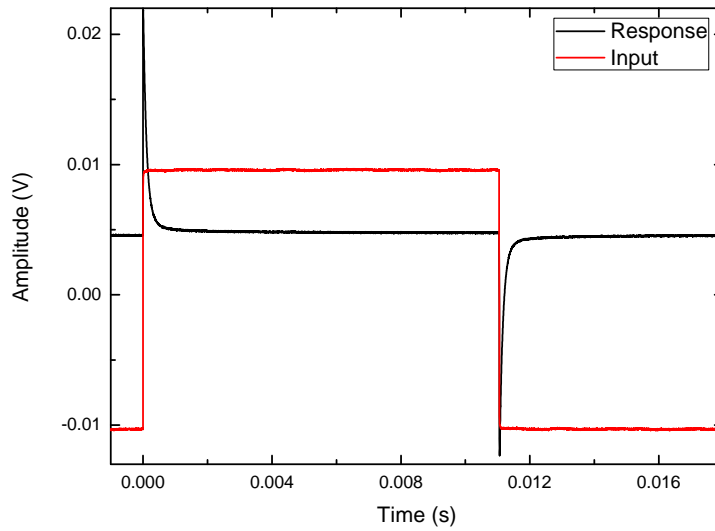


Figure 5.17: The raw signal from the oscilloscope for the response of the device in black, and of the input square wave in red. A large, exaggerated offset can be observed in the response signal. This curve was taken with de-ionized water with a load resistance of $10k\Omega$. The offset from before $t = 0$ is subtracted from the curve corresponding to the drop in voltage of the square wave. The offset immediately before the drop in voltage is subtracted from the curve corresponding to the rise in voltage of the square wave.

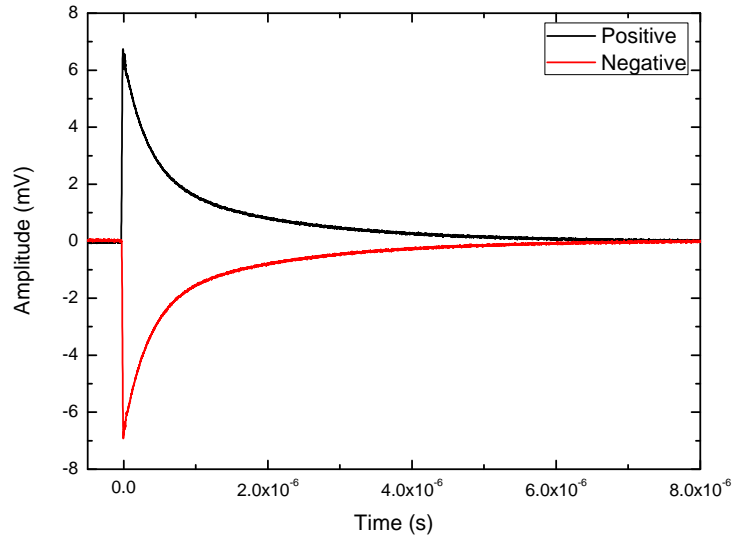


Figure 5.18: Shows the positive (black) and negative (red) portions of the response for a sample with a top plate parylene layer of thickness 253nm, a concentration of $1 * 10^{-5} mol/L$ KCl and a load resistance of 50Ω after the offsets have been subtracted. Because they are taken with two separate files they are triggered with the change in slope of the input pulse.

5.23 shows the theoretical capacitance for a few different thicknesses. It can be seen that as the concentration of the liquid increases so does the capacitance of the device. The dependence on the thickness of the parylene layer on the top plate can be seen, as the thickness of the parylene layer is increased the overall capacitance of the device decreases. In the experiment, the time constant is measured from the voltage decay. This can be converted to the capacitance by dividing it by the equivalent resistance of the system. Figure 5.24 shows two of these where (a) has a load resistance of 5000Ω and (b) has a load resistance of 10000Ω . Unfortunately the experimental capacitance's are off in their absolute values from the theoretical ones by a significant margin, and the thickness scaling is not the same. They still follow the same trends with the capacitance increasing as the concentration increases, as well as the capacitance decreasing as the thickness of the top plate parylene layer increases. This is how the

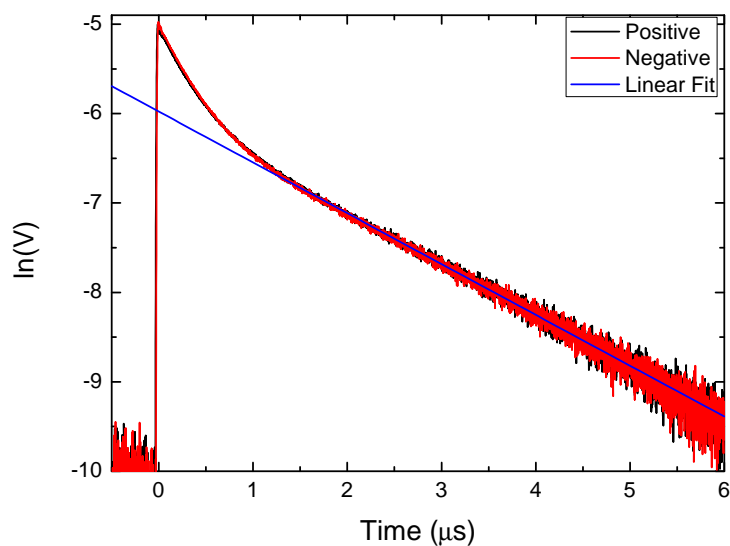


Figure 5.19: The natural log of V plotted against time of the positive (black) response and the natural log of $-V$ plotted against time of the negative (red) response of the 253nm top plate sample with a concentration of $1 * 10^{-5} mol/L$ KCl measured across a 50Ω resistance. A linear fit to the data is in blue with a time constant of $\tau_1 = 2.2\mu s$. The portion at the beginning which does not fit with the linear trend at the end only appears for small resistances and becomes smaller as the concentration of the KCl solution is increased.

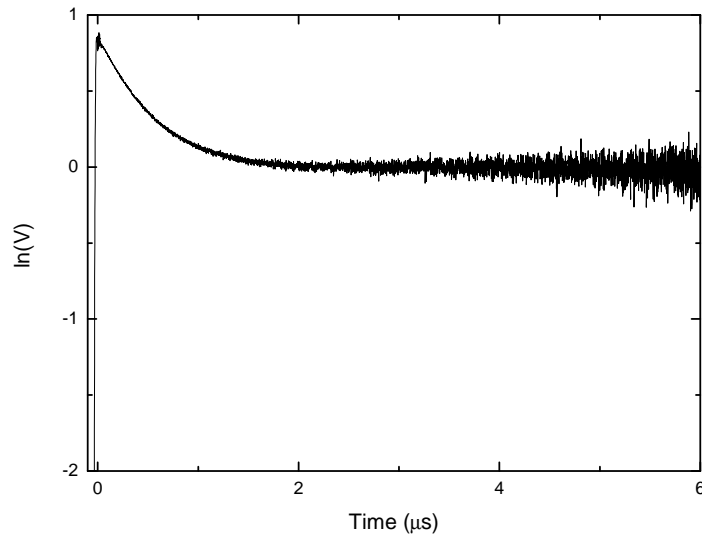


Figure 5.20: A plot of raw natural logarithm of the voltage signal after the linear fit has been subtracted from the signal, zoomed in to the non linear portion of the graph. The behavior in the short time scale still does appear not to be linear.

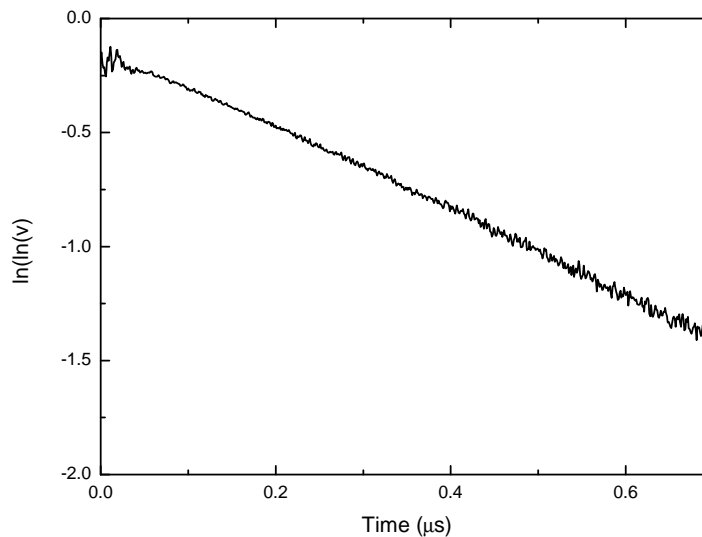


Figure 5.21: A zoomed in look at the non linear part of figure 5.20 after the natural logarithm has been taken after. A linear fit is taken to get A and τ_2 from equation 5.30.

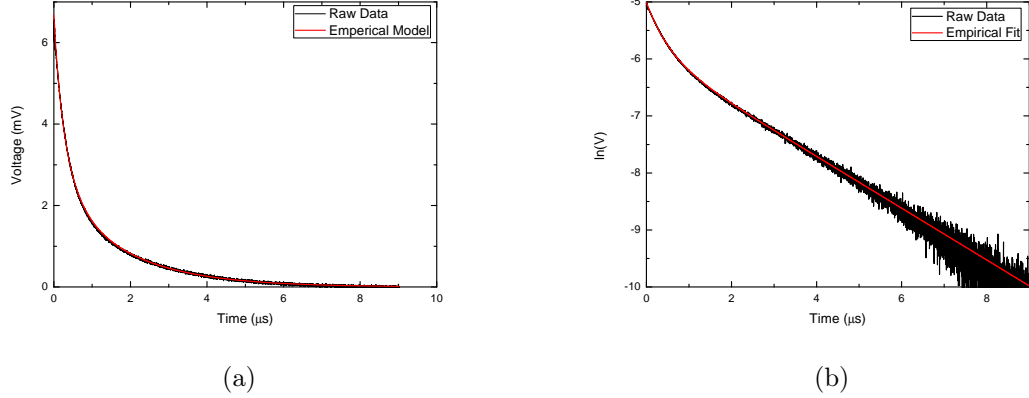


Figure 5.22: (a) shows the empirical fit of equation 5.30 to the raw data with $\tau_1 = 2.2\mu s$ and $\tau_2 = 0.56\mu s$. (b) shows the fit between the natural logarithm of equation 5.30 and the natural logarithm of the raw data.

system behaves when the load resistances are large enough to not allow the non linear behavior of the formation of the electrical double layer. However, when the resistance is small and the formation of the electrical double layer can be seen, the dependence on concentration is reversed as can be seen in figure 5.25. As of now this is not understood.

Now that the behavior of the double layer in equilibrium has been looked at, the formation time of the electrical double layer can be looked at. As mentioned above, this will be done by looking at τ_2 and how it changes with concentration and how it changes with the thickness of the parylene layer on the top plate. The data for the various thicknesses was generally pretty scattered. Like for the Case 2 model, a power law fit can be done on the data to get the time constant as a function of the ion concentration. Figure 5.26 shows the two best data sets that are closest to a power law fit in the form $\tau = ap_0^b$. Table 5.3 shows the fit parameters for all of the top plate samples. Unlike with Case 2 the values are not all that consistent. The fractional errors in a and b are a factor of 3 larger than for Case 2. ($\tau = 0.015 \pm 0.005$) $p_0^{-0.18 \pm 0.03} \mu s$ compared to $\tau = (0.047 \pm 0.005)p_0^{-0.18 \pm 0.01} \mu s$) However, if instead of taking an

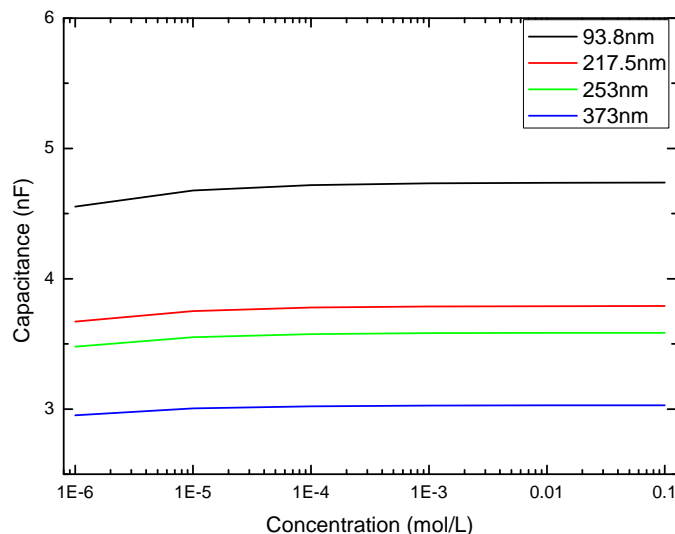


Figure 5.23: Shows the theoretical capacitance of the sample once the electrical double layer has formed. The thickness of the electrical double layer is defined as the Debye length of the system at the concentration used. The dielectric constant of the double layer was $\epsilon_{DoubleLayer} = 20$. This shows a positive trend where increasing the concentration increases the capacitance asymptotically.

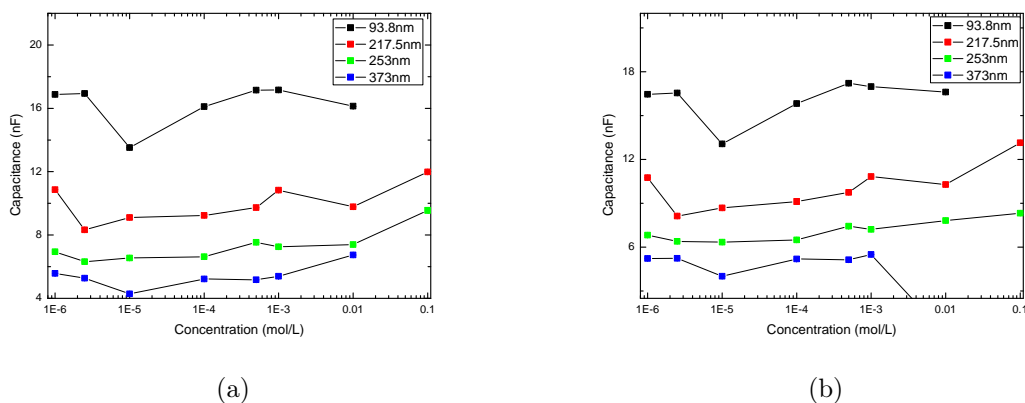


Figure 5.24: (a) Shows the capacitance plotted against the concentration for four different thicknesses with a load resistance of 5000Ω . (b) Shows the same plot with a load resistance of 10000Ω . Both show the same trends as was visible in the plots of the theoretical capacitances. As the concentration increases, both the experimental and theoretical capacitances increase, though they follow different trends. As well, both show the same dependence on the thickness, where as the thickness increases the overall capacitance decreases.

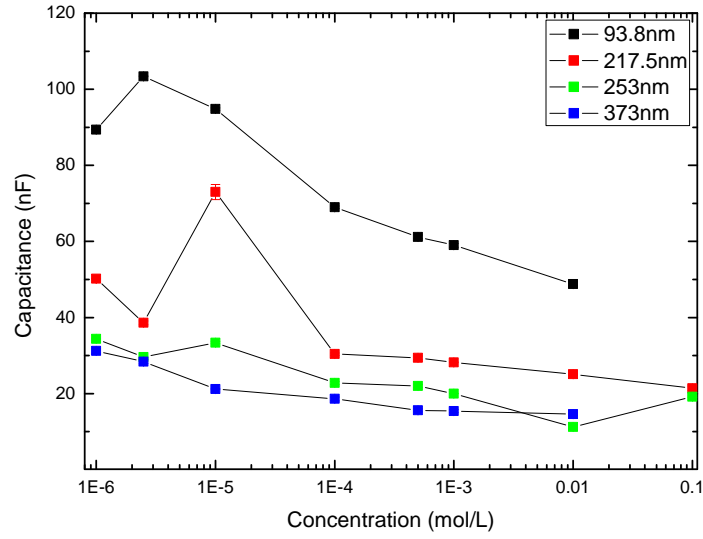


Figure 5.25: Shows the capacitance of the same four samples as they vary with concentration with a load resistance of 50Ω . Unlike for the larger load resistances, the trend is reversed and as the concentration increases the capacitance decreases.

average of all these values to make one equation, if you use each equation and calculate the time constant for a given concentration it can be plotted against the thickness of the top plate parylene layer to see if there is any trend based on thickness. Using a concentration of $p_0 = 0.01\text{mol}/L$, the time constants were be calculated. Figure 5.27 shows a downward trend of the time constant as the thickness of the top plate parylene layer increases for both models. This makes sense, because as the potential drops across the parylene layers which causes a smaller potential difference between the edges of the channel than from the pulse. The thicker layers of parylene cause a larger potential drop, and the double layer forms faster when a smaller potential difference is between the channel. This makes sense physically because with a smaller potential the ions aren't packed as tightly and are able to get to those positions faster, and is supported by the simulation and figure 4.16.

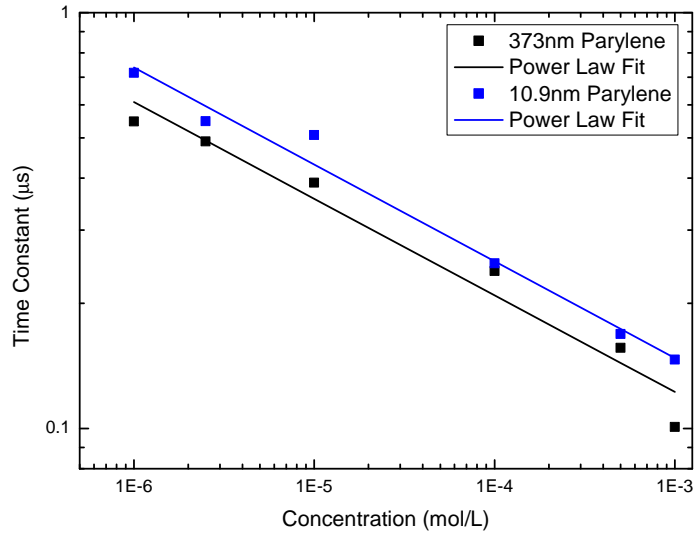


Figure 5.26: Shows the time constant of the empirical model in μs plotted against the concentration in mol/L for the two best data runs, in black with the 373nm thick parylene top plate and in blue the 10.9nm thick parylene top plate. They are plotted on a log log scale so that the linear fit is really a power law fit in the form of $\tau = ap_0^b$ where p_0 is the concentration, τ and a and b are fit parameters. For the 10.9nm top plate $a = 0.0296\mu s$ and $b = -0.2328$. For the 373nm top plate $a = 0.0246\mu s$ and $b = -0.2325$.

Thickness (nm)	a (μs)	b
2.7	0.0436	-0.1974
9.8	0.1484	-0.0414
10.9	0.0296	-0.2328
40.8	0.0627	-0.1293
71.5	0.0209	-0.2513
87	0.1688	-0.0457
93.8	0.0426	-0.1843
217.5	0.0210	-0.2503
253	0.0231	-0.2291
290	0.0406	-0.1809
373	0.0246	-0.2325

Table 5.3: Shows the power law fit parameters for all of the top plate parylene thicknesses. b is the exponent of the concentration and a is the value of τ when $p_0 = 1mol/L$.

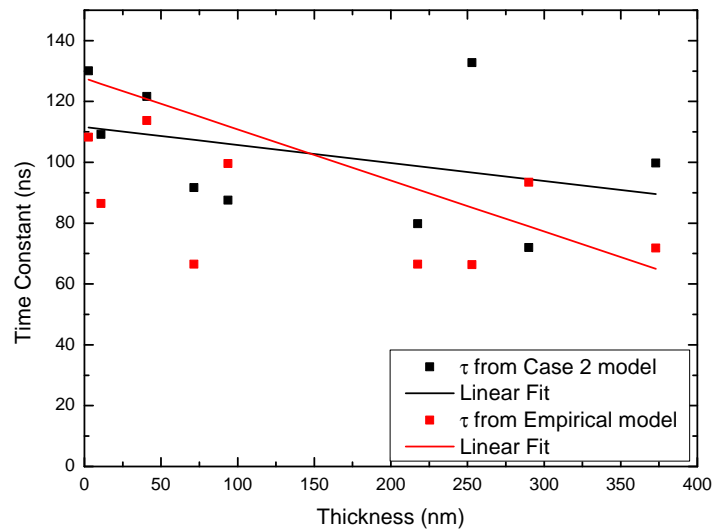


Figure 5.27: Shows the time constant of the double layer formation calculated from the fit parameters for $p_0 = 0.01 \text{ mol/L}$ plotted against the thickness of the parylene layer in the top plate for the model developed in the “Case 2” subsection in black and from the empirical model in red. The solid lines show the best fit trends of the scattered data sets. Both do not fit the data very well, but both show a trend that the double layer forms faster as the thickness increases.

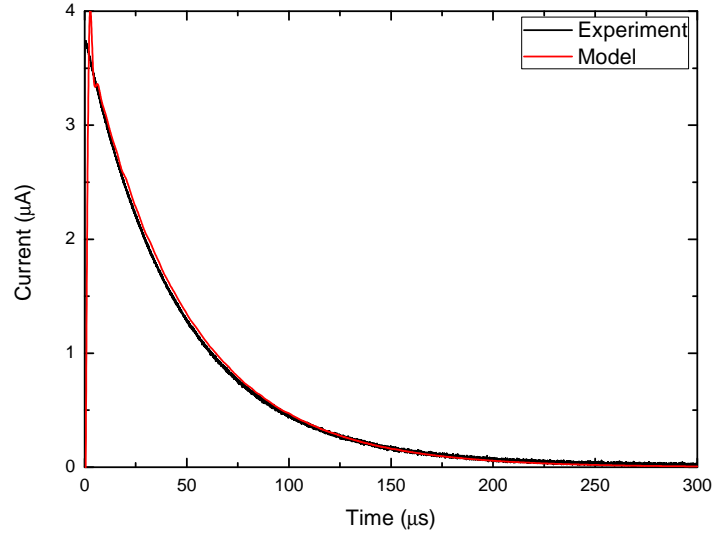


Figure 5.28: Shows the current calculated with the circuit model with an RC time constant defined with equation 5.4 compared against the experimental data. No current from the electrical double layer is included. The parameters used in the experiment and simulation were a load resistance of 5000Ω and a concentration of 0.0001mol/L KCl, as well as a $9\mu\text{m}$ channel thickness in the simulation. The capacitance of the device used (9.43nF) was that from a fit, since the geometric capacitance does not agree with the measured capacitances.

5.5 Comparison with Simulation

Since the attempt to include the external circuit parameters was unsuccessful because the current from the electrical double layer formation was too large, direct comparison between the measured and simulated current is not possible. The experiment was done in two regimes, one where the double layer effects were apparent and the other where they were not. The regime where the double layer effects were not apparent is that with resistance $R \geq 1000\Omega$. The RC time constant is given by equation 5.4. Using a realistic voltage pulse the current can be calculated using

$$I(t) = \frac{V_0(t)}{R_2} e^{-\frac{t}{\tau}}. \quad (5.31)$$

Figure 5.28 shows the comparison of the experimental current and the simple circuit model, showing good agreement. The value of the capacitance used is not the geometric capacitance, but from a fit, so it is not surprising that this fit is quite good. Also, the relationships between the time constants and the current can be compared. From the simulation the power law equation for the time constant is $\tau = 0.8402p_0^{-0.4932}\mu s$ and the range of time constants are from $750\mu s$ for $p_0 = 1 * 10^{-6}mol/L$ to $8.1\mu s$ for $p_0 = 0.01mol/L$. All of the time constants for the experiment are less than $1\mu s$ no matter the concentration. The exponent in the power law fit is much smaller for the experiment and doesn't compare well, but they do both have a trend of decreasing time constants as the concentration increases. Another thing to note about the simulation, is that the double layer time constant is significantly longer than that of the Morrow et al. simulation[6]. For the same potential and concentration the Morrow et al. simulation had time constants over 5 times smaller than calculated in this simulation. Its not surprising that the time constants are different because they are not calculated the same way. Here it is found by finding the time constant of the exponential decay of the current, meaning the time constant is the value of the current when it has decayed to approximately 37% of its maximum. However the Morrow et al. simulation determines the decay time when the simulation is a correlation coefficient of 0.98 between the calculated potential and the potential from the Gouy-Chapman solution. Another difference between the simulations that would cause a difference is the starting ion distributions. Morrow et al. starts with a uniform distribution, and his time constant would be longer if the same initial ion distribution as in this simulation was used.

5.6 Experimental conclusions

The experiment to investigate the dynamics of the electrical double layer was completed using a variety of concentrations ($1 * 10^{-6} mol/L$ to $0.1 mol/L$) for a range of thicknesses of the parylene layer for the top plate. The bottom plate was held constant so only one thickness was used for the bottom parylene layer and one channel depth was used. This experiment found that, although the capacitor model was not right at predicting the actual value of the capacitance of the devices when a double layer was present it predicted the correct trend, for large load resistances (Figures 5.23 and 5.24). For the smaller load resistances, which allowed the probing of the double layer formation, however, the trend as the concentration increased was the opposite of what the capacitor model predicted. (Figure 5.25) The cause of this is unknown, but it is interesting and should be studied in more detail. Lastly, and most importantly, the double layer formation times were investigated. They were found to decrease with concentration (Figure 5.26) and in all cases were less than $1 \mu s$. The power law fit equation from the “Case 2” model had more consistent results and a model based on the physics of the problem rather than being guided by how the data looks. This gives an equation to estimate the electrical double layer time constant which can be used to estimate the frequency of an AC signal used in a microfluidic. Since the time constant found here is from an exponential fit, significant ion movement would occur in one time constant, so the frequency of the AC signal should be much larger than the frequency which has one period as the time constant. To ensure that double layer effects can be ignored $f \gg \frac{1}{\tau}$. Using equation 5.25 this relation becomes

$$f \gg \frac{p_0^{0.15}}{0.047} MHz \quad (5.32)$$

and now a safe estimate for the frequency used in microfluidic devices can be found which is based on experimental evidence.

Chapter 6

Conclusion

The importance of the position of electric charge can not be overstated. Electric charge position has been important in the work of both projects presented in this thesis. This thesis described how a microfluidic parallel plate capacitor was fabricated using mostly standard microfabrication processes, such as sputtering, optical lithography and chemical wet etching, as well as some more novel processes, such as parylene deposition, to create a microfluidic device with blocking electrodes. This device had a bottom plate, which consisted of an electrode deposited inside a microchannel and covered in a layer of parylene and several top plates with different thicknesses of parylene.

The molecular heterojunction structures were made by depositing the first transparent electrode with an electron beam evaporation system. The molecular layer of NAB was deposited with cyclic voltametry and then the insulating layer of SiO_2 and then the top transparent electrode was deposited again with electron beam lithography. All of the fabrication of the molecular junction was done by the McCreery et al.

The experiment on the molecular junction was an exploratory experiment, using the results at wavelengths at 410nm and 532nm applying voltage pulses

from times of $\sim 100ms$ to $\sim 10s$ which showed changes in the absorbance spectrum. These changes were attributed to a physical change in the molecular structure. This suggests that it would be worth looking at faster time scales to see if changes in the optical behavior are seen that can't be attributed to a physical structure change in the molecule. The first experiment done was to look at the electrical characteristics of the samples. This was done by taking an I-V curve by stepping the voltage and measuring the current. An AC voltage dither was also added to measure $\frac{dI}{dV}$.

The rasterscan experiment varied the spatial position of the beam on the sample and found that there was little to no spatial dependence of the signal. This meant the experiment would not be sensitive to slight shifts in the beam position as long as it was maintained in the middle of the active area.

As the frequency and magnitude of the bias were varied it was found that the qualitative behavior of the system was consistent, however quantitative results were not reproducible. The results however suggest that the behavior of the NAB-1 and NAB-4 samples in the frequency range of 500Hz-100kHz and the bias range of 100mV-500mV were the result of the properties of the substrate, and not that of the molecular layer.

After the completion of the study of molecular junctions a flux corrected transport simulation was performed with the same geometry as the electrical double layer experiment to probe the formation time of the electrical double layer. This simulation found a power law fit to the time constant as a function of frequency that is of similar form to the equation for the Debye length, suggesting that the time constant is proportional to the Debye length. However, the experiment, combined with a dielectric model, it was found that the power law fit had a significantly different exponent. The simulation also found a trend that as the magnitude of the input pulse used increased so did the

time constant. This trend was seen in the experimental data as the parylene layer became thicker, hence the voltage between the channel became smaller and therefore the time constant also decreased.

Lastly, the experiment found a range of values of the time constant for the double layer formation, based on the concentration of the solution. This is useful when using electrical detection techniques in microfluidic devices. Equation 5.32 can be used as a guide to find a detection frequency that will allow double layer effects to be avoided based on the ion concentration of the buffer solution being used.

Bibliography

- [1] A. J. Bard and L. R. Faulkner. *Electrochemical Methods: Fundamentals and Applications*. John Wiley and Sons Inc, 2001.
- [2] J. Wu R. L. McCreery and R. P. Kalakodimi. Electron transport and redox reactions in carbon-based molecular electronic junctions. *Physical Chemistry Chemical Physics*, 8:2572–2590, 2006.
- [3] D. J. Thomson G. E. Bridges M. Hedayatipoor S. Olson M. R. Freeman G. A. Ferrier, A. N. Hladio. Microfluidic electromanipulation with capacitive detection for the mechanical analysis of cells. *BIOMICROFLUIDICS*, 2:044102–1, 2008.
- [4] D. J. Thomson G. E. Bridges G. A. Ferrier, S. F. Romanuik and M. R. Freeman. A microwave interferometric system for simultaneous actuation and detection of single biological cells. *Lab on a Chip*, 9:3406–3412, 2009.
- [5] G. A. Ferrier G. E. Bridges M. Butler K. Sunley D. J. Thomson M. Nikolic-Jaric, S. F. Romanuik and M. R. Freeman. Microwave frequency sensors for detection of biological cells in microfluidic channels. *BIOMICROFLUIDICS*, 3:034103–1, 2009.
- [6] D. R. McKenzie R. Morrow and M. M. Bilek. The time-dependent development of electrical double-layers in saline solutions. *Journal of Physics D: Applied Physics*, 39:937–943, 2006.

- [7] M. Kappl H. J. Butt, K. Graf. *Physics and Chemistry of Interfaces*. WILEY-VCH, 2006.
- [8] B. Kirby. *Micro- and Nanoscale Fluid Mechanics Transport in Microfluidic Devices*. Cambridge, 2010.
- [9] R. L. McCreery A. P. Bonifas. In-situ optical absorbance spectroscopy of molecular layers in carbon based molecular electronic devices. *Chem of Mat*, 20:3849–3856, 2008.
- [10] M. A. Swartz A. L. Thangawng, R. S. Ruoff and M. R. Glucksberg. An ultra-thin pdms membrane as a bio/micro-nano interface: fabrication and characterization. *Biomed Microdevices*, 9:587–595, 2007.
- [11] N. Tankovsky and E. Syrakov. Transient ion fluxes, driven by an external electric field in a thin electrolytic cell with blocking electrodes. *Journal of Physics: Condensed Matter*, 17:1225–1238, 2005.
- [12] D. R. Franceschetti and J. R. Macdonald. Numerical analysis of electrical response: Statics and dynamics of space-charge regions at blocking electrodes. *J. Appl. Phys*, 50:291, 1979.
- [13] N. Tankovsky and E. Syrakov. Transient ion dynamics, forced by external electric field in electrolytic cell with blocking electrodes. *Ionics*, 14:525–531, 2008.
- [14] R. Morrow and L. E. Cram. Flux-corrected transport and diffusion on a non-uniform mesh. *Journal of Computational Physics*, 57:129–136, 1985.
- [15] R. Morrow P. Steinle and A. J. Roberts. Use of implicit and explicit flux-corrected transport algorithms in gas discharge problems involving

- non-uniform velocity fields. *Journal of Computational Physics*, 85:493–499, 1989.
- [16] P. Steinle and R. Morrow. An implicit flux-corrected transport algorithm. *Journal of Computational Physics*, 80:61–71, 1989.
- [17] S. T. Zalesak. Fully multidimensional flux-corrected transport algorithms for fluids. *Journal of Computational Physics*, 31:335–362, 1979.
- [18] R. Morrow. The flux-corrected transport method. Unpublished book chapter - personal correspondence.
- [19] R. Morrow. An implicit flux corrected transport method for diffusion or advection dominated problems. Personal correspondence.
- [20] C. W. Gear. *Numerical Initial Value Problems in Ordinary Differential Equations*. Prentice-Hall, 1971.
- [21] W. T. Vetterling, W. H. Press, S. A. Teukolsky and B. P. Flannery. *Numerical Recipes*. Cambridge University Press, 2007.
- [22] L. Lapidus and J. H. Seinfeld. *Numerical Solutions of Ordinary Differential Equations*. Academic Press, 1971.
- [23] R. Morrow and N. Sata. The discharge current induced by the motion of charged particles in time-dependent electric fields; sato's equation extended. *J. Phys. D: Appl. Phys.*, 32:L20–L22, 1999.
- [24] R. M. Lynden-Bell, S. Koneshan, J. C. Rasaiah and S. H. Lee. Solvent structure, dynamics, and ion mobility in aqueous solutions at 25 c. *Journal of Physical Chemistry B*, 102:4193–4204, 1998.

- [25] B. K. Tay Z. J. Han, R. Morrow and D. McKenzie. Time-dependent electrical double layer with blocking electrode. *Applied Physics Letters*, 94:043118–1, 2009.
- [26] D. J. Griffiths. *Introduction to Electrodynamics*. Prentice-Hall, 1999.
- [27] R. Resnick D. Halliday and J. Walker. *Fundamentals of Physics*. Wiley, 2001.
- [28] T. R. Sandin H. D. Young, R. A. Freedman and A. L. Ford. *University Physics*. Addison Wesley, 2000.

Appendix A

FCT C++ Code

```
/******  
This program calculates the current in a microfluidic channel with blocking  
electrodes using a Flux Corrected Transport Algorithm.  
As well as calculating the current it calculates the evolution of the electric  
field, the potential and the positive and negative ion density distributions.  
Steven Olson  
Aug 3 2010  
*****/  
  
#include <iostream>  
#include <conio.h>  
#include <cstdlib>  
#include <fstream>  
#include <math.h>  
#include <algorithm>  
#include <vector>  
#include <gsl/gsl_linalg.h>  
#include <gsl/gsl_vector.h>  
#include <time.h>  
#include <gsl/gsl_statistics.h>  
#include <gsl/gsl_spline.h>  
#define up 7.12e-8 //mobility of positive ions  
#define un -6.88e-8 //mobility of negative ions  
#define Dp 1.83e-9 //diffusion coefficient of positive ions  
#define Dn 1.77e-9 //diffusion coefficient of negative ions  
#define NA 6.02214e23 //Avagadro's number  
#define elec 1.60e-19 //electron charge  
#define Temp 294.0 //Lab temperature
```

```

#define kb 1.38065e-23 //Boltzmann constant
#define co 0.00001 //solution concentration in mol/L
#define dc 9e-6 //depth of the channel
#define ew 80.0 //dielectric constant of water
#define epar 2.65 //dielectric constant of parylene
#define d1 200e-9 //thickness of parylene layer on top plate
#define d2 100e-9 //thickness of the constant parylene layer
#define e0 8.854e-12 //Permittivity of free space
//Defining Poisson's Equation for Runge Kutta Solution
#define gE(x1, x2) (elec/(ew*e0))*(x1-x2)
using namespace std;
int main(){
time_t start, end;
time(&start);
int SAM=5000; //Sampling the ion densities, E-field and Potential after SAM # of time steps
int fc=100, k=0;
int sam_rate=TN/fc;
double A=0.0001; //Area of electrode (1cm x 1cm)
double Vo=0.0100; //magnitude of initial voltage pulse
double R=50;
double C1=43e-9;
double sigma=0;
double Vrc1, Vrc2;
double C=A*ew*e0/dc;
double dV, dx, dy, a, a5, dt, sp, sn, q0, q1, q2, h1, h2, dif, tau;
double b, c, d, a1, a2, a3, a4, k1, k2, k3, k4, f0, f1, B, I1, Vp, I, I2;
double TIME=0;
double r=1, flux_current=10e10, flux_int;
double dtol=1e-7;
int i, j;
double ld=0.304e-9/sqrt(co); //Debye length
double NXD=((dc/ld)*20);
int NX=int (NXD); //number of steps
gsl_vector *gp1 = gsl_vector_alloc(NX+1); //current time step higher order solution vector
gsl_vector *gn1 = gsl_vector_alloc(NX+1); //current time step higher order solution vector
gsl_vector *dp1 = gsl_vector_alloc(NX+1); //higher order matrix main diagonal
gsl_vector *dn1 = gsl_vector_alloc(NX+1); //higher order matrix main diagonal
gsl_vector *ep1 = gsl_vector_alloc(NX); //higher order matrix above diagonal vector
gsl_vector *en1 = gsl_vector_alloc(NX); //higher order matrix above diagonal vector
gsl_vector *fp1 = gsl_vector_alloc(NX); //higher order matrix below diagonal vector
gsl_vector *fn1 = gsl_vector_alloc(NX); //higher order matrix below diagonal vector

```

```

gsl_vector *dp2 = gsl_vector_alloc(NX+1); //lower order matrix main diagonal
gsl_vector *dn2 = gsl_vector_alloc(NX+1); //lower order matrix main diagonal
gsl_vector *ep2 = gsl_vector_alloc(NX); //lower order matrix above diagonal
gsl_vector *en2 = gsl_vector_alloc(NX); //lower order matrix above diagonal
gsl_vector *fp2 = gsl_vector_alloc(NX); //lower order matrix below diagonal
gsl_vector *fn2 = gsl_vector_alloc(NX); //lower order matrix below diagonal
gsl_vector *gp2 = gsl_vector_alloc(NX+1); //current time step lower order solution vector
gsl_vector *gn2 = gsl_vector_alloc(NX+1); //current time step lower order solution vector
gsl_vector *pH = gsl_vector_alloc(NX+1); //Higher order pos ion density solution
gsl_vector *nH = gsl_vector_alloc(NX+1); //higher order neg ion density solution
gsl_vector *x = gsl_vector_alloc(NX+1); //uniform grid vector
gsl_vector *pL = gsl_vector_alloc(NX+1); //Lower order pos ion density solution
gsl_vector *nL = gsl_vector_alloc(NX+1); //Lower order neg ion density solution
gsl_vector *cp = gsl_vector_alloc(NX+2); //Pos courant number
gsl_vector *cn = gsl_vector_alloc(NX+2); //Neg courant number
gsl_vector *wn = gsl_vector_alloc(NX+1); //neg ion velocity
gsl_vector *wp = gsl_vector_alloc(NX+1); //pos ion velocity
gsl_vector *pI = gsl_vector_alloc(NX+1); //initial pos ion density
gsl_vector *nI = gsl_vector_alloc(NX+1); //initial neg ion density
gsl_vector *E = gsl_vector_alloc(NX+1); //Electric field
gsl_vector *V = gsl_vector_alloc(NX+1); //Potential
gsl_vector *PhiHp = gsl_vector_alloc(NX+2); //Higher order pos flux
gsl_vector *PhiHn = gsl_vector_alloc(NX+2); //Higher order neg flux
gsl_vector *PhiLp = gsl_vector_alloc(NX+2); //Lower order pos flux
gsl_vector *PhiLn = gsl_vector_alloc(NX+2); //Lower order neg flux
gsl_vector *ADPhip = gsl_vector_alloc(NX+2); //Pos antidiffusive flux
gsl_vector *ADPhin = gsl_vector_alloc(NX+2); //Neg antidiffusive flux
gsl_vector *CADPhip = gsl_vector_alloc(NX+2); //Corrected antidiffusive flux
gsl_vector *CADPhin = gsl_vector_alloc(NX+2); //Corrected antidiffusive flux
gsl_vector *eE = gsl_vector_alloc(NX); //e for electric field
gsl_vector *fE = gsl_vector_alloc(NX); //f for electric field
gsl_vector *bE = gsl_vector_alloc(NX+1); //b for electric field
gsl_vector *dE = gsl_vector_alloc(NX+1); //ion density infortation for electric field
gsl_vector *diff_E = gsl_vector_alloc(NX);
gsl_vector *sum_E = gsl_vector_alloc(NX);
//gsl_vector *Im = gsl_vector_alloc(NX/10 +1);
vector <double> fluxp, fluxn;
vector <double> Cp, Cn; //Corrector multipliers for pos and neg antidiffusive flux
vector <double> p;
vector <double> n;
vector <double> pa, pb, pmax, pmin;

```

```

vector <double> na, nb, nmax, nmin;
vector <double> Ppp, Qpp, Rpp, Ppm, Qpm, Rpm;
vector <double> Pnp, Qnp, Rnp, Pnm, Qnm, Rnm;
vector <double> Im, xm, Imr, Iml, Ipdr, Indr, IpDif, InDif, Ik;
Cp.resize(NX), Cn.resize(NX), p.resize(NX+1),n.resize(NX+1), pa.resize(NX+1),
pb.resize(NX+1), pmax.resize(NX+1), pmin.resize(NX+1), na.resize(NX+1),
nb.resize(NX+1), nmax.resize(NX+1), nmin.resize(NX+1), Ppp.resize(NX+1),
Qpp.resize(NX+1), Rpp.resize(NX+1), Ppm.resize(NX+1), Qpm.resize(NX+1),
Rpm.resize(NX+1), Pnp.resize(NX+1), Qnp.resize(NX+1), Rnp.resize(NX+1),
Pnm.resize(NX+1), Qnm.resize(NX+1), Rnm.resize(NX+1), fluxp.resize(NX+1),
fluxn.resize(NX+1), Im.resize(NX + 1), xm.resize(NX + 1), Imr.resize(61),
Iml.resize(61), Ipdr.resize(NX+1), Indr.resize(NX+1), IpDif.resize(NX+1),
InDif.resize(NX+1), Ik.resize(NX+1);
ofstream pOut("p.dat"), nOut("n.dat"), fluxpOut("Fluxp.dat"),
fluxnOut("Fluxn.dat"), EOut("E.dat"), VOut("V.dat"),
VgcOut("Vgc.dat"), EgcOut("Egc.dat"), fluxTOut("flux_test.dat"), IOut("I.dat"),
ImOut("Im.dat"), xmOut("xm.dat"), IlbOut("Ilb.dat"), IrbOut("Irb.dat"),
IpdrOut("Ipdr.dat"), IndrOut("Indr.dat"), IpDifOut("IpDif.dat"),
InDifOut("InDif.dat"), IkOut("Ik.dat");
/*****
Reading in Input pulse from file and doing a spline interpolation
*****/

int Nf=10000;
int Ns=4000;
int M=Ns-2000;
double AmpAve[M];
double mean;
double time1[Ns], amp1[Ns];
gsl_vector *time_2 = gsl_vector_alloc(Nf);
gsl_vector *amp = gsl_vector_alloc(Nf);
ifstream inputfile;
inputfile.open ("test2.dat");
for (i=0; i<Nf; i++){
inputfile >> a;
inputfile >> b;
gsl_vector_set(time_2, i, a);
gsl_vector_set(amp, i, b);
}
for (i=0; i<Ns; i++){
time1[i]=gsl_vector_get(time_2, i);
amp1[i]=gsl_vector_get(amp, i);

```

```

}
for (i=0; i<M; i++){
AmpAve[i]=amp1[i+2000];
}
mean = gsl_stats_mean(AmpAve, 1, M);
gsl_interp_accel *acc = gsl_interp_accel_alloc ();
gsl_spline *spline = gsl_spline_alloc (gsl_interp_cspline, Ns);
gsl_spline_init (spline, time1, amp1, Ns);
/*****
Reading in Initial ion densities from files
*****/
ifstream input1, input2;
input1.open("pLinitial.dat");
input2.open("nLinitial.dat");
//for loop generating spatial grid, initial pos and neg ion densities as well
//the initial electric field
dx=dc/NX;
for (i=0; i<=NX; i++){
gsl_vector_set(x, i,dc/2 + (i*dx));
input1 >> h1;
input2 >> h2;
p[i]=h2;
n[i]=h1;
//p[i]=1000*NA*co;
//n[i]=1000*NA*co;
}
input1.close();
input2.close();
/*****
Adding density pulse to propogate
*****/
/*for (i=1000; i<=2000; i++) {
p[i]=p[i]*2;
n[i]=n[i]*2;
}*/
/*****
Starting main time loop
*****/
j=0;
double tau2=2.0e-6;
dt=1.0e-8;

```

```

//while (flux_current>50000000){
while (TIME<1.5e-3){
/*if (TIME<gsl_vector_get(time_2, Ns-1)){
Vo=gsl_spline_eval(spline, TIME, acc);
}
else {
Vo=mean;
}*/
Vo=-mean*(1-exp(-(TIME+1.0e-9)/tau2));
gsl_vector_set(V, 0, Vo);
gsl_vector_set(V, NX, -Vo);
dV=(gsl_vector_get(V, 0)-gsl_vector_get(V, NX)); //potential difference between opposite ends of
the channel
if (j==0){
B=gsl_vector_get(V, NX);
q0=10000;
q1=q0*1.001;
dy=1.0;
while (fabs(dy)>dtol){
gsl_vector_set(E, 0, q0);
for (i=0; i<NX; i++){
k1=gE(p[i],n[i]);
k2=gE(p[i]+0.5*dx*k1, n[i]+0.5*dx*k1);
k3=gE(p[i]+0.5*dx*k2, n[i]+0.5*dx*k2);
k4=gE(p[i]+dx*k3, n[i]+dx*k3);
gsl_vector_set(E, i+1, gsl_vector_get(E, i)+(dx/6.0)*(k1+2.0*k2+
2.0*k3+k4));
gsl_vector_set(V, i+1, gsl_vector_get(V, i)-(dx/6.0)*(3.0*
gsl_vector_get(E, i)+3.0*gsl_vector_get(E, i+1)));
}
f0=gsl_vector_get(V, NX);
gsl_vector_set(E, 0, q1);
for (i=0; i<NX; i++){
k1=gE(p[i],n[i]);
k2=gE(p[i]+0.5*dx*k1, n[i]+0.5*dx*k1);
k3=gE(p[i]+0.5*dx*k2, n[i]+0.5*dx*k2);
k4=gE(p[i]+dx*k3, n[i]+dx*k3);
gsl_vector_set(E, i+1, gsl_vector_get(E, i)+(dx/6.0)*(k1+2.0*k2+
2.0*k3+k4));
gsl_vector_set(V, i+1, gsl_vector_get(V, i)-(dx/6.0)*(3.0*
gsl_vector_get(E, i)+3.0*gsl_vector_get(E, i+1)));

```



```

}
f1=gsl_vector_get(V, NX);
dy=f1-f0;
q2=q1+(B-f1)*(q1-q0)/dy;
q0=q1;
q1=q2;
}
cout<<"dV="<<dV<<endl;
for (i=0; i<=NX; i++){
//gsl_vector_set(E, i, dV/dc);
EOut<<gsl_vector_get(E, i)<<" ";
}
for (i=0; i<NX; i++){
gsl_vector_set(sum_E, i, fabs(gsl_vector_get(E, i))+
fabs(gsl_vector_get(E, i+1)));
}
EOut<<endl;
cout<<"p[1]="<<p[1]<<" p[NX]="<<p[NX]<<" n[1]="<<n[1]<<endl;
cout<<"dt="<<dt<<" & dx="<<dx<<" & ld="<<ld<<" & NX="<<NX<<endl;
TIME = TIME+dt;
cout<<"dt="<<dt<<" & dx="<<dx<<endl;
//Calculating diffusion coefficients
sp=Dp*dt/(pow(dx, 2));
sn=Dn*dt/(pow(dx, 2));
cout<<"s="<<sp<<endl;
}
/*****
Calculating the Initial Courant Numbers
*****/
for (i=0; i<NX; i++){
gsl_vector_set(cp, i+1, up*dt*((gsl_vector_get(E, i)+gsl_vector_get(E, i+1))/(2.0*dx));
gsl_vector_set(cn, i+1, un*dt*((gsl_vector_get(E, i)+gsl_vector_get(E, i+1))/(2.0*dx));
}
gsl_vector_set(cp, 0, 0);
gsl_vector_set(cp, NX+1, 0);
gsl_vector_set(cn, 0, 0);
gsl_vector_set(cn, NX+1, 0);
if (j==0){
cout<<"dt="<<dt<<" & dx="<<dx<<endl;
cout<<"sp="<<sp<<" cp(0)="<<gsl_vector_get(cp, 0)<<" cp(NX+1)="<<gsl_vector_get(cp, NX+1)<<endl;
}

```

```

/* *****
calculating matrix elements for the Higher Order solution.
The main diagonals, dp, dn, the upper diagonals ep, en and the lower
diagonals fp and fn. These elements definethe tridiagonal matrix.
gp and gn define the column vector in the equation A*p=g.
***** /
/*****
Positive Ion Density for Higher Order Solution
***** /
//Calculating ep1 = c which forms the upper diagonal of A
for (i=0; i<NX; i++){
a= 2.0+(3.0*gsl_vector_get(cp, i+1))+pow(gsl_vector_get(cp, i+1), 2)
-6.0*sp;
gsl_vector_set(ep1, i, a);
}
//Calculating fp1=a which forms the lower diagonal of A
for (i=0; i<NX; i++){
a=2.0-(3.0*gsl_vector_get(cp, i+1))+pow(gsl_vector_get(cp, i+1), 2)-
6.0*sp;
gsl_vector_set(fp1, i, a);
}
//calculating dp1[0] and dp1[NX] of the main diagonal of A
gsl_vector_set(dp1, 0, 8.0+(3*(gsl_vector_get(cp, 1)-gsl_vector_get(cp, 0)))-
pow(gsl_vector_get(cp, 1), 2)-pow(gsl_vector_get(cp, 0), 2)+(6.0*sp));
gsl_vector_set(dp1, NX, 8.0+(3*(gsl_vector_get(cp, NX+1)-gsl_vector_get(cp, NX)))-
pow(gsl_vector_get(cp, NX), 2)-pow(gsl_vector_get(cp, NX+1), 2)+(6.0*sp));
//Calculating dp1[i] = b for 0<i<NX of the main diagonal of A
for (i=1; i<NX; i++){
a=8.0+(3.0*(gsl_vector_get(cp, i+1)-gsl_vector_get(cp, i)))-
(pow(gsl_vector_get(cp, i+1), 2)+pow(gsl_vector_get(cp, i), 2))+
12.0*sp;
gsl_vector_set(dp1, i, a);
}
//Calculating gp1[0] of the vector g in the equation A*p=g
a=(8.0 - (3.0*(gsl_vector_get(cp, 1)-gsl_vector_get(cp, 0)))-
(pow(gsl_vector_get(cp, 1), 2)+pow(gsl_vector_get(cp, 0), 2))-
(6.0*sp))*p[0]+(2.0-(3.0*gsl_vector_get(cp, 1))+
pow(gsl_vector_get(cp, 1), 2)+(6.0*sp))*p[1];
gsl_vector_set(gp1, 0, a);
//calculating gp1[NX] of the vector g in the equation A*p=g
a=(2.0+(3.0*gsl_vector_get(cp, NX))+pow(gsl_vector_get(cp, NX), 2)+

```

```

6.0*sp)*p[NX-1]+(8.0-(3.0*(gsl_vector_get(cp, NX+1)-
gsl_vector_get(cp, NX)))-pow(gsl_vector_get(cp, NX), 2)-
pow(gsl_vector_get(cp, NX+1), 2)-(6.0*sp))*p[NX];
gsl_vector_set(gp1, NX, a);
//Calculating gp1[i] for 0<i<NX of the vector g in the equation A*p=g
for (i=1; i<NX; i++){
a=(2.0+(3.0*gsl_vector_get(cp, i))+pow(gsl_vector_get(cp, i), 2)+
(6.0*sp))*p[i-1]+(8.0-(3.0*(gsl_vector_get(cp, i+1)-
gsl_vector_get(cp, i)))-pow(gsl_vector_get(cp, i+1), 2)+
pow(gsl_vector_get(cp, i), 2)-(12.0*sp))*p[i]+
(2.0-(3.0*gsl_vector_get(cp, i+1))+pow(gsl_vector_get(cp, i+1), 2)
+(6.0*sp))*p[i+1];
gsl_vector_set(gp1, i, a);
}
/*****
Negative Ion Density for Higher Order Solution
*****/
//Calculating en1 = c which forms the upper diagonal of A
for (i=0; i<NX; i++){
a= 2.0+(3.0*gsl_vector_get(cn, i+1))+pow(gsl_vector_get(cn, i+1), 2)
-6.0*sn;
gsl_vector_set(en1, i, a);
}
//Calculating fn1=a which forms the lower diagonal of A
for (i=0; i<NX; i++){
a=2.0-(3.0*gsl_vector_get(cn, i+1))+pow(gsl_vector_get(cn, i+1), 2)-
6.0*sn;
gsl_vector_set(fn1, i, a);
}
//calculating dn1[0] and dn1[NX] of the main diagonal of A
gsl_vector_set(dn1, 0, 8.0+(3*(gsl_vector_get(cn, 1)-
gsl_vector_get(cn, 0)))-pow(gsl_vector_get(cn, 1), 2)-
pow(gsl_vector_get(cn, 0), 2)+(6.0*sn));
gsl_vector_set(dn1, NX, 8.0+(3*(gsl_vector_get(cn, NX+1)-
gsl_vector_get(cn, NX)))-pow(gsl_vector_get(cn, NX), 2)-
pow(gsl_vector_get(cn, NX+1), 2)+(6.0*sn));
//Calculating dn1[i] = b for 0<i<NX of the main diagonal of A
for (i=1; i<NX; i++){
a=8.0+(3.0*(gsl_vector_get(cn, i+1)-gsl_vector_get(cn, i)))-
(pow(gsl_vector_get(cn, i+1), 2)+pow(gsl_vector_get(cn, i), 2))+
12.0*sn;

```

```

gsl_vector_set(dn1, i, a);
}
//Calculating gn1[0] of the vector g in the equation A*p=g
a=(8.0-(3.0*(gsl_vector_get(cn, 1)-gsl_vector_get(cn, 0)))-
(pow(gsl_vector_get(cn, 1), 2)+pow(gsl_vector_get(cn, 0), 2))-
(6.0*sn))*n[0]+(2.0-(3.0*gsl_vector_get(cn, 1))+
pow(gsl_vector_get(cn, 1), 2)+(6.0*sn))*n[1];
gsl_vector_set(gn1, 0, a);
//calculating gn1[NX] of the vector g in the equation A*p=g
a=(2.0+(3.0*gsl_vector_get(cn, NX))+pow(gsl_vector_get(cn, NX), 2)+
6.0*sn)*n[NX-1]+(8.0-(3.0*(gsl_vector_get(cn, NX+1)-
gsl_vector_get(cn, NX)))-pow(gsl_vector_get(cn, NX), 2)-
pow(gsl_vector_get(cn, NX+1), 2)-(6.0*sn))*n[NX];
gsl_vector_set(gn1, NX, a);
//Calculating gn1[i] for 0<i<NX of the vector g in the equation A*p=g
for (i=1; i<NX; i++){
a=(2.0+(3.0*gsl_vector_get(cn, i))+pow(gsl_vector_get(cn, i), 2)+
(6.0*sn))*n[i-1]+(8.0-(3.0*(gsl_vector_get(cn, i+1)-
gsl_vector_get(cn, i)))-pow(gsl_vector_get(cn, i+1), 2)+
pow(gsl_vector_get(cn, i), 2)-(12.0*sn))*n[i]+
(2.0-(3.0*gsl_vector_get(cn, i+1))+pow(gsl_vector_get(cn, i+1), 2)
+(6.0*sn))*n[i+1];
gsl_vector_set(gn1, i, a);
}
//Solving tridiagonal systems with Scientific Library Solver
gsl_linalg_solve_tridiag(dp1, ep1, fp1, gp1, pH);
gsl_linalg_solve_tridiag(dn1, en1, fn1, gn1, nH);
/*****
Calculating Positive Ion Densities for Lower Order Scheme
*****/
//calculating gp2[0]
a=-((gsl_vector_get(cp, 1)-fabs(gsl_vector_get(cp, 1))))*p[1]+
(2+(gsl_vector_get(cp, 0)-fabs(gsl_vector_get(cp, 0)))-
(gsl_vector_get(cp, 1)+fabs(gsl_vector_get(cp, 1))))*p[0];
gsl_vector_set(gp2, 0, a);
//calculating gp2[NX]
a=((gsl_vector_get(cp, NX)+fabs(gsl_vector_get(cp, NX)))*p[NX-1]+
(2+(gsl_vector_get(cp, NX)-fabs(gsl_vector_get(cp, NX)))-
(gsl_vector_get(cp, NX+1)+fabs(gsl_vector_get(cp, NX+1))))*p[NX];
gsl_vector_set(gp2, NX, a);
//calculating dp2[i] for 1<=i<=NX

```

```

for (i=1; i<NX; i++){
a=(2.0+(4.0*sp));
gsl_vector_set(dp2, i, a);
}
//Setting dp2[0]=1-fp2[1] and dp2[NX]=1-ep2{NX-1}
gsl_vector_set(dp2, 0, 2.0+(2.0*sp));
gsl_vector_set(dp2, NX, 2.0+(2.0*sp));
//calculating ep2[i] and fp2[i] for all i
for (i=0; i<NX; i++){
a=-2.0*sp;
gsl_vector_set(ep2, i, a);
gsl_vector_set(fp2, i, a);
}
//calculating gp2[i] for all i except i=0 and i=NX
for (i=1; i<NX; i++){
a1=(gsl_vector_get(cp, i)+fabs(gsl_vector_get(cp, i)));
a2=(2.0+(gsl_vector_get(cp, i)-fabs(gsl_vector_get(cp, i)))-
(gsl_vector_get(cp, i+1)+fabs(gsl_vector_get(cp, i+1))));
a3=(gsl_vector_get(cp, i+1)-fabs(gsl_vector_get(cp, i+1)));
a=(a1*p[i-1])+(a2*p[i])-(a3*p[i+1]);
gsl_vector_set(gp2, i, a);
}
/*****
calculating the negative ion solutions with the lower order scheme
*****/
//calculating gn2[0]
a=-((gsl_vector_get(cn, 1)-fabs(gsl_vector_get(cn, 1))))*n[1]+
(2+(gsl_vector_get(cn, 0)-fabs(gsl_vector_get(cn, 0)))-
(gsl_vector_get(cn, 1)+fabs(gsl_vector_get(cn, 1))))*n[0];
gsl_vector_set(gn2, 0, a);
//calculating gn2[NX]
a=((gsl_vector_get(cn, NX)+fabs(gsl_vector_get(cn, NX))))*n[NX-1]+
(2+(gsl_vector_get(cn, NX)-fabs(gsl_vector_get(cn, NX)))-
(gsl_vector_get(cn, NX+1)+fabs(gsl_vector_get(cn, NX+1))))*n[NX];
gsl_vector_set(gn2, NX, a);
//calculating dn2[i] for 1<=i<=NX
for (i=1; i<NX; i++){
a=(2.0+(4.0*sn));
gsl_vector_set(dn2, i, a);
}
//Setting dn2[0]=1-fn2[1] and dn2[NX]=1-en2{NX-1}

```

```

gsl_vector_set(dn2, 0, 2.0+(2.0*sn));
gsl_vector_set(dn2, NX, 2.0+(2.0*sn));
//calculating en2[i] and fn2[i] for all i
for (i=0; i<NX; i++){
a=-2.0*sn;
gsl_vector_set(en2, i, a);
gsl_vector_set(fn2, i, a);
}
//calculating gn2[i] for all i except i=0 and i=NX
for (i=1; i<NX; i++){
a1=(gsl_vector_get(cn, i)+fabs(gsl_vector_get(cn, i)));
a2=(2.0+(gsl_vector_get(cn, i)-fabs(gsl_vector_get(cn, i)))-
(gsl_vector_get(cn, i+1)+fabs(gsl_vector_get(cn, i+1))));
a3=(gsl_vector_get(cn, i+1)-fabs(gsl_vector_get(cn, i+1)));
a=(a1*n[i-1])+(a2*n[i])-(a3*n[i+1]);
gsl_vector_set(gn2, i, a);
}
//solving the tridiagonal matrix for the lower order scheme
gsl_linalg_solve_symm_tridiag(dp2, ep2, gp2, pL);
gsl_linalg_solve_symm_tridiag(dn2, en2, gn2, nL);
/*****
calculating the flux's for pos and neg ions for the higher order scheme
*****/
for (i=1; i<=NX; i++){
//Pos Higher Order Ion Flux
a=(dx/12.0)*(2.0+(pow(gsl_vector_get(cp, i), 2)*
(gsl_vector_get(pH,i)-gsl_vector_get(pH, i-1)-p[i]+p[i-1]))+
(3.0*gsl_vector_get(cp, i)*(gsl_vector_get(pH, i)+
gsl_vector_get(pH, i-1)+p[i]+p[i-1]))-(6.0*sp*
(gsl_vector_get(pH, i)-gsl_vector_get(pH, i-1)+p[i]-p[i-1]))));
gsl_vector_set(PhiHp, i, a);
//Neg Higher Order Ion Flux
a=(dx/12.0)*(2.0+(pow(gsl_vector_get(cn, i), 2)*
(gsl_vector_get(nH,i)-gsl_vector_get(nH, i-1)-n[i]+n[i-1]))+
(3.0*gsl_vector_get(cn, i)*(gsl_vector_get(nH, i)+
gsl_vector_get(nH, i-1)+n[i]+n[i-1]))-(6.0*sn*
(gsl_vector_get(nH, i)-gsl_vector_get(nH, i-1)+n[i]-n[i-1]))));
gsl_vector_set(PhiHn, i, a);
}
gsl_vector_set(PhiHp, 0, 0);
gsl_vector_set(PhiHp, NX+1, 0);

```

```

gsl_vector_set(PhiHn, 0, 0);
gsl_vector_set(PhiHn, NX+1, 0);
/*****
calculating the flux's for pos and neg ions for the lower order scheme
*****/
for (i=1; i<=NX; i++){
//Pos Lower order ion flux
a=(dx/2.0)*((gsl_vector_get(cp, i)+fabs(gsl_vector_get(cp, i)))*
p[i-1]+(gsl_vector_get(cp, i)-fabs(gsl_vector_get(cp, i)))*p[i]-
(2.0*sp*(gsl_vector_get(pL, i)-gsl_vector_get(pL, i-1))));
gsl_vector_set(PhiLp, i, a);
//Neg Lower Order ion flux
a=(dx/2.0)*((gsl_vector_get(cn, i)+fabs(gsl_vector_get(cn, i)))*
n[i-1]+(gsl_vector_get(cn, i)-fabs(gsl_vector_get(cn, i)))*n[i]-
(2.0*sn*(gsl_vector_get(nL, i)-gsl_vector_get(nL, i-1))));
gsl_vector_set(PhiLn, i, a);
}
gsl_vector_set(PhiLp, 0, 0);
gsl_vector_set(PhiLp, NX+1, 0);
gsl_vector_set(PhiLn, 0, 0);
gsl_vector_set(PhiLn, NX+1, 0);
/*calculating the anti diffusive flux before any correction is applied */
for(i=0; i<=NX+1; i++){
a=gsl_vector_get(PhiHp, i)-gsl_vector_get(PhiLp, i);
gsl_vector_set(ADPhip, i, a);
a=gsl_vector_get(PhiHn, i)-gsl_vector_get(PhiLn, i);
gsl_vector_set(ADPhin, i, a);
}
/*****
Starting Zalesak's flux limiting procedure
*****/
/*Checking conditions on Antidiffusive flux's for p and n for Zalesak's
scheme*/
for (i=0; i<NX; i++){
b=gsl_vector_get(ADPhip, i+1)*(gsl_vector_get(pL, i+1)-gsl_vector_get(pL, i));
if(i==0){
c=gsl_vector_get(ADPhip, i+1)*(gsl_vector_get(pL, i+2)-gsl_vector_get(pL, i+1));
d=gsl_vector_get(ADPhip, i+1)*gsl_vector_get(pL, i);
}
else if(i>NX-2){
d=gsl_vector_get(ADPhip, i+1)*(gsl_vector_get(pL, i)-gsl_vector_get(pL, i-1));

```

```

c=0;
}
else{
c=gsl_vector_get(ADPhip, i+1)*(gsl_vector_get(pL, i+2)-gsl_vector_get(pL, i+1));
d=gsl_vector_get(ADPhip, i+1)*(gsl_vector_get(pL, i)-gsl_vector_get(pL, i-1));
}
if(b<0&&(c<0||d<0)){
gsl_vector_set(ADPhip, i, 0);
}
b=gsl_vector_get(ADPhin, i+1)*(gsl_vector_get(nL, i+1)-gsl_vector_get(nL, i));
if(i==0){
c=gsl_vector_get(ADPhin, i+1)*(gsl_vector_get(nL, i+2)-gsl_vector_get(nL, i+1));
d=gsl_vector_get(ADPhin, i+1)*gsl_vector_get(nL, i);
}
else if(i>NX-2){
d=gsl_vector_get(ADPhin, i+1)*(gsl_vector_get(nL, i)-gsl_vector_get(nL, i-1));
c=0;
}
else{
c=gsl_vector_get(ADPhin, i+1)*(gsl_vector_get(nL, i+2)-gsl_vector_get(nL, i+1));
d=gsl_vector_get(ADPhin, i+1)*(gsl_vector_get(nL, i)-gsl_vector_get(nL, i-1));
}
if(b<0&&(c<0||d<0)){
gsl_vector_set(ADPhin, i+1, 0);
}
}
}
/*****
calculating pa, pb, pmin, pmax, na, nb, nmin, nmax for Zalesak's Limiter
method
*****/
for (i=1; i<NX; i++){
pmax[i]=max(max(p[i-1], p[i]), max(max(p[i+1], gsl_vector_get(pL, i-1)),
max(gsl_vector_get(pL, i), gsl_vector_get(pL, i+1))));
pmin[i]=min(min(p[i-1], p[i]), min(min(p[i+1], gsl_vector_get(pL, i-1)),
min(gsl_vector_get(pL, i), gsl_vector_get(pL, i+1))));
nmax[i]=max(max(n[i-1], n[i]), max(max(n[i+1], gsl_vector_get(nL, i-1)),
max(gsl_vector_get(nL, i), gsl_vector_get(nL, i+1))));
nmin[i]=min(min(n[i-1], n[i]), min(min(n[i+1], gsl_vector_get(nL, i-1)),
min(gsl_vector_get(nL, i), gsl_vector_get(nL, i+1))));
}
pmax[0]=max(max(p[0], p[1]), max(gsl_vector_get(pL, 0), gsl_vector_get(pL, 1)));

```



```

pmax[NX]=max(max(p[NX-1], p[NX]), max(gsl_vector_get(pL, NX-1), gsl_vector_get(pL, NX)));
pmin[0]=min(min(p[0], p[1]), min(gsl_vector_get(pL, 0), gsl_vector_get(pL, 1)));
pmin[NX]=min(min(p[NX-1], p[NX]), min(gsl_vector_get(pL, NX-1), gsl_vector_get(pL, NX)));
nmax[0]=max(max(n[0], n[1]), max(gsl_vector_get(nL, 0), gsl_vector_get(nL, 1)));
nmax[NX]=max(max(n[NX-1], n[NX]), max(gsl_vector_get(nL, NX-1), gsl_vector_get(nL, NX)));
nmin[0]=min(min(n[0], n[1]), min(gsl_vector_get(nL, 0), gsl_vector_get(nL, 1)));
nmin[NX]=min(min(n[NX-1], n[NX]), min(gsl_vector_get(nL, NX-1), gsl_vector_get(nL, NX)));
for (i=0; i<=NX; i++){
Ppp[i]=max(0.0, gsl_vector_get(ADPhip, i))-min(0.0, gsl_vector_get(ADPhip, i+1));
Ppm[i]=max(0.0, gsl_vector_get(ADPhip, i+1))-min(0.0, gsl_vector_get(ADPhip, i));
Pnp[i]=max(0.0, gsl_vector_get(ADPhin, i))-min(0.0, gsl_vector_get(ADPhin, i+1));
Pnm[i]=max(0.0, gsl_vector_get(ADPhin, i+1))-min(0.0, gsl_vector_get(ADPhin, i));
}
for(i=0; i<=NX; i++){
Qpp[i]=(pmax[i]-gsl_vector_get(pL, i))*dx;
Qpm[i]=(gsl_vector_get(pL, i)-pmin[i])*dx;
Qnp[i]=(nmax[i]-gsl_vector_get(nL, i))*dx;
Qnm[i]=(gsl_vector_get(nL, i)-nmin[i])*dx;
}
for(i=0; i<=NX; i++){
//Calculating Rpp
if(Ppp[i]>0){
Rpp[i]=min(1.0, Qpp[i]/Ppp[i]);
}
else if (Ppp[i]==0){
Rpp[i]=0.0;
}
//Calculating Rpm
if(Ppm[i]>0){
Rpm[i]=min(1.0, Qpm[i]/Ppm[i]);
}
else if (Ppm[i]==0){
Rpm[i]=0.0;
}
//Calculating Rnp
if(Pnp[i]>0){
Rnp[i]=min(1.0, Qnp[i]/Pnp[i]);
}
else if(Pnp[i]==0){
Rnp[i]=0.0;
}
}

```

```

//Calculating Rnm
if(Pnm[i]>0){
Rnm[i]=min(0.0, Qnm[i]/Pnm[i]);
}
else if(Pnm[i]==0){
Rnm[i]=0.0;
}
}

/*calculating the positive and negative corrector multipliers to multiply
with the antidiffusive flux to get the corrected, limited antidiffusive
flux */
Cp[0]=0;
Cp[NX+1]=0;
Cn[0]=0;
Cn[NX+1]=0;
for (i=1; i<=NX; i++){
//Calculating Corrector Multiplier for positive antidiffusive flux
if(gsl_vector_get(ADPhip, i)>=0){
Cp[i]=min(Rpp[i], Rpm[i-1]);
}
else{
Cp[i]=min(Rpp[i-1], Rpm[i]);
}
//Calculating Corrector Multiplier for negative antidiffusive flux
if(gsl_vector_get(ADPhin, i)>=0){
Cn[i]=min(Rnp[i], Rnm[i-1]);
}
else{
Cn[i]=min(Rnp[i-1], Rnm[i]);
}
}
}

//calculating the corrected antidiffusive flux
for(i=0; i<=NX+1; i++){
gsl_vector_set(CADPhip, i, Cp[i]*gsl_vector_get(ADPhip, i));
gsl_vector_set(CADPhin, i, Cn[i]*gsl_vector_get(ADPhin, i));
}

/* calculating the flux corrected ion densities */
for (i=0; i<=NX; i++){
p[i]=gsl_vector_get(pL, i)+(gsl_vector_get(CADPhip, i)-gsl_vector_get(CADPhip, i+1))/dx;
n[i]=gsl_vector_get(nL, i)+(gsl_vector_get(CADPhin, i)-gsl_vector_get(CADPhin, i+1))/dx;
}
}

```

```

/*****
Calculate Flux for Pos and Neg ions
*****/

for (i=0; i<=NX; i++){
if (i<=NX/2){
fluxp[i]=(up*p[i]*gsl_vector_get(E, i)-((Dp/dx)*(p[i+1]-p[i]));
fluxn[i]=(un*n[i]*gsl_vector_get(E, i)-((Dn/dx)*(n[i+1]-n[i]));
}
else {
fluxp[i]=(up*p[i]*gsl_vector_get(E, i)-((Dp/dx)*(p[i]-p[i-1]));
fluxn[i]=(un*n[i]*gsl_vector_get(E, i)-((Dn/dx)*(n[i]-n[i-1]));
}
}
if (j<10000){
flux_current=10e10;
}
else {
flux_current=fluxp[NX/2];
}
/*****
Calculating Electric field based on ion redistribution
*****/
/*****
Setting Vp to the potential at the left boundary from the previous time
to be used in the current calculation*****/
/*Calculating E with 4th Order Runge Kutta, and V with Simpson's rule
combing with the shooting method */
a4=0;
B=gsl_vector_get(V, NX);
q0=gsl_vector_get(E, 0);
q1=q0*1.001;
dy=1.0;
while (fabs(dy)>dtol){
gsl_vector_set(E, 0, q0);
for (i=0; i<NX; i++){
k1=gE(p[i],n[i]);
k2=gE(p[i]+0.5*dx*k1, n[i]+0.5*dx*k1);
k3=gE(p[i]+0.5*dx*k2, n[i]+0.5*dx*k2);
k4=gE(p[i]+dx*k3, n[i]+dx*k3);
gsl_vector_set(E, i+1, gsl_vector_get(E, i)+(dx/6.0)*(k1+2.0*k2+
2.0*k3+k4));

```

```

gsl_vector_set(V, i+1, gsl_vector_get(V, i)-(dx/6.0)*(3.0*
gsl_vector_get(E, i)+3.0*gsl_vector_get(E, i+1)));
}
f0=gsl_vector_get(V, NX);
gsl_vector_set(E, 0, q1);
for (i=0; i<NX; i++){
k1=gE(p[i],n[i]);
k2=gE(p[i]+0.5*dx*k1, n[i]+0.5*dx*k1);
k3=gE(p[i]+0.5*dx*k2, n[i]+0.5*dx*k2);
k4=gE(p[i]+dx*k3, n[i]+dx*k3);
gsl_vector_set(E, i+1, gsl_vector_get(E, i)+(dx/6.0)*(k1+2.0*k2+
2.0*k3+k4));
gsl_vector_set(V, i+1, gsl_vector_get(V, i)-(dx/6.0)*(3.0*
gsl_vector_get(E, i)+3.0*gsl_vector_get(E, i+1)));
}
f1=gsl_vector_get(V, NX);
dy=f1-f0;
q2=q1+(B-f1)*(q1-q0)/dy;
q0=q1;
q1=q2;
}
/*****
Calculating the non Faradiac current
*****/
I1=0;
for (i=0; i<NX; i++){
I1=I1+(((p[i]+p[i+1])*gsl_vector_get(cp, i+1)*dx/(2.0*dt))-((n[i]+n[i+1])*
gsl_vector_get(cn, i+1)*dx/(2.0*dt))-((Dp/dx)*(p[i+1]-p[i]))+
((Dn/dx)*(n[i+1]-n[i])))*dx;
}
for (i=0; i<NX; i++){
Ipdri[i]=up*p[i]*gsl_vector_get(E, i);
Indri[i]=un*n[i]*gsl_vector_get(E, i);
if (i>0&& i<NX){
IpDif[i]=Dp*(p[i+1]-p[i-1])/(2.0*dx);
InDif[i]=Dn*(n[i+1]-n[i-1])/(2.0*dx);
}
else if (i==0){
IpDif[i]=Dp*(p[i+1]-p[i])/dx;
InDif[i]=Dn*(n[i+1]-n[i])/dx;
}
}

```

```

else {
IpDif[i]=Dp*(p[i]-p[i-1])/dx;
InDif[i]=Dn*(n[i]-n[i-1])/dx;
}
if (i<100||i>NX-100){
IpdrOut<<Ipdr[i]<<" ";
IndrOut<<Indr[i]<<" ";
IpDifOut<<IpDif[i]<<" ";
InDifOut<<InDif[i]<<" ";
}
}
for (i=0; i<=NX; i++){
Ik[i]=A*elec*(Ipdr[i]-Indr[i]
-IpDif[i]+InDif[i]);
if (i%40==0){
IkOut<<Ik[i]<<" ";
}
else if (i==NX){
IkOut<<Ik[i]<<" ";
}
}
I2=0;
for (i=0; i<=NX; i++){
I2 = I2+Ik[i]*dx/dc;
}
IkOut<<endl;
IpdrOut<<endl;
IndrOut<<endl;
IpDifOut<<endl;
InDifOut<<endl;
I=((A/(dc))*((elec*I1))+((mean/50)*exp(-TIME/tau2)));
/*****
Calculating the size of the next time step
*****/
for (i=0; i<NX; i++){
gsl_vector_set(diff_E, i, fabs(gsl_vector_get(E, i))+
fabs(gsl_vector_get(E, i+1)));
}
if (p[0]>1.01*p[NX/2]){
dt=5.0e-8;
}

```

```

else {
a5=0.9*dx/(up*fabs(gsl_vector_max(sum_E)));
//dt=a5;
//dt=5.0e-7;
if (a5<1e-7){
dt=a5;
}
else {
dt=0.1e-7;
}
}
TIME=TIME+dt;
sp=Dp*dt/(pow(dx, 2));
sn=Dn*dt/(pow(dx, 2));
IOut<<TIME<<" " <<I<<" " <<gsl_vector_get(V, 0)<<" " <<(A/(dc))*((elec*I1))
<<" " <<((mean/50)*exp(-TIME/tau2)) <<" "
<<((A*ew*e0/(dc*dt))*(gsl_vector_get(V, 0)-Vp-Vrc2+Vrc1)
<<" " <<(gsl_vector_get(V, 0)-Vrc2)/R<<" " <<(A/(dc))*(elec*I1)+((mean/50)*exp(-TIME/tau2))<<"
"<<dt<<" " <<I2<<endl;
//Re-Calculating the Courant Numbers with the new Electric field
for (i=0; i<NX; i++){
gsl_vector_set(cp, i+1, up*dt*((gsl_vector_get(E, i)+gsl_vector_get(E, i+1))/(2.0*dx));
gsl_vector_set(cn, i+1, un*dt*((gsl_vector_get(E, i)+gsl_vector_get(E, i+1))/(2.0*dx));
}
gsl_vector_set(cp, 0, 0);
gsl_vector_set(cp, NX+1, 0);
gsl_vector_set(cn, 0, 0);
gsl_vector_set(cn, NX+1, 0);
fluxTOut<<fluxp[NX/2]<<endl;
if (j%SAM==0){
cout<<"j="<<j<<" ";
for (i=0; i<=NX; i++){
VOut<<gsl_vector_get(V, i)<<" ";
EOut<<gsl_vector_get(E, i)<<" ";
pOut<<p[i]<<" ";
nOut<<n[i]<<" ";
fluxpOut<<fluxp[i]<<" ";
}
}
else if (j==TN){
for (i=0; i<=NX; i++){

```

```

VOut<<gsl_vector_get(V, i)<<" ";
EOut<<gsl_vector_get(E, i)<<" ";
pOut<<p[i]<<" ";
nOut<<n[i]<<" ";
fluxpOut<<fluxp[i]<<" ";
}
}
VOut<<endl;
EOut<<endl;
pOut<<endl;
nOut<<endl;
fluxpOut<<endl;
j++;
/*****
Ending Time Loop
*****/
}
/*****
Calculating Guoy Chapman solution
*****/
double gamma, kappa, po;
vector <double> Vgc;
vector <double> Egc;
Vgc.resize(NX/2);
Egc.resize(NX/2);
gamma=tanh((elec*gsl_vector_get(V, 0))/(4*kb*Temp));
kappa=sqrt(co)/(0.304e-9);
po=pow(kappa, 2)*ew*e0*kb*Temp/(2.0*pow(elec, 2));
for (i=0; i<NX/2; i++){
Vgc[i]=(2.0*kb*Temp/elec)*log((1+gamma*exp(-kappa*(gsl_vector_get(x, i)+
gsl_vector_get(x, NX)))/(1-gamma*exp(-kappa*(gsl_vector_get(x, i)+
gsl_vector_get(x, NX))));
VgcOut<<Vgc[i]<<" ";
Egc[i]=sqrt(8.0*po*kb*Temp/(ew*e0))*sinh(elec*Vgc[i]/(2.0*kb*Temp));
EgcOut<<Egc[i]<<" ";
}
FILE * f=fopen ("x.dat", "w");
gsl_vector_fprintf(f, x, "%.5g");
fclose(f);
//Freeing up spline objects
gsl_spline_free (spline);

```

```
gsl_interp_accel_free (acc);
cout<<"# of timesteps="<<j<<" Total time="<<TIME<<endl;
time(&end);
dif = difftime(end, start);
cout<<endl;
int dif=int (dif);
int hr=dif/3600;
int min=(dif%3600)/60;
int sec=((dif%3600)%60);
cout<<"Time to run program is "<<hr<<"hr "<<min<<"min "<<sec<<"s"<<endl;
return 0;

}
```